PRODUCTION AND CHARACTERIZATION OF POROUS CERAMICS FOR HIGH TEMPERATURE APPLICATIONS

A Thesis Submitted to
the Graduate School of Engineering and Sciences of
İzmir Institute of Technology
in Partial Fulfillment of the Requirements for the Degree of

DOCTOR OF PHILOSOPHY

in Materials Science and Engineering

by
Tuğçe SEMERCİ

July 2022
İZMİR

ACKNOWLEDGMENTS

A thesis is further enhanced by external evaluation by experienced researchers in the relevant field. Thus, I would like to thank the members of the thesis committee Prof. Dr. Mustafa M. Demir, Prof. Dr. Ahmet E. Eroğlu, Prof. Dr. Ali Aydın Göktaş, and Assoc. Prof. Dr. Nesrin Horzum Polat. Their comments and suggestions have been invaluable.

I am grateful for the financial support provided by the Air Force Office of Scientific Research (AFOSR) during my studies.

Members of our research group "Inorganic Solid Materials Group" always made their team spirit, fellowship, and support available during this academic journey, and for that, I offer my thanks.

I also wish to thank the teams of the Center for Materials Research (CMR) and the Biotechnology and Bioengineering Application and Research Center (BIOMER) at the Izmir Institute of Technology for their help during my analyses.

Many people have contributed their expertise during my studies. Hence, I would like to thank Prof. Dr. Murilo Daniel de Mello Innocentini for his input on gas permeability tests, Prof. Dr. Gian Domenico Soraru and his Ph.D. student Apoorv Kulkarni for their input on additive manufacturing, Assoc. Prof. Dr. Derya Dışpınar and his Ms.C. student Kerem Can Dizdar for their input on molten metal filtration tests, Prof. Dr. Alberto Ortona and his Ph.D. student Marco Pelanconi for their input on heat exchange tests, and Prof. Dr. Ahmet Yemenicioğlu and his Ph.D. student Pelin Barış Kavur for their help on mechanical tests.

I am obliged to my colleagues at the Izmir Institute of Technology, especially Öykü İçin, Ezgi Oğur, and Nazlıcan Uza for their kind support and friendship.

Lastly but most importantly, I am deeply grateful to my parents Selma and Hasan Semerci, for their moral support and endless love for being by my side under all circumstances. Also, I offer my special thanks to Dr. Uras Tos for always being there for me and for supporting me in my toughest battles. I owe them everything for what I am today.

ABSTRACT

PRODUCTION AND CHARACTERIZATION OF POROUS CERAMICS FOR HIGH TEMPERATURE APPLICATIONS

This thesis focuses on the production and characterization of different porous polymer derived ceramic (PDC) components (foams, additively manufactured (AM) honeycombs, and aerogels) and demonstrates their potential for high temperature applications, including gas permeability (up to ~700 ^{o}C), molten metal filtration, and heat exchanger.

The foams were produced via the replica technique and different pore sizes, ranging from 300 μm to 2 mm, silicon oxycarbide (SiOC) ceramic foams were able to be formed. The average total porosity of the foams was 96 vol% with a specific surface area (SSA) of ~80 m^2/g. AM-made honeycomb-like cellular structures with different cell sizes (578 μm, 1040 μm) were obtained via fused filament fabrication. Finally, SiOC aerogels were synthesized using siloxane resin, then dried at ambient pressure and room temperature. The produced SiOC aerogels showed a total porosity of around 80 vol% and an SSA reaching 250 m^2/g.

Regarding the high temperature applications of porous PDC components, initially, the gas permeability of SiOC foams was tested, and the results showed stability up to 700 °C in the air without any loss of functionality, offering reusability even in aggressive environments. In the subsequent studies, filtration of molten aluminum alloy was tested using various porous components. PDC foams demonstrated better performance in comparison to the AM-made cellular structures and commercial SiC foams. Finally, heat exchange analysis was performed to evaluate the heat transfer of SiOC foams, and an increase in pressure drop was found to be directly proportional to the rate of increase in air velocity.

ÖZET

YÜKSEK SICAKLIK UYGULAMALARI İÇİN GÖZENEKLİ SERAMİKLERİN ÜRETİMİ VE KARAKTERİZASYONU

Bu çalışma içerisinde, farklı gözenek yapısına sahip polimer türevli seramikler (polymer derived ceramic, PDC) üretilmiştir. Öncelikle polimerik yapıda köpükler, ardından eklemeli imalat (additive manufacturing, AM) ile üretilmiş petek benzeri yapılar ve son olarak da aerojellerin imalatı yapılmıştır. Ortaya çıkan gözenekli seramikler gaz geçirgenlik (~700 ^{o}C'ye kadar), eriyik metal filtrasyonu ve ısı eşanjörü gibi yüksek sıcaklık uygulamaları için testlere tabi tutulmuşlardır.

Seramik köpükler replika tekniği ile üretilmiş ve 300 µm ile 2 mm arasında değişen farklı gözenek boyutlarına, hacimce ortalama %96 toplam gözenekliliğe ve yaklaşık 80 m^2/g spesifik yüzey alanına (specific surface area, SSA) sahip silikon oksikarbür (SiOC) seramikleri elde edilmiştir. Eklemeli imalat ile petek benzeri hücresel yapılar farklı hücre boyutlarıyla (578 µm, 1040 µm) üretilmiştir. Son olarak, SiOC aerojelleri siloksan reçinesi kullanılarak jel haline getirilmiş ardından ortam basıncı ve oda sıcaklığında kurutularak polimerik aerojellerin sentezi yapılmıştır. Yüksek sıcaklık pirolizi sonucunda elde edilen SiOC aerojelleri, hacimce yaklaşık %80 toplam gözeneklilik ve 250 m^2/g SSA değeri vermiştir.

Yüksek sıcaklık uygulamalarıyla ilgili, ilk olarak SiOC köpüklerinin gaz geçirgenlik testleri yapılmış ve sonuçlara göre test edilen köpükler herhangi bir işlevsellik kaybı olmadan havada 700 °C'ye kadar stabilite göstererek, agresif ortamlarda bile yeniden kullanılabilirlik imkânı sunabilmişlerdir. Takip eden çalışmalarda, eriyik alüminyum alaşım filtrasyonu, çeşitli gözenekli bileşenler kullanılarak test edilmiş ve PDC köpükleri hem AM ile üretilen hücresel gözenekli yapılara hem de ticari SiC köpüklerine kıyasla daha iyi performans göstermiştir. Son olarak, SiOC köpüklerin ısı transferini değerlendirmek için ısı eşanjörü testleri yapılmış ve sonuçlar basınç düşüşündeki artışın, hava hızındaki artış oranıyla doğru orantılı olduğunu göstermiştir.

Dedicated to my lovely mom and dad…

TABLE OF CONTENTS

LIST OF FIGURES

Figure **Page**

Figure **Page**

Figure **Page**

Figure **Page**

Figure **Page**

Figure **Page**

LIST OF TABLES

Table **Page**

LIST OF ABBREVIATIONS

ADA	Azodicarbonamide
BTEE	Bis(triethoxysilyl)ethane
BTEM	Bis(triethoxysilyl)methane
DBTDL	Dibutyltin dilaurate
IUPAC	International Union of Pure and Applied Chemistry
LDH	Layered doubled hydroxide
MTES	Methyltriethoxysilane
PDC	Polymer derived ceramic
PDMS	Polydimethylsiloxane
PE	Polyethylene
PHMS	Polymethylhydrosiloxane
PMF	Poly(melamine-formaldehyde)
PMMA	Poly(methyl methacrylate)
PMPS	Phenyl methyl poly (silsesquioxane)
PMS	Polymethylsilsesquioxane
PP	Preceramic polymer
PS	Polystyrene
PU	Polyurethane
SAXS	Small-angle X-ray scattering
SSA	Specific surface area
TBA	Tert-butyl alcohol
TEOS	Tetraethoxysilane
VTES	Triethoxyvinylsilane

CHAPTER 1

INTRODUCTION AND MOTIVATION

Ceramics have great potential to be used in high temperature technological processes that include furnace elements, thermal insulators, filtration (gas & liquid) devices, porous burners, heat exchangers, etc., due to their good thermal and chemical stability. As can be seen in Figure 1.1, the increase in the number of publications in the last two decades (note that the data is incomplete for 2022, as the year had not yet been concluded when the data was obtained) shows a genuine interest in the topic.

Production of porous ceramics from preceramic polymers, i.e., polymer derived ceramics (PDCs), provides benefits compared to the conventional methods (e.g., traditional high temperature powder consolidation and sintering techniques) including a low processing temperature and simple production steps. PDCs are amorphous materials composed of nanodomains such as carbon, silicon carbide (SiC), or silicon nitride (Si_3N_4), depending on the processing conditions and preceramic polymer type.[1] When polysiloxanes, i.e., the most economical type of preceramic polymers, are pyrolyzed in the temperature range of ≥800-1400°C, an amorphous silicon oxycarbide (SiOC) with the general formula SiO_xC_{4-x} ($0<x<4$) is obtained. SiOC is an anionic modification of silica-glass, in which some of the divalent oxygen atoms are replaced by tetravalent carbon atoms. This modification provides enhanced properties compared to silica glass.[2] For instance, compared to vitreous silica, PDC provides enhanced high temperature creep and oxidation resistance.[1,3–6] The viscosity of amorphous PDCs is not only 2-3 times higher than that of vitreous silica but also the highest of all glasses.[7,8] These properties of PDCs have made them promising materials for high temperature applications.

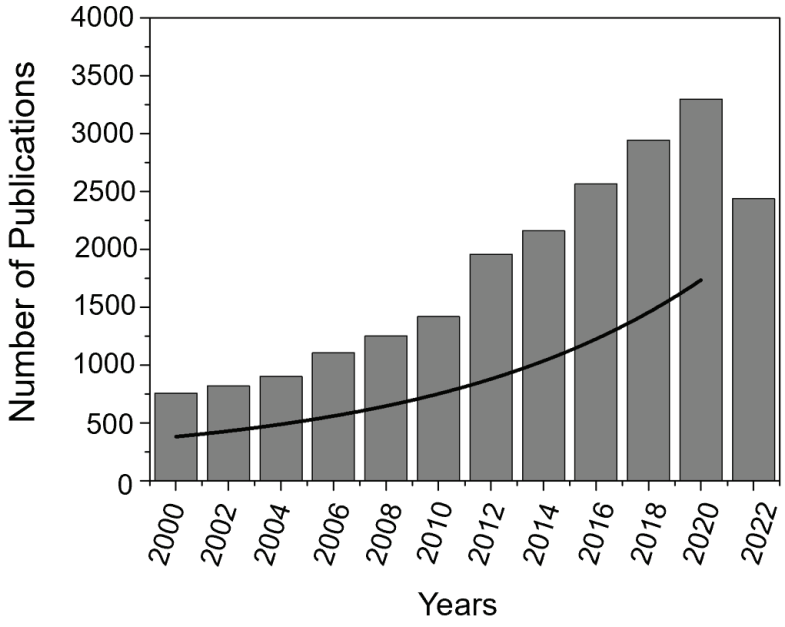

Figure 1.1. Number of publications resulting from a *google scholar* search with the keywords “high temperature applications”, “hot gas filters”, “molten metal filters”, “porous burners”, “high temperature thermal insulators”, “heat exchangers”, and “ceramics”. Data were extracted and merged from 1 January 2000 up to 1 July 2022, and the line represents an exponential growth function fit. (Source: Google Scholar, 2022)

Despite numerous studies focused on the production of porous PDCs, there are only a few studies on the applications of these PDC structures, particularly for high temperatures. Accordingly, this thesis focuses on the production and characterization of porous PDC components such as foams, honeycomb-like cellular structures, and aerogels, and shows their potential for high temperature applications, such as gas permeability (up to ~700 ^{o}C), molten metal filtration, and heat exchanger.

CHAPTER 2

LITERATURE REVIEW

Published in part in: Vakifahmetoglu, C., Semerci, T., Gurlo, A., & Soraru, G. D. "Polymer derived ceramic aerogels". Current Opinion in Solid State and Materials Science, 25(4), 100936, (2021).

2.1. Polymer Derived Ceramics (PDCs)

Preceramic polymers (PP) are organosilicon-based polymers that generally contain a Si chain backbone, as shown in Figure 2.1, and have been used to obtain Si-based polymer-derived ceramics (PDCs) since the early 1960s.[9] PDC route enables the production of Si-based binary (e.g., SiC),[10–12] ternary (e.g., SiOC,[10,13,14] and SiCN[15–17]), quaternary (e.g., SiBCN,[15,18,19] SiCNO,[20,21] and SiBCO[22,23]), and pentanary (e.g., HfSiCNO (Hf-O-doped SiCN),[24] and SiHfBCN[5]) ceramics.

PDCs having cellular and 3D complex structures have been produced using PPs.[25–27] Ceramic production using PP has many advantages over the conventional method (sintering of ceramic powder).[28] For instance, PPs require low processing temperatures compared to ceramic powders.[29,30] Additionally, PDCs do not need sintering additives. It is possible to shape preceramic polymer with low-cost techniques including compression/injection molding, spinning, and extrusion.[31–34]

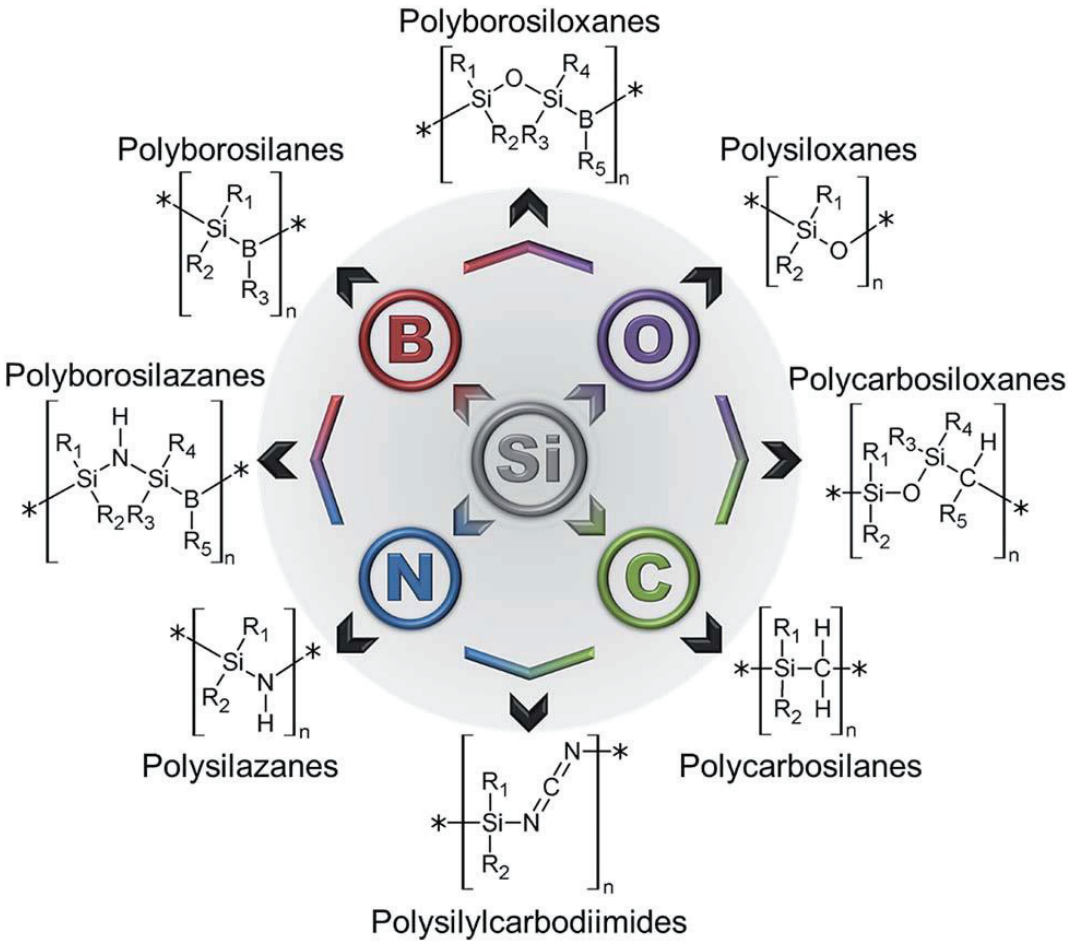

Figure 2.1. Main classes of silicon-based preceramic polymers.

(Source: Barroso, G et al., 2018)[35]

The microstructural properties of the final PDCs can be altered by varying the amount of carbon in the structure. Previously, it was shown that the carbon in the structure adversely affected the PDCs' properties, but recently it has been discovered that carbon-rich PDCs show more enhanced properties than that of low-carbon PDCs under certain conditions.[36–39] Free carbon contributes towards multifunctional properties of carbon-rich PDCs that include piezoresistivity,[40] corrosion resistance,[41] electrical conductivity,[42,43] and creep resistance.[3,44]

Production of PDCs consists of the following steps (see Figure 2.2): (i) synthesis of precursors (or using commercial preceramic polymers), (ii) shaping and crosslinking, and (iii) polymer to ceramic transformation (i.e., ceramization).

It is possible to adjust the chemical and physical properties of the final PDC by synthesizing precursors. There are key points that affect this synthesizing process.[8,45] One important point is that the polymers should have enough high molecular weight and a cage-like structure to prevent volatilization. Another point is to adjust the solubility and viscosity properties of precursors. On the other hand, preceramic polymers, as presented in Figure 2.1, are widely used to produce high-efficiency PDC.

Since production parameters such as solubility and viscosity of preceramic polymers can be adjusted, PDCs can be easily obtained with a variety of shaping methods including but not limited to coating,[46,47] spinning,[32,48] and 3D printing.[14,49]

Crosslinking is the most important step in PDC production because it contributes toward maintaining the obtained shape and increasing the ceramic yield by producing non-fusible thermoset structures and avoiding the loss of organosilicon species.[50] This process can be carried out in an oxidative or inert atmosphere (e.g., polysiloxane or polysilazane) by various kinds of exposures that include thermal, and ultraviolet (UV).[51,52] The thermal crosslinking process takes place through reactions formed by the reactive groups of the preceramic polymers.[8] In essence, some of these reactions can be listed as follows: hydrosilylation (Si-H/CH=CH_2), dehydrocoupling (Si-H/Si-H and Si-H/N-H, etc.), and vinyl polymerization (CH=CH_2).[53–55] Furthermore, the catalyst used during thermal crosslinking can also affect the curing process. The UV crosslinking process is achieved by using photosensitive functional groups to obtain the cured polymer even at room temperature.[56,57]

PDCs are obtained by pyrolysis (organic-inorganic transition) of crosslinked preceramic polymers in an inert atmosphere between 600-1400 °C.[8] During this transition, the release of organic functional groups including CH_4 and C_6H_6 takes place and mass loss occurs which is generally between 10-30%.[58] This mass loss is associated with the efficiency of the preceramic polymers and ceramic yield.[47] At low pyrolysis temperatures (above 400 ^oC), the release of gaseous decomposition products causes transient microporosity with high specific surface area (SSA). This porosity disappears at high temperature pyrolysis (800-1000 ^oC) because of the densification mechanism.[47,58] On the other hand, crystalline ceramic is obtained when the thermoset structure is pyrolyzed at high temperatures (above ~1200 ^oC) by starting to grow nano-sized crystals.[59]

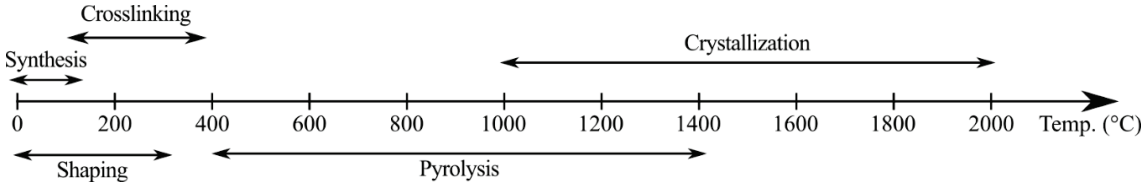

Figure 2.2. Production steps of PDCs at various temperature ranges.

2.1.1. Silicon Oxycarbide (SiOC)

Silicon oxycarbide is an amorphous material that consists of silicon atoms coordinated with oxygen and carbon atoms.[1,37,60] The structure of SiOC contains a random network of Si-C and Si-O bonds with tetrahedral units of SiO_xC_{4-x} ($0<x<4$). This network shows a full range of mixed bonded with possible Si sites (SiC_4, SiC_3O, SiC_2O_2, and SiO_4), that mostly depends on initial polymer composition and pyrolysis temperature.[41]

Thermoset structures, i.e., cured preceramic polymers, turn into an amorphous material when the pyrolysis temperature is increased above ~500 °C. During this transformation, hydrocarbon gases, i.e., CH_4 and C_6H_6, and the hydrogen gas leave the system and free carbon accumulates. Because of this carbon formation, SiOC is also called black glass.

The presence of free carbon in PDCs, especially in SiOC, has been often reported in the literature.[15,39,61,62] By heat treating at low temperatures free carbon is precipitated as carbon cluster [Basic Structural Units (BSU)], whereas high temperatures yield graphite carbon regions.[63] The influence of saturated (methyl, propyl, etc.) and unsaturated (phenyl, allyl, etc.) hydrocarbons on free carbon are different. Saturated groups have a less free carbon effect on PDC, while unsaturated ones have a greater effect.[1] In one particular study, it was shown that the amount of free carbon in the obtained SiOC increases with the increase of the phenyl groups in the preceramic precursor.[63] Changes in the thermal treatment processes during PDC production also influence the free carbon.[64,65]

Ceramer (CERAmic + polyMER) is a particular type of PDC that occurs when pyrolysis is carried out at 600 to 800 ^oC.[66] SiOC glass is obtained by the cleavage and

volatilization of organic groups including hydrocarbon and hydrogen gases at T>1000 ºC.[8,67] When heat treated at a higher temperature (T>1400 ºC), SiC formation begins in certain areas.[68] The size of the formed SiC nuclei also increases with phase separation. Figure 2.3 shows HRTEM images of SiOC glass obtained from sol-gel process when the material is pyrolyzed between 1000 and 1400 °C in Ar.[60] While the sample treated at 1000 °C shows an amorphous network as well as a low phase contrast, a few lamellar structures (shown in the inset) are observed in turbostratic carbon, as depicted in Figure 2.3 (a). Figure 2.3 (b) shows that, when heat treated at a higher temperature (T>1200 ºC), SiOC is completely amorphous with only a weak phase contrast. Few lamellar features are observed which refer to BSU. Darker regions and lattice fringes that belong to SiC precipitates are shown in Figure 2.3 (c) while Figure 2.3 (d) shows numerous nanosized SiC precipitates.

One of the proposed models on the SiOC structure is shown in Figure 2.3 (e).[69] This model shows nanodomains of SiOC ceramic produced by pyrolysis under Ar at 1200 °C. The presence of amorphous silica regions and graphene cage-like networks are observed and the width of silica nanodomains is measured using SAXS as 1-5 nm. The structure shown in this model explains the properties of SiOC, notably an outstanding creep resistance and unique viscoelastic behavior.

Preceramic polymers have been successfully used to produce both open and closed porosity ceramic components since using them provides advantages over the conventional method. For this reason, recently porous components have been widely produced and used in different applications. These porous ceramics, especially porous PDC, production methods, applications including filtration (gases & liquids), as well as thermal and sound insulation will be described in the following sections.

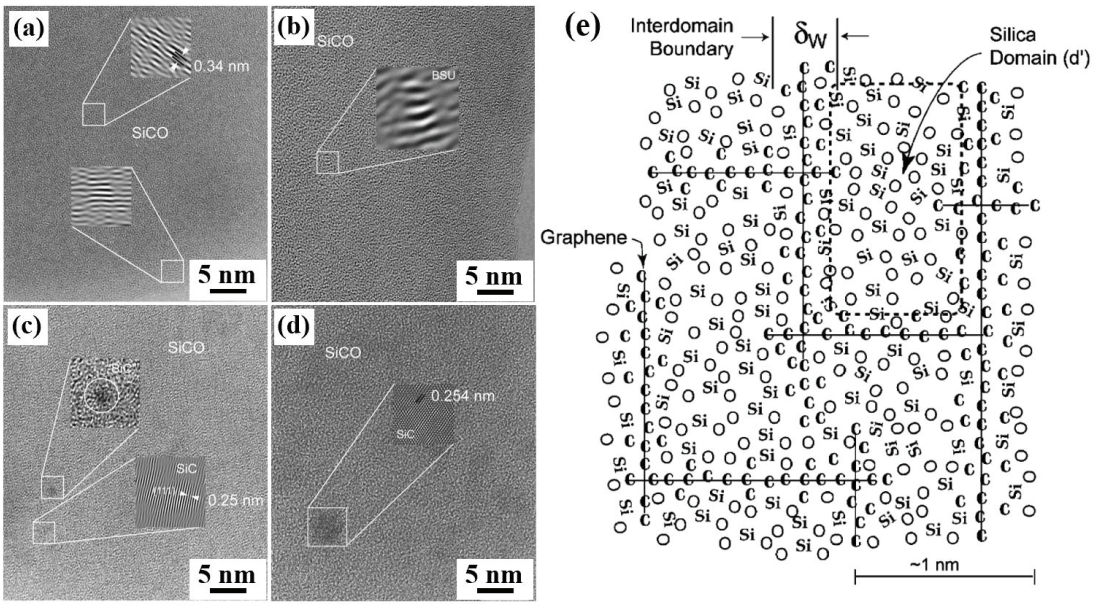

Figure 2.3. HRTEM images of SiOC glass annealed at (a) 1000 °C, (b&c) 1200 °C, (d) 1400 °C in Ar, and (e) a proposed model for the nanodomains in low-medium carbon containing SiOC. (Sources: Kleebe, H-J et al., 2001; Saha, A et al., 2006)[60,69]

2.2. Porous Ceramics

Porous ceramics have a unique combination of properties including high mechanical strength in addition to thermal and chemical stability at low relative density. In the last 30 years, considerable effort has been devoted to the production of both open and closed porosity ceramics to benefit from these desirable properties.[70] Hence, porous materials are of great interest for a wide range of technological processes that include insulation (thermal & sound), catalyst support, and absorption.[71,72] The applications of porous ceramics can be diversified according to their porosity properties. For instance, high surface area improves the functionality of the material while macroporosity improves heat and mass transfer.[73]

Cellular ceramics are highly porous (total porosity >60 vol%) materials with polyhedral cells and can be described mostly as a typical honeycomb or foam depending on their morphology. Honeycombs consist of regularly uniaxial channels, while foams

have reticulated structures with a 3D interconnected porosity. Figure 2.4 (a&b) shows the AM-made ceramic honeycomb with hexagonal cells obtained by direct foam writing of particle-stabilized foams.[74] The term porosity in foams is measured in pores per inch (ppi) and refers to the number of pores in one linear inch. Alumina foams having a porosity value of 10 and 27 ppi prepared by the replica method are shown in Figure 2.4 (c&d).[75]

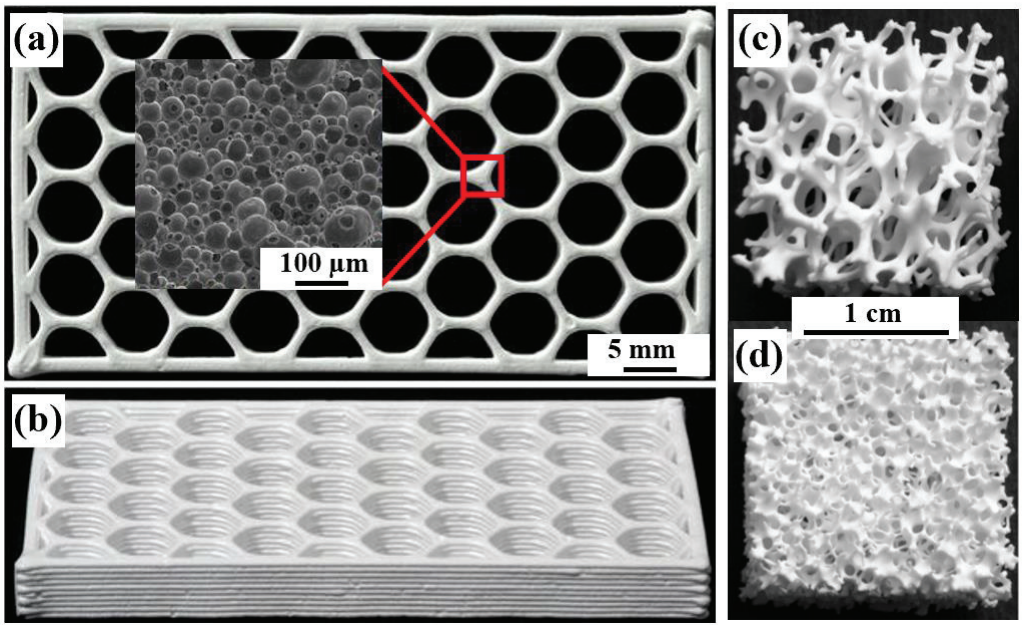

Figure 2.4. (a&b) Representative AM-made hexagonal ceramic honeycomb. The inset shows the SEM image of the closed porosity microstructure of the node; and photographic images of alumina foams with porosity of (c) 10 ppi, and (d) 27 ppi. (Sources: Muth, J et al., 2017; Hadi, A et al., 2015)[74,75]

There are different possibilities for categorizing porous components. One of the most used is based on pore size according to the IUPAC definition.[76] In this terminology, the pores are defined based on macroporous polymeric materials with pore sizes between 50 nm and 1 µm. According to this definition, pores are classified as microporous when the pore size is < 2 nm, mesoporous when the pore size is in the 2-50 nm range, and macroporous when the pore size is > 50 nm. A variable definition based on "cell" has been adapted from the plastics industry to distinguish between micrometer

to millimeter-sized pores. Therefore, pores between 1 and 100 µm are called microcellular, while pores larger than 100 µm are called macrocellular. It is important to note here that cell and pore sizes refer to the different structures of ceramics. A cell has a small opening on the cell face/wall, which is generally called a cell window (pore). Figure 2.5 shows the difference between the cell and cell window sizes. Apart from the pore size, pore structure/shape is also used for classification, where different material classes are represented by open (permeable, interconnected), blind (dead-end), closed (isolated), and mixed porosities. Depending on the pore structure, e.g., open/closed cell, cellular ceramics have various application areas including filtration (gases & liquids), lightweight sandwich structures, and heat exchange.[77,78]

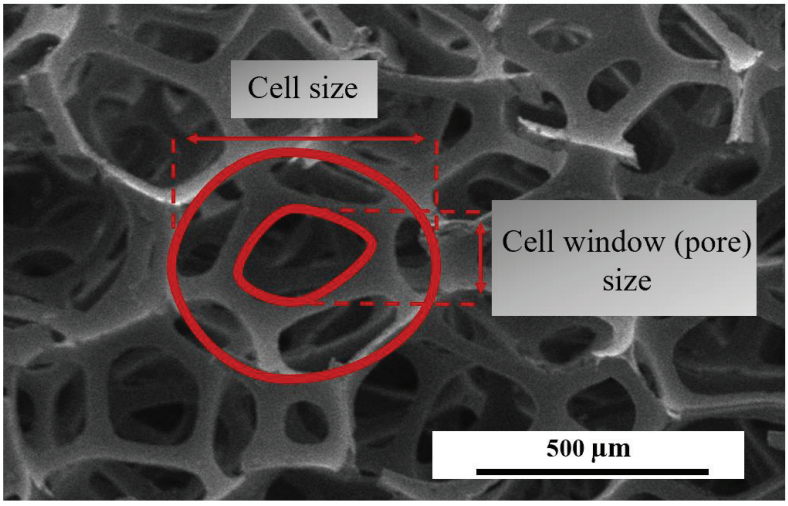

Figure 2.5. SEM image of open cell PU foam with 80 ppi showing cell and cell window sizes.

2.2.1. Porous PDCs

Production of porous ceramics using PP has advantages compared to the conventional method including a low processing temperature, simple production steps, and easy formability with low-cost techniques. Different fabrication methods have been developed to produce porous PDCs. Since porous PDC production methods, properties

and applications are adequately explained in comprehensive reviews,[66,79] only the most common production methods are mentioned in this thesis.

I) Sacrificial Templating

Sacrificial templating method comprises polymer precursors and pore formers (sacrificial), the latter of which creates porosity after they are burnt out/decomposed.[80] This method is categorized as a negative replica since pore formers leave pores behind, contrary to the replica technique, which acts as a positive replication method. During the burn-out/decomposition process, gases might be released, resulting in a crack formation that affects the features of the obtained ceramic.[81] However, dense struts are generally obtained with this method, yielding improved ceramic properties. Additionally, sacrificial templating provides an opportunity to obtain a porous PDC in the desired pore size and porosity via selecting the appropriate sacrificial template (according to the intended pore structure/size). In this regard, Table 2.1 lists properties of the porous PDCs obtained by sacrificial templating.

SiOC foams were obtained by a mixture of precursor and poly(methyl methacrylate) (PMMA) microbeads (with sizes of 10, 25, 50, 100, and 185 μm), as shown in Figure 2.6.[82,83] Gas permeability tests were carried out for the microcellular SiOC foam (10-150 μm cell size and 83-89 vol% total porosity) and $k_1 \sim 0.29 \times 10^{-12}$ - 92.00×10^{-12} m^2 & $k_2 \sim 0.02 \times 10^{-5}$ - 17.11×10^{-5} m were found. It was shown that gas permeability increases as the cell size increases.[82] SiOC foams with total porosity >70 vol% were also prepared with iron silicide micro powders as fillers to achieve a soft-ferromagnetic property. The compressive strength of the foam decreased with the increase in the amount of iron silicate.[83]

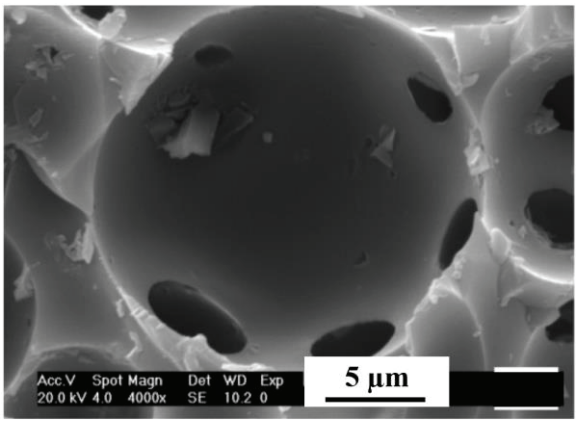

Figure 2.6. SEM image of SiOC foam obtained with PMMA microbeads having the size of 25 µm. (Source: Biasetto, L et al., 2007)[82]

Si(O)CN foams with cell size up to 15 µm, total porosity of ~61 vol%, and compressive strength of ~11.6 MPa were produced using PMMA microbeads.[84] Apart from the PMMA beads, polystyrene (PS) [as depicted in Figure 2.7 (a)] and polyethylene (PE) are also used as sacrificial templates to obtain a porous structure.[85,86] SEM image of closed porosity SiCN foam obtained with PS beads is shown in Figure 2.7 (b). SiOC foams having a total porosity of up to 70 vol% and 90 vol% were obtained by using epoxy powder and corn starch.[87,88] In another study, polyurethane (PU) foam was synthesized using a blowing agent and then SiOC and SiOC+SiC foams were produced using PU foam as a sacrificial template.[30,89,90]

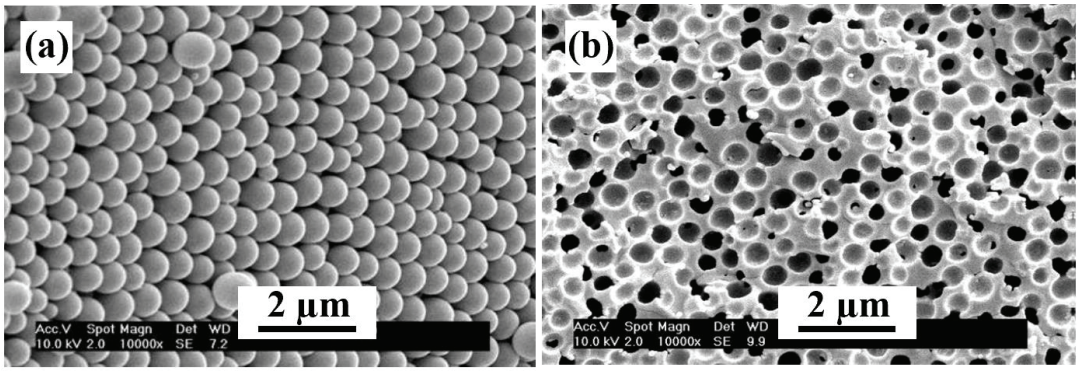

Figure 2.7. SEM images of (a) PS beads, and (b) SiCN foam having closed porosity. (Source: Yan, J et al., 2007)[85]

Table 2.1. Properties of porous PDCs produced by sacrificial templating.

Formed PDCs / Pore-forming agent	Pore properties	Other properties	Possible applications	Ref.
SiOC foam / PMMA microbead	ϕ_T ~ 70-89% Ø = 10-150 μm & 10-50 μm	σ_c ~ 1.3-9 MPa k_1 ~ 0.29 x 10^{-12}-92.00 x 10^{-12} m^2 k_2 ~ 0.02 x 10^{-5}-17.11 x 10^{-5} m B_s = 9.5-17 emu/g	Aerosol filtration, ferromagnet in devices	82,83
SiOC foam / PMMA microbead & PE	ϕ_T ~ 40-94% Ø ~ 9-100 μm	σ_c ~ 12-16 MPa	N.A.	86
SiOC foam / Epoxy powder	ϕ_T ~ 35-69% ρ_b ~ 0.62-1.31 g/cm^3	σ_c ~ 15-38 MPa E = 10 GPa (@ 56% ϕ_T)	N.A.	87
SiOC foam / Corn starch	ϕ_T = 78-90%	σ_c ~ 2-9 MPa	N.A.	88
SiOC & SiOC+SiC foams / PU	ϕ_T ~ 80-90% ρ_b ~ 0.10-0.56 g/cm^3 Ø ~ 200-1100 μm	σ_c ~0.7-14 MPa E ~ 15-450 MPa α_l = 1.1 x 10^{-6} K^{-1}	N.A.	30,89,90
SiOC / LDH	SSA ~ 501-1311 m^2/g	N.A.	Catalysis, gas adsorption/separation under harsh conditions	91,92
Si(O)CN foam / PMMA microbead	ρ_b ~ 0.520-0.885 g/cm^3 ϕ_T ~ 61-77%	σ_c ~ 5.6-11.6 MPa	High temperature application	84
SiCN foam / PS sphere	SSA ~ 71-184.5 m^2/g Ø ~ 500-1000 μm	N.A.	N.A.	85

N.A. = not available, Ø = pore diameter, ϕ_T = total porosity, SSA = specific surface area, k_1 = Darcian permeability, k_2 = non-Darcian permeability, ρ_b = bulk/apparent density, σ_c = compressive strength, E = Young's modulus, B_s = magnetic induction, α_l = thermal expansion coefficient.

II) Foaming

In direct foaming, pores are formed by introducing gas bubbles into the liquid form through (i) self-foaming, (ii) blowing agents, and (ii) gas blowing. Gas bubbles first nucleate and then with the increase in bubble size, pore formation begins. Table 2.2 gives the properties of the porous PDCs obtained by direct foaming. The setting of gas bubbles inside the liquid form is the most crucial subject in this method since the liquid form is thermodynamically unstable and gas bubbles tend to coarsen. This causes gas

bubbles to grow or shrink/disappear, which unintentionally affects the pore size/total porosity of porous ceramics.[71]

Si/SiC filled SiOC foams were obtained with the foaming via i.e., water and ethanol, during the condensation reaction of the phenyl methyl poly (silsesquioxane) (PMPS) precursor. It was shown that pore distribution varied according to crosslinking temperature and time.[93]

The melt viscosity of the preceramic polymer is the most crucial parameter for controlling the foaming process. Foaming is related to the viscosity of the liquid form at the foaming temperature, and the growth of gas bubbles is resisted by viscosity. The lower viscosity of the liquid form provides higher gas bubbles growth rates than those having a higher viscosity. Therefore, larger pore sizes are obtained in liquid form with lower viscosity.[94] It was stated that the viscosity of the PMS/isopropanol solution showed a minor effect on the density and total porosity of the SiOC foam, but a major effect on the pore size distribution.[94] Due to the change in the viscosity behavior of the preceramic polymer, SiOC foams with gradient structure started to be obtained at 220 °C while a homogeneous structure was obtained at 270 °C.[93] Porous SiOC and SiOC-SiC were produced from another commercially available silicone resin by a self-blowing process.[95–97]

Two chemical reactions took place during the preparation of SiOC, namely: (i) hydrosilylation (for crosslinking) and (ii) dehydrogenation (for blowing). Ethanol as a chemical blowing agent reacted with silicone oil [polymethylhydrosiloxane (PHMS)] and created hydrogen for the foaming process.[98] SiCN macro-cellular foams (cell size ~700 μm) were obtained by using commercially available poly(methylvinyl)silazane and a physical blowing agent azodicarbonamide (ADA) (1wt%) in a one-step process, as depicted in Figure 2.8.[84]

Ni-containing porous SiOC foams were prepared by using the same blowing agent, i.e., ADA, and as a result, 71-78 vol% of total porosities were obtained. Gas permeability tests were carried out and $k_1 = 4.10 \times 10^{-10}$ m^2 and $k_2 = 3.17 \times 10^{-6}$ m were found for foams having 74.2 vol% total porosity (open porosity of 69.2 vol%).[99] Gaseous, liquid, or supercritical CO_2 were shown to be viable as a pore-forming agent in porous structures that were obtained by gas blowing.[33,100,101] Mixture of polycarbosilane and polysiloxane were saturated with gaseous CO_2 and microcellular SiOC foams having mostly closed cells (cell size < 10 μm) were obtained.[101]

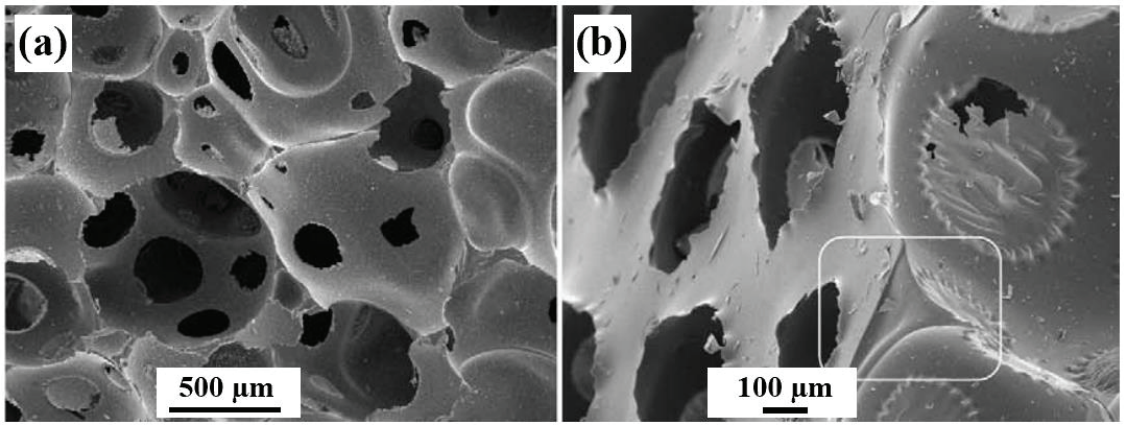

Figure 2.8. SEM images of (a) obtained SiCN foam using 1 wt% ADA, and (b) dense strut showing with a white rectangle. (Source: Vakifahmetoglu, C et al., 2009)[84]

Table 2.2. Properties of porous PDCs produced by direct foaming.

Formed PDCs / Pore-forming agent	Pore properties	Other properties	Possible applications	Ref.
i) Self-foaming				
SiOC foam / Silicone resin	N.A.	σ_c ~ 1-9 MPa	N.A.	93
SiOC & SiOC-SiC / Silicone resin	ϕ_T ~ 52-88%	σ_c ~ 1-27 MPa	N.A.	95–97
ii) Physical/chemical blowing agents				
SiOC foam / Ethanol	ρ_b ~ 0.20-1.20 g/cm^3 Ø ~ 150-500 µm	N.A.	N.A.	98
Ni-containing SiOC / ADA	ϕ_T ~ 71-78%	k_1 ~ 4.10 x 10^{-10} m^2 k_2 ~ 3.17 x 10^{-6} m (@ ~74% ϕ_T)	Catalysis	99
SiC foam / ADA	ϕ_T ~ 59-85% Ø = 416-1455 µm	N.A.	N.A.	102
SiCN foam / ADA	ρ_b ~ 0.687-0.830 g/cm^3 ϕ_T ~ 64-71%	σ_c ~ 1.08-3.31 MPa	High temperature application	84
iii) Gas Blowing				
SiOC foam / CO_2	ϕ_T ~ 45% Ø < 10 µm	N.A.	N.A.	101
SiOC / CO_2	ϕ_T ~ 64-89% Ø ~ 10-400 µm	N.A.	High temperature application	33,100

N.A. = not available, Ø = pore diameter, ϕ_T = total porosity, k_1 = Darcian permeability, k_2 = non-Darcian permeability, ρ_b = bulk/apparent density, σ_c = compressive strength.

III) Freeze Casting

Freeze casting is a method in which a frozen liquid acts as a sacrificial template for the pores.[103,104] Table 2.3 gives the properties of the porous PDCs obtained by freeze casting. Commercially available siloxane resin (PMPS) was dissolved in heated solvents [cyclohexane, camphene, and tert-butyl alcohol (TBA)] to allow for the formation of a homogenous form. After the dissolved siloxane resin was cured by a crosslinking agent [Dibutyltin dilaurate (DBTDL)], the solution was frozen, causing a phase separation between the dissolved siloxane resin and the solvent. The solidified solvent was sublimated to obtain the porous structure by freeze-drying. The use of cyclohexane and camphene caused dendrite pores while the use of TBA caused cellular pores,[103] as shown in Figure 2.9.

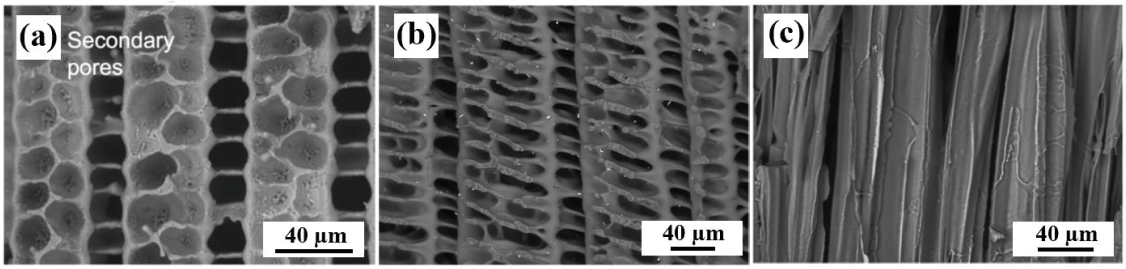

Figure 2.9. SEM images showing different pore structures obtained from (a) cyclohexane, (b) camphene, and (c) TBA, with 20 wt% siloxane resin. (Source: Naviroj, M et al., 2015)[103]

Table 2.3. Properties of porous PDCs produced by freeze casting.

Formed PDCs / Pore-forming agent	Pore properties	Other properties	Possible applications	Ref.
SiOC / Cyclohexane & camphene & TBA	ϕ_T ~ 61-95% Ø ~ 10-60 µm	N.A.	N.A.	103
SiC / Camphene	Ø = 2.7-23 µm	N.A.	N.A.	104

N.A. = not available, Ø = pore diameter, ϕ_T = total porosity.

IV) Thermal Processing

Ceramer (CERAmic + polyMER) is a particular type of PDC material that is obtained from the decomposition of precursors during mineralization (400-800 ºC).[66] Micro and meso pores, i.e., transient porosity, are generated through the gas released due to the decomposition of CH_3 and C_6H_5 groups in PP. These materials are neither proper polymers nor can be defined as ceramics but have a much higher SSA. Hence, they are suitable for applications that include adsorption and filtration.[105–107] Table 2.4. summarizes properties of the porous PDCs obtained by preceramic polymer decomposition. SiOC foams were obtained with micro/mesopores in the struts/cell walls with an SSA up to 436 m^2/g when pyrolyzed at 600 ºC. When SiOC foams were pyrolyzed at 1200 ºC, and an SSA of 13 m^2/g was obtained. Activated carbon was added to the foams, and then an SSA up to 130 m^2/g was obtained.[105] In other studies, SiOC ceramers were produced as a pellet and bead with an SSA up to ~430 and 370 m^2/g.[106,107]

Table 2.4. Properties of porous PDCs produced by preceramic polymer decomposition.

Formed PDCs / Pore-forming agent	Pore properties	Other properties	Possible applications	Ref.
SiOC foam / N.A.	SSA ~ 13-436 m^2/g Ø ~ 2.92-4.51 nm	N.A.	Adsorption	[105]
SiOC / N.A.	SSA = 432 m^2/g	N.A.	Adsorption	[106]
SiOC nanobead / N.A.	SSA = 370.9 m^2/g	q_m = 0.6 mg/g	Adsorption	[107]

N.A. = not available, Ø = pore diameter, SSA = specific surface area, q_m = adsorption capacity.

2.2.1.1. PDC Cellular Structures

In this thesis, PDC foams and cellular structures were produced using replica and additive manufacturing among the porous PDC production methods mentioned above. These methods will be explained in the following subsections.

2.2.1.1.1. Replica Technique

The replica is a preferred method among the porous PDC production techniques to obtain reticulated ceramic foams. In this technique, a porous ceramic with a similar structure to the original template is obtained by impregnating/coating with a hard/soft template (wood, polymeric foam, silica, etc.)[108] in polymeric suspension. This technique was patented in 1963 by Schwartzwalder and Somers who worked using a PU sponge as a template along with conventional ceramic slurries.[109] Table 2.5 shows properties of the porous PDCs obtained by the replica technique.

Reticulated SiOC foams (having mostly open or partially closed cells) with thermal conductivity of 0.03-0.16 $W \cdot m^{-1} \cdot K^{-1}$ at R.T. and having total porosity of 79-98 vol% were obtained by using the PU template (as shown in Figure 2.10).[110] SiOC foams having mesoporous structure and total porosity up to 98 vol% were obtained by hydrogen fluoride (HF) etching. While a 43 m^2/g SSA was obtained with 1 h of etching, a high SSA of up to 147 m^2/g was obtained with 24 h of etching.[111] Additionally, a hierarchical SiOC structure was created by infiltration of green matrix foam with a second slurry to obtain results with 2.5 mm and 0.29 mm for matrix and infiltrated foams.[112] In another study,[113] SiC nanowires decorated in the SiOC foams were obtained as increments in the total porosity ~77-85 vol% and SSA of 0.5-45 m^2/g with the increase of the pyrolysis temperature (from 1000 ^oC to 1400 ^oC) due to the SiC nanowires.

A disadvantage of the replica technique is the formation of hollow struts that affect the mechanical properties of materials due to the decomposition of the template. However, porous PDC foams with not only hollow but also dense struts have been produced by the replica technique.[108,111,114–116] The processing conditions to obtain reticulated SiOC foams with dense and hollow struts were studied.[13] Crosslinking conditions (temperature and time) of the preceramic polymer blend were changed deliberately, which resulted in the SiOC foam having hollow and dense struts. At a higher temperature (220 °C), curing was faster than it had been at a relatively lower temperature (80 °C + R.T.), and the PU did not swell the preceramic solution. During pyrolysis, the PU struts that were just coated with the preceramic solution decomposed and left hollow struts. When curing was done at a lower temperature (80 °C + R.T.), the

impregnation process happened slowly, providing the preceramic solution enough time to swell by PU and create dense struts.

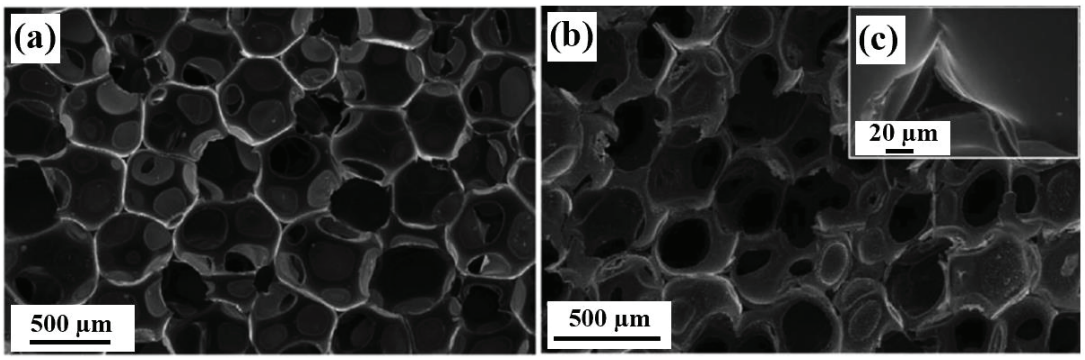

Figure 2.10. SEM images of (a) PU template including partially closed cells, and (b) SiOC foam with (c) inset showing the cross-section of the strut. (Source: Santhosh, B et al., 2020)[110]

SiOC foams having a total porosity of 75-79 vol% were produced utilizing pinewood as a template.[117] When the pyrolysis temperature was increased from 900 °C to 1100 °C, the compressive strength increased from 0.5 MPa (total porosity of ~75 vol%) to 4.5 MPa (total porosity of ~79 vol%). Enhanced mechanical properties of foams pyrolyzed at higher temperatures were explained by the densification of the struts. In other studies, SiOC and SiBCO foams were obtained by using mesoporous CMK-3 and poly(melamine-formaldehyde).[118,119]

Table 2.5. Properties of porous PDCs produced by replica technique.

Formed PDCs / Template	Pore properties	Other properties	Possible applications	Ref.
SiOC foam / PU sponge	ϕ_T = 91-98% SSA ~ 0.39-79.21 m^2/g Ø ~ 656-779 µm	σ_c = 0.2-0.9 MPa k_1 = 0.28 x 10^{-9}-11.48 x 10^{-9} m^2 k_2 = 0.34 x 10^{-5}- 54.17 x 10^{-5} m	High temperature filtration, catalytic support	13
SiOC foam / PU sponge	ϕ_T = 95-98% SSA ~ 4-147 m^2/g Ø ~ 3-4 nm	σ_c = 0.07-0.25 MPa	N.A.	111

(cont. on next page)

Table 2.5 (cont.)

SiOC foam / PU sponge	Ø ~ 353-381 μm	σ_c ~ 0.44-0.94 MPa E ~ 52-134 MPa	N.A.	[108]
SiOC foam / PU sponge	Ø ~ 290-2500 μm	N.A.	N.A.	[112]
SiOC & SiCN(O) foams / PU sponge	ϕ_T = 75-98%	α_l ~ 1.72 x 10^{-6} - 1.93 x 10^{-6} K^{-1} λ ~ 0.03-0.20 $W \cdot m^{-1} \cdot K^{-1}$ (@R.T.) D ~ 1.6 x 10^{-2}-2.1 x 10^{-2} cm^2/s (@1000 °C)	N.A.	[110]
SiOC+SiC nanowire foam / PU sponge	ϕ_T ~ 76-85% SSA ~ 0.5-45 m^2/g	N.A.	N.A.	[113]
SiOC foam / Pinewood	ϕ_T ~ 75-79% SSA ~ 25-99 m^2/g	σ_c = 0.5-4.5 MPa	Adsorption, filtration, catalytic support	[117]
SiOC / mesoporous carbon CMK-3	Ø = 2.74-3.30 nm SSA = 602-616 m^2/g	σ_c = 15.84-24.30 MPa	Catalysis	[118]
SiC foam / PU sponge	ϕ_T ~ 87-98% SSA ~ 0.13-0.31 m^2/g	σ_c = 0.17-0.75 MPa E = 2.7-11.7 GPa λ = 0.05-0.12 $W \cdot m^{-1} \cdot K^{-1}$ (@R.T.) q_m = 192-2317 ng/g	Adsorption for drugs	[114,116]
SiBOC foam / PMF foam	ϕ_T ~ 82-92% ρ_b = 0.18-0.39 g/cm^3 Ø = 1-5 μm & 100-400 μm	σ_c = 0.3-0.87 MPa E = 4-12 MPa λ = 0.08-0.13 $W \cdot m^{-1} \cdot K^{-1}$ (@R.T.)	Thermal protection system	[119]

N.A. = not available, Ø = pore diameter, ϕ_T = total porosity, SSA = specific surface area, ρ_b = bulk/apparent density, k_1 = Darcian permeability, k_2 = non-Darcian permeability, σ_c = compressive strength, E = Young's modulus, λ = thermal conductivity, q_m = adsorption capacity, α_l = thermal expansion coefficient, D = thermal diffusivity, E = Young's modulus.

2.2.1.1.2. Additive Manufacturing

Additive manufacturing (AM) is a novel technology that allows the production of porous materials in demanded properties (porosity, cell, and strut sizes, etc.). Design freedom makes sophisticated shapes possible and yields fewer imperfect structures, resulting in increased strength. To date, numerous types of AM have been developed to produce cellular PDCs including stereolithography (SLA),[49,120] selective laser sintering (SLS),[121] binder jetting,[122] direct ink writing (DIW),[123] and digital light processing

(DLP).[124,125] Table 2.6 summarizes properties of the porous PDCs produced by additive manufacturing.

Among AM techniques, DIW is one of the most widely used due to its simplicity in terms of processing conditions. Pure SiOC cellular structures having a total porosity of ~64 vol% with compressive strength of ~2.5 MPa were produced by using DIW. The addition of graphene oxide (0.025-0.1 wt% GO) allowed for reduced shrinkage of the preceramic polymer, resulting in SiOC with thicker struts and higher compressive strength of ~3.1 MPa (with 0.1 wt% GO, as depicted in Figure 2.11) compared to GO-free samples.[126] In addition, Figure 2.12 shows that SiOC scaffolds with hierarchical porosity were fabricated using different amounts (50-80 vol%) and particle sizes of PMMA microbeads (0.46, 5, 10, 25, and 50 μm). The amount and size of PMMA microbeads affected the main properties of the structure, and compressive strength was obtained up to ~8.19 MPa when 0.46 μm microbeads were used.[127] The same research group showed that SiOC components with different patterns (filament size, pore size, and angle of deflection between layers) affect the properties such as mechanical strength and gas permeability.[128] Ceramic matrix composites with complex shapes were produced using carbon fibers as reinforcement by DIW. Since fiber addition caused cracks perpendicular to the filament axis, the formation of cracks was mostly prevented by adding SiC powder to the ink as a passive filler.[123]

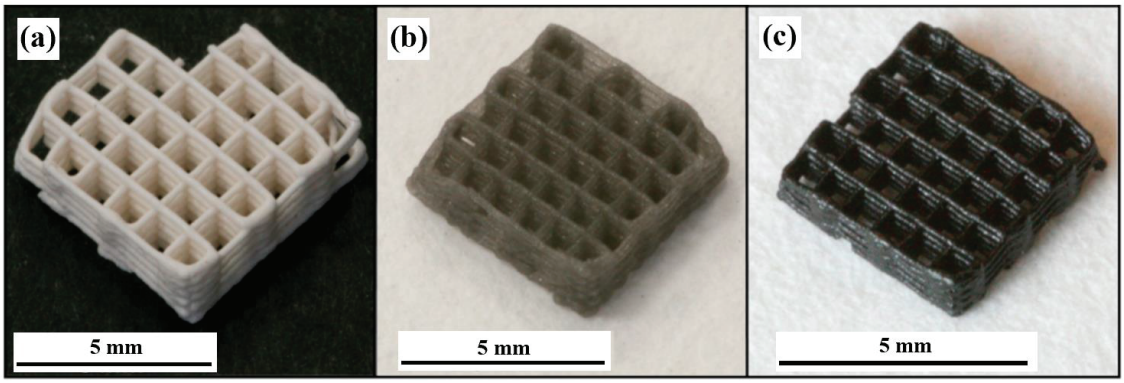

Figure 2.11. Optical images of SiOC cellular structures using 0.1 wt% GO: (a) as printed, (b) after crosslinking, and (c) after pyrolysis. (Source: Pierin, G et al., 2016)[126]

SiOC components with different designs having a total porosity of 82-91 vol% and ~93 vol% were produced by DLP and SLA.[124,129] Additionally, SiOC ceramics based on Kagome lattice were successfully produced with a total porosity of up to 80 vol% using commercial preceramic polymer and different printing solvents.[130]

SiOC cellular structures with hollow struts were produced by a two-step process including printing commercial filaments with fused filament fabrication (FFF) and impregnation of printed structure with preceramic polymer blend.[131] The same research group developed SiOC(N) scaffolds having cell sizes of 1.2 mm and compressive strength up to 24 MPa with dense struts.[132] The scaffolds are expected to enhance the mechanical strength to be used in bone regeneration applications. Hence, obtained SiOC(N) scaffolds were tested for biocompatibility in the bone tissue regeneration process.[132,133]

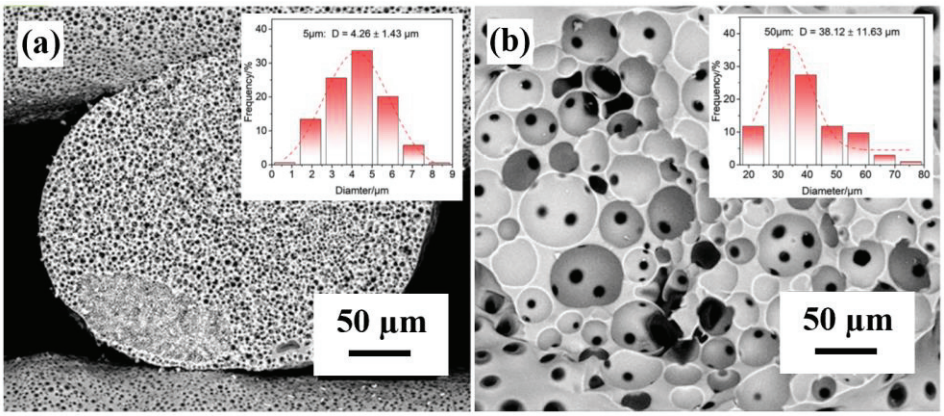

Figure 2.12. SEM images of obtained SiOC components with 80 vol% PMMA microbeads sizes of (a) 5 μm, and (b) 50 μm. The insets show the pore size distributions. (Source: Huang, K et al., 2020)[127]

Table 2.6. Properties of porous PDCs produced by additive manufacturing.

Formed PDCs	Pore properties	Other properties	Possible applications	Ref.
SiOC	ϕ_T ~ 80%	N.A.	N.A.	130
SiOC	ϕ_T ~ 93%	σ_c ~ 0.69 MPa	N.A.	129
SiOC	ϕ_T ~ 82-91%	σ_c ~ 3.8-10 MPa E ~ 0.9-3.1 GPa	N.A.	124

(cont. on next page)

Table 2.6 (cont.)

SiOC	ϕ_T ~ 70-88% Ø ~ 0.29-38.13 μm	σ_c ~ 0.94-8.19 MPa	Catalyst support, biomedical component, energy device	127
SiOC	ϕ_T ~ 50-75%	σ_c ~ 4.8-154.6 MPa k_1 ~ 1.41 x 10^{-9}- 3.42 x 10^{-9} m^2 k_2 ~ 1.87 x 10^{-4}- 4.60 x 10^{-4} m	Gas filtration, catalysis	128
SiOC	ϕ_T ~ 64%	σ_c ~ 2.51 MPa	N.A.	126
SiOC	Ø ~ 250 μm	N.A.	Heat exchange, chemical/gas filter	131
SiOC	ρ_b ~ 0.06-0.80 g/cm^3	σ_c ~163.3 MPa (@0.80 g/cm^3)	High temperature applications	49
SiOC	ϕ_T ~ 75%	σ_c ~3.80 MPa	N.A.	123
SiOC	ϕ_T ~ 3-11%	σ_c ~ 1.54-19.08 MPa E ~ 1.8-94.8 GPa	N.A.	14
SiOC(N)	Ø ~ 300-500 μm & 1.2 mm	σ_c ~ 22-24 MPa	Bone regeneration	132,133
SiCN	ϕ_T ~ 7-13% ρ_b ~ 1.98-2.17 g/cm^3	E ~ 12.5-32.5 GPa	Microwave absorbent	134
SiCN	ϕ_T ~ 4-5% ρ_b ~ 2.04-2.12 g/cm^3	E ~ 10-55 GPa	Electromagnetic wave absorbent	135
SiCN	ϕ_T ~ 93% Ø ~ 2200 μm	σ_c ~ 0.18 MPa E ~ 5.8 MPa	N.A.	136
SiC	ϕ_T ~ 10-70%	σ_c ~ 5-24 MPa	N.A.	121

N.A. = not available, Ø = pore diameter, ϕ_T = total porosity, ρ_b = bulk/apparent density, σ_c = compressive strength, E = Young's modulus, k_1 = Darcian permeability, k_2 = non-Darcian permeability.

2.2.1.2. PDC Aerogels

Aerogels are highly porous and thus extremely light components that consist of mostly air in their 3D solid networks. Since aerogels were first discovered by Kistler in 1931,[137] considerable research has been devoted to exploring novel compositions and unique properties of aerogels that include very low density (< 0.5 g/cm^3), high porosity (usually > 90%), high surface area (usually ~ 100-1000 m^2/g) and low thermal conductivity (< 0.05 $W \cdot m^{-1} \cdot K^{-1}$ @R.T.). These properties ensure aerogels hold widespread attention in applications such as thermal insulation,[138,139] wastewater treatment,[140,141] energy storage,[142] and sensor applications[143–146] among many others.

Besides the widely investigated silica and carbon-based aerogels, there are various other aerogel compositions including but not limited to polymers

[polyvinylchloride,[147] polyimide,[148–150] polyvinylidene fluoride,[151] composites (polyvinylidene fluoride/silica,[152] polymethyl methacrylate/silica)[153]], and ceramics (Si_3N_4,[154,155] SiC,[156] yttria-stabilized zirconia[157]). Recent research indicates that, due to the inherent difficulty to process ceramics as aerogels by conventional ceramic process, compositional variety is still not widely available.[158] On the other hand, it is possible to produce various PDC aerogels by sol-gel or using commercial preceramic polymers because the PDC route has distinct advantages. One such advantage is that preceramic precursors have low processing temperatures; therefore, they can be formed easily by cost-effective techniques (compression/injection molding, spinning, extrusion, etc.). Additionally, sintering additives are not required, and they demonstrate improved creep resistance with high thermal stability up to 1200 °C.[66,79]

Generally speaking, aerogels are synthesized by the sol-gel technique which is defined by IUPAC as "Process through which a network is formed from solution by a progressive change of liquid precursor(s) into a sol, to a gel, and in most cases finally, to a dry network".[159] The main steps of this process consist of sol-gel preparation, aging, and drying. Gel formation starts with the precursor hydrolysis/condensation reactions, resulting in dispersion of the colloidal particles in the solution, called *sol*. Condensation reactions continue and a network of colloidal particles occurs, called *gel*. In the aging step, the silica network is reinforced by aggregating particles. The last and most significant step is *drying*. The purpose of the drying process is to remove the solvent from the gel and depending on the drying path chosen, xerogels, cryogels, or aerogels can be produced by ambient pressure drying, freeze drying, or supercritical drying, respectively. In ambient pressure drying, the solvent is removed by evaporation under atmospheric pressure and at low temperatures. The solid structure is exposed to unconstrained shrinkage during the drying stage because of the high surface tension of the solvent and capillary forces. Therefore, drying time/conditions should be controlled to minimize the defects caused by the collapse. In freeze drying, the solvent is first frozen and then removed by sublimation to obtain a cryogel. The most widely used method among drying methods is supercritical drying. In this method, the solvent is removed under supercritical conditions (i.e., higher than critical temperature and the pressure of the solvent used) without collapse of the pores to obtain aerogel. This drying technique aims to minimize the shrinkage which is caused by the capillary force. For this purpose, a solvent with low surface tension is selected in the structure to reduce the liquid/vapor interface energy. CO_2 is the most widely used solvent because of its cost-

effectiveness, non-toxicity, and simple requirements to bring to supercritical conditions.[160] In this drying method, the wet gel is placed in a pressure vessel and filled with liquid CO_2, and then the solvent in the wet gel is periodically exchanged with liquid CO_2. The CO_2 reaches the supercritical state by bringing the pressure vessel to the critical temperature (31 ^oC) and pressure (7.35 MPa). Then the CO_2 is removed from the structure with low pressure (<1 bar/min). The CO_2 liquid-gas transition in this process is presented in Figure 2.13 (a). In the supercritical region, liquid/vapor interfacial tension is minimized since the surface tension reaches zero. Thus, the pore network is not exposed to any collapse or shrinkage without the presence of capillary forces. As seen in Figure 2.13 (b), freeze drying has the fastest drying time among all aforementioned drying methods while ambient pressure drying has the longest.

PDC aerogels are obtained by two methods: (i) sol-gel and (ii) preceramic polymer processing. These methods will be explained separately in the following subsections.

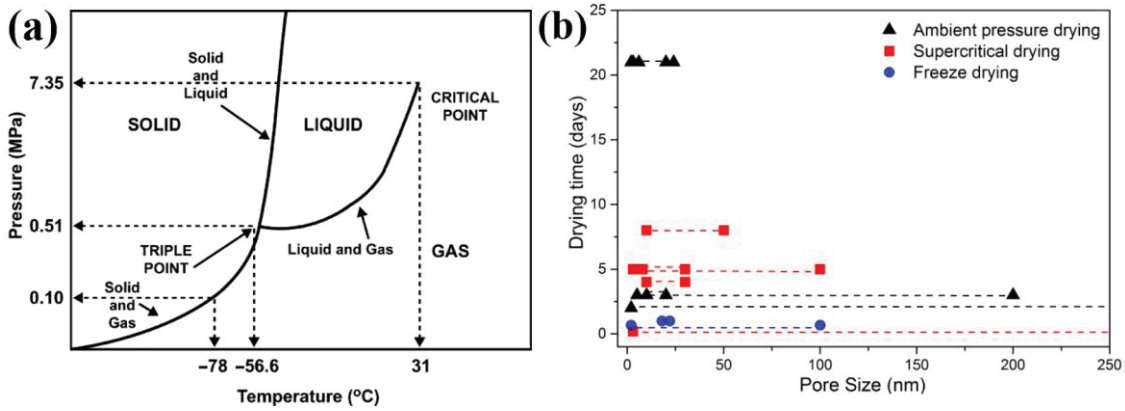

Figure 2.13. (a) Unary phase diagram of pressure (MPa) vs. temperature (°C) for CO_2 (Source: Werner, B G et al., 2006),[161] and (b) Effect of drying methods on PDC aerogel's pore size extracted from published studies. (Source: Vakifahmetoglu, C et al., 2021)[162]

2.2.1.2.1. Sol-gel Processing of PDC Aerogels

The first step in the sol-gel route for PDC aerogels is the synthesis of the required preceramic polymer using hybrid silicon alkoxides (tetraethylorthosilicate,[163–165] methyldimethoxysilane,[164] methyl-, ethyl-, propyl- and phenyl-trimethoxysilane,[163,164,166] etc.). After that, hydrolysis/condensation reactions take place, followed by crosslinking and drying steps.

There are both advantages and disadvantages to the production of PDC aerogels using sol-gel processing. The use of silicon alkoxide allows a wider composition range for the PDC aerogels. However, there are drawbacks due to their toxic properties and high cost. In addition, aerogels obtained via sol-gel processing usually have an SSA range of several hundred m^2/g and poor mechanical properties (brittleness) unless further processed. This creates difficulties for the post-processing of the aerogels and limits their widespread use.

Tables 2.7 and 2.8 summarize properties of the sol-gel synthesized PDC aerogels. For the sol-gel synthesized SiOC-based aerogels, pore sizes in the range of 2 to a few thousand nanometers and an SSA reaching 800 m^2/g were observed, as shown in Table 2.7. Ambient dried aerogels, called ambigels, were synthesized using silicon alkoxides [bis(triethoxysilyl)methane (BTEM), bis(triethoxysilyl)ethane (BTEE), and methyltriethoxysilane (MTES)] in a two-step sol-gel process (acid/base), followed by pyrolysis at 800-1400 ^oC.[167–169] SiOC ambigel (hereafter called aerogel, as seen in Figure 2.14) synthesized from BTEE was pyrolyzed at 800 ^oC in hydrogen and obtained an SSA up to 615 m^2/g.[169] In another study,[170] different precursors were tried with the two-step acid-base sol-gel to obtain monolithic SiOC aerogel, and the crack-free structure was obtained from triethoxyvinylsilane /tetraethoxysilane (VTES/TEOS).

SiOC aerogel synthesized from silicon alkoxide was obtained using CO_2 supercritical drying with an SSA reaching around 250 m^2/g.[171] In other interesting research,[172] drying of SiOC aerogel synthesized from TEOS was obtained by ethanol supercritical drying and obtained an SSA of up to ~200 m^2/g with thermal conductivity of 0.027 $W \cdot m^{-1} \cdot K^{-1}$ at R.T. The formation of several other PDC aerogels was also achieved by the sol-gel process.[173–175]

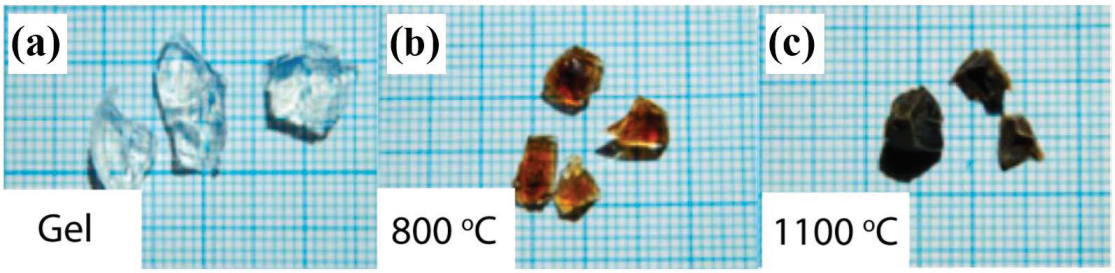

Figure 2.14. Optical microscope images of (a) gel, and SiOC aerogels pyrolyzed at (b) 800 °C, and (c) 1100 °C. (Source: Dire, S et al., 2015)[169]

Table 2.7. Properties of sol-gel synthesized SiOC-based aerogels. (Source: Vakifahmetoglu, C et al., 2021)[162]

PDC aerogel	Processing parameters			Pore properties	Other properties	Possible applications	Ref.
	Solvent	Drying method	Pyrolysis				
SiOC	IPA	Ambient pressure (21 days/ 50 °C)	1000°C 3h Ar	Ø ~ 3-24 nm SSA = 132-452 m^2/g V_{pore} = 0.33-0.89 cm^3/g	N.A.	N.A.	167
SiOC	IPA	Ambient pressure (21 days/ 50 °C)	1400°C 3h Ar	Ø = 2-20 nm SSA = 150 m^2/g V_{pore} = 0.19 cm^3/g	τ_{resp} = 4 min (@5ppm NO_2) 5 min. (@5000 ppm H_2) τ_{rec} = 2 min. (@5ppm NO_2) 1 min. (@5000 ppm H_2)	Gas sensor (NO_2, H_2, detection)	168
SiOC	IPA	Ambient pressure (21 days/ 50 °C)	800 - 1100°C 1h H_2	Ø ~ 2-6 nm SSA = 171-615 m^2/g V_{pore} = 0.18-0.58 cm^3/g ρ_b ~ 0.90-1.30 g/cm^3	R = 55-78 % (@ > 600 nm) R = 20-67 % (@ 400 nm)	Optical sensor	169

(cont. on next page)

Table 2.7 (cont.)

SiOC	IPA	Ambient pressure (2 days/ 60 °C)	1000 °C 1h Ar	Ø = 2 nm & 95-350 nm SSA = 354-488 m^2/g ρ_b = 0.27-0.34 g/cm^3	σ_c = 1.45-3.17 MPa	N.A.	[170]
SiOC	EtOH	Supercritical drying [CO_2] (4 h/ 35°C/ 80 bar)	1000 - 1600 °C 1h Ar	Ø = 10-1000 nm SSA = 10-247 m^2/g	N.A.	N.A.	[171]
SiOC	EtOH & HCl acid	Supercritical drying [CO_2]	1000 °C 2h Ar	Ø ~ 9 nm SSA =531 m^2/g V_{pore} = 0.97 cm^3/g ρ_b = 0.4 g/cm^3	E = 1.42 GPa G = 0.54 GPa	N.A.	[176]
SiOC	IPA	Supercritical drying [EtOH]	1200 °C 1h Ar	Ø = 56 nm SSA = 198 m^2/g V_{pore} = 0.65 cm^3/g ρ_b = 0.3 g/cm^3	λ = 0.027 $W \cdot m^{-1} \cdot K^{-1}$ @R.T.	Thermal insulation	[172]
SiOC/ BN	Nhex	Ambient pressure (3 days/ 60 °C)	900 - 1300 °C 2h N_2	Ø = 10-20 nm & < 69 nm SSA = 27-566 m^2/g V_{pore} = 0.26-1.12 cm^3/g ρ_b = 0.36-0.89 g/cm^3	λ ~ 0.040-0.200 $W \cdot m^{-1} \cdot K^{-1}$ @R.T. λ ~ 0.150-0.750 $W \cdot m^{-1} \cdot K^{-1}$ @1300 °C σ_c = 2.2-20.3 MPa	Thermal insulation	[173]
SiBOC	EtOH	Supercritical drying (N.A.)	1200 °C	Ø = 10-150 nm SSA = 293 m^2/g	λ = 0.138 $W \cdot m^{-1} \cdot K^{-1}$ (in vacuum @1500°C) σ_c ~ 1.849 MPa, ε ~ 20%	Thermal insulation	[174]
SiOCN	EtOH	Freeze drying & Vacuum drying (80 °C)	450 - 900 °C 2h N_2	Ø ~ 3-12 nm SSA ~ 25-827 m^2/g	η = -8-75.9 %	Volatile carbonyl compound adsorbent & cigarette smoke filter	[175]

N.A. = not available, Ø = pore diameter, SSA = specific surface area, V_{pore} = Pore volume, ρ_b = bulk/apparent density, σ_c = compressive strength, ε = strain, λ = thermal conductivity, E = Young's modulus, G = shear modulus, τ_{resp} = response time, τ_{rec} = recovery time, R = reflectance, EtOH = ethanol, HCl acid = hydrochloric acid, IPA = isopropanol, Nhex = n-hexane.

Table 2.8 summarizes properties of sol-gel synthesized SiC-based aerogels. After the gels obtained from resorcinol-formaldehyde/silica composite (RF/SiO_2) using the sol-gel process were dried with CO_2 supercritical drying, RF/SiO_2 aerogels produced were converted to SiC & SiC/C aerogels after subsequent processes (carbonization, magnesiothermic reaction, and carbothermal reduction, etc.).[177–179] In other studies, SiC & SiC/C based composite aerogels were obtained from the carbothermal reduction of phenyl-bridged polysilsesquioxane (with/without nanoclay mineral) having an SSA around 2000 m^2/g.[180–182]

SiC/mullite composite aerogel having an SSA of ~70 m^2/g [heat treatment at 1400 ^oC, mullite formation temperature, as seen in Figure 2.15 (b)] produced from catechol formaldehyde/silica/alumina hybrid aerogel [$CF/SiO_2/AlOOH$, as seen in Figure 2.15 (a)] via the sol-gel method and CO_2 supercritical drying. After heat treatment at 1450 ^oC, an SSA reached 300 m^2/g due to the composition of mullite.[183] $SiC/C/SiO_2$ composite aerogels having an SSA up to 500 m^2/g were produced with a sol-gel polymerization process and ambient pressure drying.[184,185]

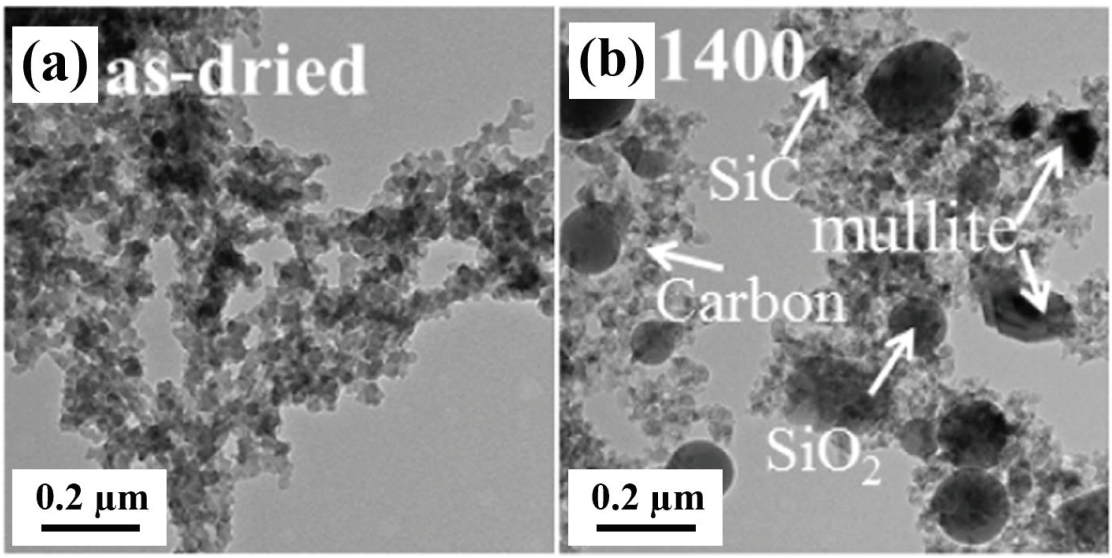

Figure 2.15. TEM images of (a) as dried, and (b) SiC/mullite composite aerogel (pyrolyzed at 1400 ^oC). (Source: Xie, M et al., 2017)[183]

Table 2.8. Properties of sol-gel synthesized SiC-based aerogels.

(Source: Vakifahmetoglu, C et al., 2021)[162]

PDC aerogel	Processing parameters			Pore properties	Other properties	Possible applications	Ref.
	Solvent	Drying method	Pyrolysis				
SiC	ACE	Supercritical drying [CO_2]	700 °C 12h Ar	Ø ~ 9 nm SSA = 232 m^2/g ρ_b ~ 0.157 g/cm^3	E_g = 3.2 eV	Catalytic, electronic, photonic, and thermal applications	177
SiC & SiC/C	EtOH	Supercritical drying [CO_2]	1500 °C 5h Ar	ϕ_T ~ 91-95 % Ø = 1-27 nm SSA = 251-892 m^2/g V_{pore} = 0.97-2.6 cm^3/g	N.A.	Various	178,179
SiC & SiC/C	DMF & DMA	Ambient pressure (1 day/60°C)	1200 - 1500 °C 4h Ar	ϕ_T = 91 % SSA = 796-1050 m^2/g V_{pore} = 0.64-0.80 cm^3/g	N.A.	Various	180,181
SiC/C	IPA	Supercritical drying [CO_2]	1500 °C 4h Ar	ϕ_T ~ 95-97 % SSA ~ 1155-2258 m^2/g V_{pore} = 3.57-6.14 cm^3/g	N.A.	Helium storage and catalysis	182
SiC/ mullite	EtOH	Supercritical drying [CO_2]	1250 - 1450 °C 5h Ar	Ø ~ 6-11 nm SSA = 67-301 m^2/g V_{pore} = 0.17-0.90 cm^3/g	N.A.	N.A.	183
SiC/C/ SiO_2	EtOH	Supercritical drying [CO_2]	1300 - 1500 °C 5h Ar	ϕ_T ~ 83-89 % Ø ~ 5-9 nm SSA = 144-746 m^2/g V_{pore} = 0.34-1.02 cm^3/g	λ = 0.035-0.053 $W \cdot m^{-1} \cdot K^{-1}$ @R.T. σ_c ~ 0.52-1.86 MPa	Thermal insulation	186

(cont. on next page)

Table 2.8 (cont.)

SiC/C/ SiO_2	IPA	Ambient pressure (~3-4 days/ R.T.-140 °C)	1500 °C 5h Ar&N_2	ϕ_T ~86 % SSA = 366-490 m^2/g	λ ~ 0.121 $W \cdot m^{-1} \cdot K^{-1}$ @R.T. σ_c ~ 1.5 MPa E = 76 MPa	N.A.	184,185
Si_3N_4	EtOH	Supercritical drying [CO_2] (4 h/ 50°C/ 100 bar)	1400 -1550 °C 5h N_2	Ø < 5 nm & >200 nm SSA = 189-638 m^2/g V_{pore} = 0.84-1.74 cm^3/g ρ_b = 0.121-0.312 g/cm^3	λ = 0.045-0.061 $W \cdot m^{-1} \cdot K^{-1}$ @R.T.	Thermal insulation	155

N.A. = not available, Ø = pore diameter, ϕ_T = total porosity, SSA = specific surface area, V_{pore} = Pore volume, ρ_b = bulk/apparent density, σ_c = compressive strength, λ = thermal conductivity, E = Young's modulus, E_g = direct band gap, ACE = acetone, EtOH = ethanol, IPA = isopropanol, DMF = N,N-dimethylformamide, DMA = N,N-dimethylacetamide.

2.2.1.2.2. Preceramic Polymer Processing of PDC Aerogels

PDC aerogels have also been produced using commercial preceramic polymers rather than sol-gel synthesized precursors.[187–189] In terms of production time, starting from the silicon alkoxides, roughly three weeks are required to obtain aerogel from the sol-gel process including drying at ambient pressure conditions and several washing steps.[167–169] On the other hand, PDC aerogels are obtained via preceramic polymer processing in about a week. The production time is remarkably shorter as commercially available preceramic polymers (polysiloxane, polysilazane, polycarbosilane, etc.) are used without the need to synthesize the starting precursor. The crosslinking process of preceramic polymers is carried out in an autoclave or a closed system to maintain the solvent in the system. After obtaining the wet gel, the yielding material is periodically washed with fresh solvent to remove the unreacted precursors or catalyst, etc. Subsequently, the drying process (ambient pressure, supercritical, or freeze) was applied, followed by pyrolysis.

The microstructure of the PDC aerogels varies depending on the type of solvent used and the amount of dilution. Polymeric aerogels (PMHS/DVB) with different solvents (cyclohexane, tetrahydrofuran, n-hexane, and acetone) were produced using CO_2 supercritical drying.[190] In the same study, it was claimed that swelling and solubility of the crosslinked preceramic polymer in different solvents affect the pore properties of the PDC. The highest SSA was obtained as 392 m^2/g of polymeric aerogel using acetone with an average pore size of 18.8 nm. Acetone was followed by n-hexane, tetrahydrofuran, and cyclohexane.

Tables 2.9 through 2.11 summarize properties of the PDC aerogels obtained from commercial preceramic polymer. For SiOC-based aerogels obtained from commercial preceramic polymers, an SSA reaching 500 m^2/g was observed, as shown in Table 2.9. Commercial polysiloxane, i.e., PHMS, was crosslinked with a crosslinking agent [tetravinylcyclotetrasiloxane (TMTV) or divinylbenzene (DVB)] via hydrosilylation reaction in the presence of a catalyst to produce SiOC aerogel with supercritical drying.[187,191–193] In another study,[187] crosslinking of the precursor was carried out at 150 °C in an autoclave and obtained wet gel was dried using CO_2 supercritical drying. Polymeric aerogel was pyrolyzed at 1000 °C to produce SiOC aerogel (carbon-rich). While the SSA of the polymeric aerogel was 227 m^2/g, the SSA of the SiOC aerogel decreased to 180 m^2/g during the polymer to ceramic transition. In another study,[191] SiOC aerogel having an SSA of 64 m^2/g and mesopores of 10-50 nm (no micropore) was obtained by the pyrolysis of polymeric aerogel at 1300 °C [as shown in Figure 2.16 (a)]. It was shown that micro and small mesopores (< 10 nm) were created with an SSA up to 530 m^2/g after SiOC aerogel was etched with HF (by the dissolution of the SiO_2-based phase), as shown in Figure 2.16 (b).

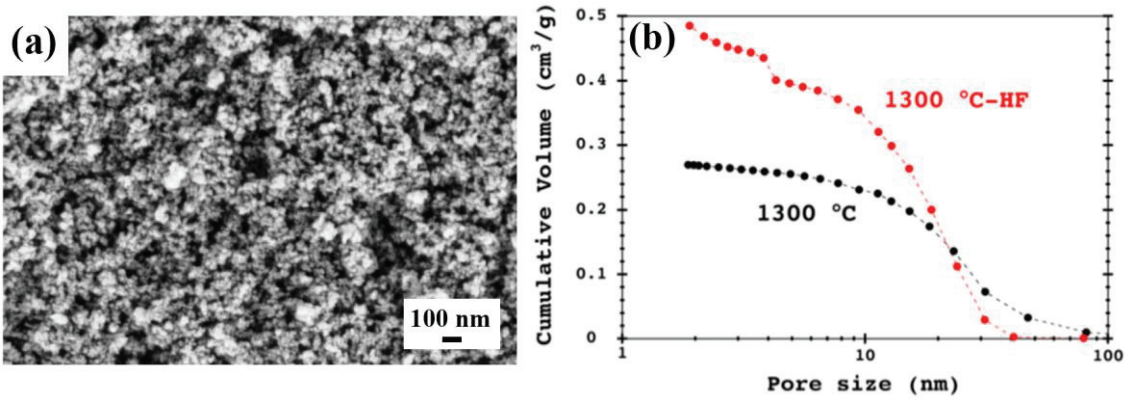

Figure 2.16. (a) SEM image of SiOC aerogel (pyrolyzed at 1300 °C), and (b) Cumulative pore volume vs. pore size of the SiOC aerogel before and after HF etching. (Source: Assefa, D et al., 2016)[191]

Table 2.9. Properties of SiOC-based aerogels obtained from commercial preceramic polymers. (Source: Vakifahmetoglu, C et al., 2021)[162]

PDC aerogel	Processing parameters			Pore properties	Other properties	Possible applications	Ref.
	Solvent	Drying method	Pyrolysis				
SiOC	ACE	Supercritical drying [CO_2] (8 days/ 41°C/ 95 bar)	1200 - 1300°C 5h Ar	Ø <10 nm &10-50 nm SSA = 33-530 m^2/g V_{pore} = 0.14-0.65 cm^3/g	N.A.	N.A.	191
SiOC	ACE	Supercritical drying (N.A.)	800 - 1600°C 2h N_2	SSA = 48-227 m^2/g V_{pore} = 0.18-0.29 cm^3/g ρ_b ~ 0.51-1.14 g/cm^3	N.A.	N.A.	193
SiOC	ACE & Cy	Supercritical drying [CO_2] (4 days/ 45°C)	900°C 1-7h Ar & H_2/Ar	Ø < 10 nm & 20-30 nm SSA = 87-215 m^2/g V_{pore} = 0.15-0.87 cm^3/g ρ_b ~ 0.65-0.98 g/cm^3	$Q_{reversible}$ ~ 900 $mAhg^{-1}$ (@C(360m Ag^{-1})) η = 35-52 %	Anode for Li-ion batteries	192

(cont. on next page)

Table 2.9 (cont.)

SiOC	ACE	Supercritical drying [CO_2]	1000ºC 1h Ar	Ø = 24 nm SSA = 180 m^2/g V_{pore} = 1.09 cm^3/g	$Q_{insertion}$ = 1280 $mAhg^{-1}$ $Q_{extraction}$ = 600 $mAhg^{-1}$ $Q_{irreversible}$ = 680 $mAhg^{-1}$ (@C(360mAg^{-1}) η = 47-99 %	Anode for Li-ion batteries	187
SiOC & SiC	ACE & Cy	Supercritical drying [CO_2]	900ºC 1h Ar	ϕ_T = 72-86 % Ø = 10-90 nm SSA = 102-163 m^2/g V_{pore} = 0.39-0.72 cm^3/g	R_{ads} = 100 % @C_o = 1 mg/L (SiOC & SiC) q_m = 44.2 mg/g (SiOC)	Water purification	194
SiOC & SiCN	ACE & Cy	Supercritical drying [CO_2] (5 days/ 45ºC/ 100 bar) & Ambient pressure (3 days)	900-1300ºC N_2 CO_2 NH_3	Ø = 5-200 nm SSA = 30-388 m^2/g V_{pore} = 0.21-0.84 cm^3/g ρ_b ~ 0.45-0.70 g/cm^3	q_m ~ 10 mg/g (Cr(III)) q_m ~ 20-30 mg/g (Cr(VI))	Water purification	195

N.A. = not available, Ø = pore diameter, ϕ_T = total porosity, SSA = specific surface area, V_{pore} = pore volume, ρ_b = bulk/apparent density, Q = specific capacity, η = efficiency, R_{ads} = % adsorbent, C_o = initial concentration, q_m = max. adsorption capacity, ACE = acetone, Cy = cyclohexane.

SiOC and SiCN aerogels were produced using CO_2 supercritical and ambient pressure drying under different atmospheres (N_2, CO_2, and NH_3), respectively.[195] The highest SSA of 388 m^2/g was obtained with SiCN aerogel pyrolyzed under an NH_3 atmosphere.

Table 2.10 summarizes properties of the SiCN-based aerogels obtained from commercial preceramic polymers. Polysilazane aerogels were obtained with the hydrosilylation reaction between polysilazane and DVB, followed by CO_2 supercritical drying, and were finally pyrolyzed at 1000-1500 ºC to produce monolith SiCN aerogels.[188] In the mentioned study, polysilazane aerogel with an SSA of 489 m^2/g decreased to 165 m^2/g and 153 m^2/g, by pyrolysis at 1000 and 1500 °C. N_2 adsorption-desorption isotherms with pore size distributions were given for polysilazane and SiCN aerogels in Figure 2.17. All aerogel samples showed mesoporous structure as shown in Figure 2.17 (a). While the polysilazane aerogel showed micropores (≤ 2 nm),

micropores collapsed during the polymer to ceramic transition, as shown in Figure 2.17 (b). However, the SiCN aerogel had mesopores around 30 nm which did not collapse during the transition.

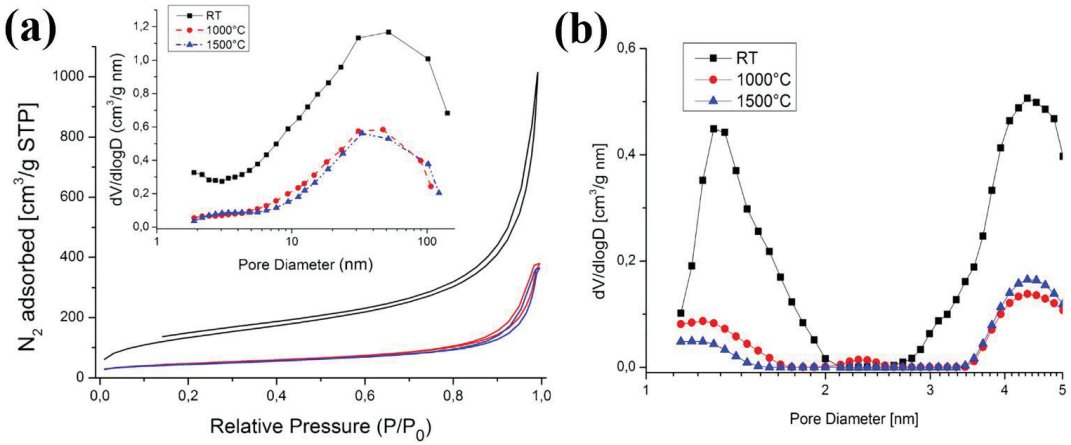

Figure 2.17. (a) N_2 sorption isotherms with BJH pore size distribution, and (b) QSDFT pore size distribution of polysilazane and SiCN aerogels pyrolyzed at 1000 ^oC and 1500 ^oC. (Source: Zera, E et al., 2015)[188]

It was shown that the change in solvent concentration in the aerogel caused differences in the pore properties. According to this research,[196] SiOCN aerogel was produced with different solvent amounts (85-95 vol%) using freeze drying. It was shown in Figure 2.18 that when the solvent amount was increased from 85 vol% to 95 vol%, the pore size increased (from 5-80 nm to 10-100 nm), and the bulk density decreased (from 0.25 g/cm^3 to 0.11 g/cm^3).

N-doped carbide-derived carbon (N-doped CDC) aerogel was produced using SiCN aerogel to be etched by chlorine. Such an aerogel sample with an SSA of up to 1890 m^2/g was tested for both CO_2 adsorption, and electric double-layer capacitor application.[197] SiBCN/graphene composite aerogel having an SSA reaching around 100 m^2/g was obtained through the crosslinking of polyborosilane with DVB using CO_2 supercritical drying, followed by pyrolysis at 1200 ^oC.[198] In addition to that, SiBCN-ZrO_2 hybrid ceramic aerogels were produced by the same method.[199]

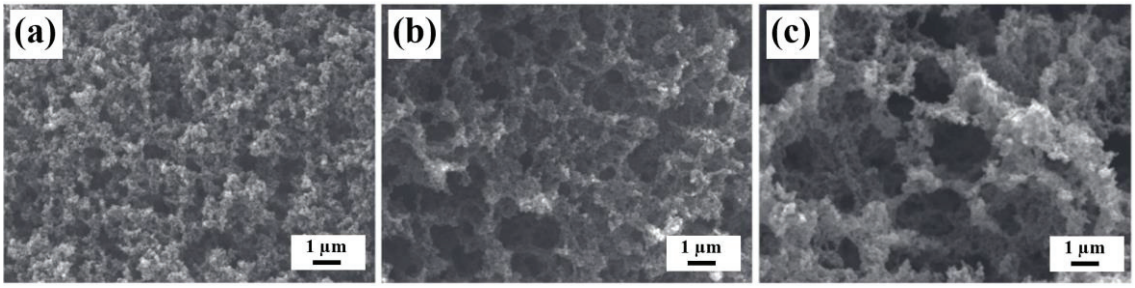

Figure 2.18. Field-emission scanning electron microscope (FE-SEM) images of SiOCN aerogels obtained with different solvent amounts: (a) 85 vol%, (b) 90 vol%, and (c) 95 vol%. (Source: Zhao, W et al., 2019)[196]

Table 2.10. Properties of SiCN-based aerogels obtained from commercial preceramic polymers. (Source: Vakifahmetoglu, C et al., 2021)[162]

PDC aerogel	Processing parameters			Pore properties	Other properties	Possible applications	Ref.
	Solvent	Drying method	Pyrolysis				
SiCN	Cy	Supercritical drying [CO_2] (4 days/ 50ºC/ 100 bar)	1000 - 1500ºC 1h N_2	ϕ_T = 95-96 % Ø ~ 30-40 nm SSA ~ 153-165 m^2/g V_{pore} = 0.56-0.58 cm^3/g	N.A.	N.A.	188
SiCN	Cy	Supercritical drying [CO_2] (5 days/ 45ºC/ 100 bar)	450 - 1000ºC 1h Ar	Ø = 3-100 nm SSA = 75-725 m^2/g V_{pore} = 0.24-0.83 cm^3/g	N.A.	N.A.	200
SiCN	Cy	Freeze drying (-78ºC/24h)	1000-1400ºC 2h N_2	Ø ~ 18-22 nm SSA ~ 106-235 m^2/g V_{pore} = 0.49-0.56 cm^3/g ρ_b ~ 0.19 g/cm^3	RL = -43.37 / -31. 69 dB d = 2-4.5 mm Effective bandwidth = 3.8-6.6 GHz	Electromag-netic wave absorbent	201
SiCN/ Co	Cy	Freeze drying (N.A.)	800ºC 2h N_2	Ø = 21-31 nm SSA = 54-109 m^2/g V_{pore} = 0.28-0.42 cm^3/g	RL = -38.29/-24.31 dB d = 0.9-1.6 mm Effective bandwidth = 5.5-10.9 GHz	Microwave absorbent	202

(cont. on next page)

Table 2.10 (cont.)

SiCN / N-doped CDC aerogel	Cy	Supercritical drying [CO_2] (5 days/ 45°C/ 100 bar)	450 - 1200°C 1h Ar	SSA = 706-1887 m^2/g V_{pore} = 0.21-0.97 cm^3/g	CO_2 adsorption 3.96 - 4.67 mmol g^{-1} @1bar, 0°C Specific capacity ~140 F g^{-1} @10 A g^{-1} for 5000 cycles	Adsorbent for CO_2 and EDLC	[197]
SiCN (O)	Cy & DBE	Supercritical drying [CO_2] (43°C/ 100 bar)	1000 - 1600°C 1h N_2	Ø = 1-48 nm SSA ~ 9-129 m^2/g V_{pore} = 0.04-1.05 cm^3/g	N.A.	N.A.	[203]
SiOCN	Cy	Freeze drying (-75°C/16h)	1000°C 2h N_2	Ø = 2-100 nm SSA = 114-134 m^2/g V_{pore} = 0.43-0.49 cm^3/g ρ_b ~ 0.11-0.25 g/cm^3	N.A.	Catalysis, separation, and sorption	[196]
SiBCN / graphene	THF	Supercritical drying [CO_2]	800 - 1200°C 1h N_2	Ø ~ 5 nm SSA ~ 102 m^2/g V_{pore} = 1.43 cm^3/g	σ_c ~ 0.2 MPa	N.A.	[198]
SiBCN / ZrO_2	THF	Supercritical drying [CO_2]	750 - 1550°C 1h N_2	Ø = 10-70 nm SSA ~ 108-211 m^2/g V_{pore} = 0.49-1.57 cm^3/g	N.A.	N.A.	[199]

N.A. = not available, Ø = pore diameter, ϕ_T = total porosity, SSA = specific surface area, V_{pore} = pore volume, ρ_b = bulk/apparent density, RL = reflection loss, d = absorbent thickness, σ_c = compressive strength, Cy = cyclohexane, DBE = Dibutyl ether, THF = tetrahydrofuran.

Table 2.11 summarizes properties of the SiC-based aerogels obtained from commercial preceramic polymer. Carbon-enriched SiC/C aerogels [as depicted in Figure 2.19 (a)] were produced through the crosslinking of polycarbosilane with DVB (via the hydrosilylation reaction) using CO_2 supercritical drying, followed by pyrolysis at 1000-1500 °C under Ar flow.[189] The pore size distributions of polycarbosilane and SiC/C aerogels are given with N_2 adsorption/desorption isotherms in Figure 2.19 (b). All aerogels showed type IV isotherms with pore sizes between 50-1000 Å (around 500 Å).

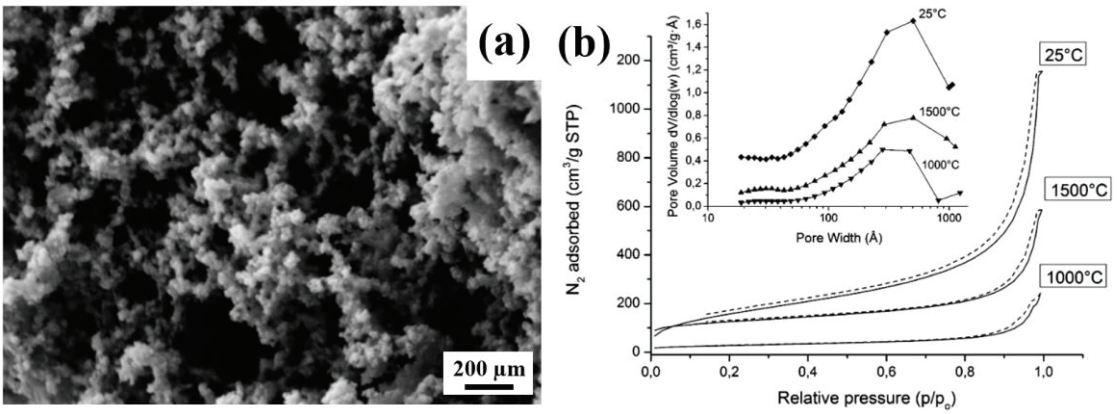

Figure 2.19. (a) SEM image of SiC/C aerogel (pyrolyzed at 1500 °C), and (b) N_2 sorption isotherms with the pore size distribution of polycarbosilane and SiC/C aerogels (1000 ºC and 1500 ºC). (Source: Zera, E et al., 2014)[189]

Table 2.11. Properties of SiC-based aerogels obtained from commercial preceramic polymers. (Source: Vakifahmetoglu, C et al., 2021)[162]

PDC aerogel	Processing parameters			Pore properties	Other properties	Possible applications	Ref.
	Solvent	Drying method	Pyrolysis				
SiC & BN	N.A.	Freeze drying (N.A.)	1400 - 1500ºC 1-3h Ar	ρ_b ~ 0.0001 g/cm^3	λ ~ 0.020 W·m^{-1}·K^{-1} (air @R.T.) ν = -0.25 E = 25 kPa	Thermal insulation	204
SiC/ C	Cy	Supercritical drying [CO_2] (4 days/ 50ºC/ 100 bar)	1000 - 1500ºC 1h Ar	Ø ~ 7-500 nm ϕ_T = 90-93 % SSA = 96-444 m^2/g V_{pore} = 0.31-0.79 cm^3/g	σ_c ~ 1.6 MPa	High temperature sorption and catalysis	189
SiC/ TiO_2	THF	Supercritical drying [CO_2] (8h/ 45ºC/ 80 bar)	600 - 1200ºC 1h N_2	Ø ~ 23 nm SSA = 58 m^2/g V_{pore} = 0.22 cm^3/g	N.A.	Catalysis, separation, and sorption	205

N.A. = not available, Ø = pore diameter, ϕ_T = total porosity, SSA = specific surface area, V_{pore} = pore volume, ρ_b = bulk/apparent density, σ_c = compressive strength, λ =

thermal conductivity, ν = Poisson's ratio, E = Young's modulus, Cy = cyclohexane, THF = tetrahydrofuran.

The effect of supercritical drying temperature was examined for SiC-TiO_2 hybrid aerogels.[205] When the polymeric structure was supercritically dried at 40-45-50 ^oC (at 8.0 MPa), the obtained SSA values were 614.09, 614.47, and 603.91 m^2/g, respectively. In the mentioned study, the CO_2 supercritical drying temperature did not present a clear trend in the polymeric aerogel microstructure.

2.3. Applications of Porous PDCs

PDCs have a broad range of applications including gas sensors, catalysts, membranes, insulation, drug delivery, and scaffolds for biomaterials.[13,82,110,206–209] One of the earliest applications of porous ceramics and glasses could be found in the refractory industry where pores were used to dominate thermal conductivity and therefore improve energy efficiency. However, the literature, unfortunately, does not provide sufficient data on the thermal properties of the porous inorganic solids.[70] The same is also true for PDCs. Mechanical properties, chemical stability, oxidation resistance, and high-temperature creep behavior of PDCs have already been well-documented.[4,41,210–212] On the other hand, thermal properties at high temperatures are one of the least researched properties of PDCs.

Due to PDCs' high temperature stability as well as their chemical and oxidation resistance, PDCs can also be used as high temperature applications for thermal barriers, hot gas filtration, and catalyst supports.[59,68,110,213–218] For instance, PDCs are used as ceramic heating elements, namely, as glow plug applications in diesel engines. In fact, the PDC glow plug, which consists of polysiloxanes and other fillers, is the first industrial application of the material.[67,219] SiOC was developed to be used as a heating element in glow plugs for diesel engines due to its resistance to high temperatures.[219] The ceramic micro-igniter is another example of a high temperature application in which SiCON-based ceramic provides high heating rates, short response times, and a high number of heating cycles.[67]

Preceramic polymers are used to produce ceramic matrix composites (CMC). Brake components used in motorcycles, cars, and trains are some potential application areas of these composites. Carbon-ceramic brake discs [STARBlades®CMC (Starfire Systems Inc., USA)] were made of polycarbosilane, SiC (as filler), and carbon fibers (as reinforcement). When compared to metal brake discs, carbon-ceramic brake systems provide exceptional thermal handling, a longer lifetime due to less wear, and better moisture resistance.[8,67]

Porous PDCs are widely used in applications such as filtration (gas & molten metal), membrane, and insulation. Reticulated SiC foams were produced via the PDC route, and the thermal conductivity at R.T. was obtained as low as 0.05 $W \cdot m^{-1} \cdot K^{-1}$.[116] Slightly lower values were seen with reticulated SiOC foams (total porosity of 79-98 vol%) having a thermal conductivity of 0.03-0.16 $W \cdot m^{-1} \cdot K^{-1}$ at R.T.[110] At high temperatures, the thermal conductivity of dense hot-pressed SiOC was seen as 0.75 $W \cdot m^{-1} \cdot K^{-1}$ up to 1000 °C[220] which is lower than the thermal conductivity of SiC (35 $W \cdot m^{-1} \cdot K^{-1}$ at 1000 °C)[221] or Si_3N_4 (~16 $W \cdot m^{-1} \cdot K^{-1}$ at 1000 °C).[222] Moreover, it was found that an increase in the amount of precipitated carbon caused an increase in the thermal conductivity of SiOC.[223]

Apart from the aforementioned applications of PDCs, they are also used as gas or molten metal filters. These applications will be explained in detail in the subsections below.

2.3.1. Gas Filters

Refractory porous ceramics are widely used in fluid flow and separation applications where active components must withstand aggressive operational conditions, including chemical attacks and high temperatures or pressures. Well-established examples include the removal of slag and inclusions from molten metals, particulate filtration of hot gas streams, and the thermo-catalytic conversion of chemicals.[80,207,209,214,224–230] In these applications, a major operational cost is related to the power consumption of pumps, compressors, and blowers to force the permeation of liquids and gases through the porous ceramic matrix. Power consumption is directly proportional to the pressure drop resulting from the fluid flow, which in turn is

influenced by the operational conditions and by the permeability of the porous structure. By the correct manipulation of pore characteristics such as morphology, size, fraction, and pore topology, the permeability coefficients of the medium can be optimized during the processing step to help minimize the cost of operation. However, since the porous structure also affects other important properties, such as mechanical strength and thermal conductivity, a balance is required to provide the best overall performance for the porous component.[231] This balance can be achieved through the suitable combination of ceramic formulation and the processing methodology used to fabricate the porous matrix.[70,232] Materials selection for filtration at high temperatures must have specific properties, including enhanced mechanical strength.

It is known that 3D interconnected foams enable improved catalytic activity via diffusion path reduction and a higher degree of reactant mixing.[233] It was previously shown that foams deliver more efficient heat transfer compared to particle beds and honeycombs. In other words, foams offer better mass transfer/pressure drop tradeoff with the advantage of radial mixing; thus, they are highly suitable for applications such as gas filtration.[234,235]

2.3.2. Molten Metal Filters

In the foundry industry, the presence of impurities/residues in molten metals has been considered a critical harmful factor affecting many features of the metal including castability, mechanical strength, and machinability.[236–239]Accordingly, molten metal is filtered to enhance casting quality. Besides the removal of impurities (e.g., oxides, carbides, and other residues), filtration promotes turbulence reduction, i.e., ensuring laminar flow, to provide conditions for lessened cavity formation. For molten metal filtration, although different material types have been proposed for diverse filter shapes/forms in recent years, ceramics (e.g., SiC, Al_2O_3, and ZrO_2) have been widely accepted as the most promising due to their notable features such as high thermal shock resistance, mechanical strength, and chemical durability.[77,80,240,241] Generally, molten metal filters are designed and used either as cellular structures (extruded and pressed form) or foams.[242] Among those, foams have a high filtration capacity due to their reticulated (i.e., 3D interconnected porosity) structure.

2.3.3. Heat Exchangers

Having a tortuous flow path structure enables the open-cell materials to be used in high temperature heat transfer applications such as heat exchangers, industrial burners, and solar energy plants.[243,244] Heat exchange is a system to transfer heat energy from one medium to another. Different materials including polymers, metals, and ceramics are used as heat exchangers.[243] The most common among these are ceramics (e.g., SiC, Si_3N_4, and Al_2O_3) due to their high operating temperatures and resistance to corrosion.[245] Pelanconi et al. produced alumina lattices with different designs via the SLA technique and found that the lattices integrated into the tube improved the heat transfer with respect to the empty tube.[246] Microstructure heat exchangers provide a much larger specific heat transfer surface than conventional systems.[247] Micro alumina heat exchangers were produced with the help of the SLA technique and low-pressure injection molding (LPIM) process and obtained system provided heat exchange coefficients up to 15 $W \cdot m^2 \cdot K$.[247] In another study, counterflow, and crossflow micro alumina heat exchangers were fabricated with the same technology and showed heat exchange coefficients reaching 22 $W \cdot m^2 \cdot K$.[248] Some key parameters including thermal conductivity and mechanical strength are also required for producing a suitable heat exchanger.[249]

To the best of our knowledge, limited studies are focusing on the application, especially high temperature, of PDC components. Therefore, in this thesis, high temperature applications including gas permeability (at R.T. and up to ~700 ^oC), molten metal filtration, and heat exchanger were tested for produced PDC components.

2.4. Applications of PDC Aerogels

Aerogels are widely used in scientific and industrial research. As an example, graphene and carbon-based aerogels exist both as anodes and cathodes for lithium-ion,[250–252] lithium-sulfur,[253–255] and sodium-ion[256,257] batteries. Although PDC aerogels are a new class of materials, they have widespread applications due to their properties. For instance, SiOC structures have disordered free carbons and that makes them

potential candidates for electrochemical applications.[258,259] As a result, SiOC aerogel was studied first as an anode material for Li-ion batteries. In the mentioned study,[187] it was shown that SiOC aerogel, pyrolyzed at 1000 ^{o}C under an Ar atmosphere, demonstrated a reversible capacity as high as 650 mAh/g at a charging rate of C (360 mA/g). In another study,[192] the effect of a solvent (acetone vs. cyclohexane) and inert atmosphere (Ar vs. Ar/H_2) on electrochemical properties of SiOC aerogel was investigated. It was found that SiOC aerogel obtained from cyclohexane provided improved cycling stability with low capacity. Additionally, pyrolyzing in Ar/H_2 atmosphere provided a high reversible capacity of 200 mAh/g at a high charging/discharging rate of 20C (7200 mA/g).

PDC aerogels are used for the adsorption of organic dyes [e.g., Methylene Blue (MB)/Rhodamine B (RB)], metal ions [Cr(III)/(VI)], and gases (e.g., CO, H_2, NO_2, and CO_2), among other application.[168,175,194,195,197] In a particular study,[194] adsorbent behavior of MB and RB between aerogels and foams were compared. It was demonstrated that SiC&SiOC aerogels provided a higher adsorption capacity than that of SiC foam since aerogels showed an SSA reaching around 163 m^2/g while foam provided an SSA of ~0.3 m^2/g. Zera et. al[195] studied SiOC and SiCN aerogels which were produced by supercritical/atmosphere drying with pyrolysis in an inert (N_2)/reactive (NH_3/CO_2) atmosphere. The authors showed the effect of the drying process with the pyrolyzed atmosphere on the adsorption capacities of metal ions (Cr(III)/(VI)). SiOC aerogel pyrolyzed under the N_2 and SiCN pyrolyzed under the NH_3 atmosphere both provided adsorption capacities as high as 30 and 20 mg/g after 1h for Cr(VI). SiCN did not provide any adsorption capacity, while SiOC aerogel showed low adsorption for Cr (III). In a recent and interesting study,[175] adsorption capacities of harmful compounds in cigarette smoke for micro/mesopores SiOCN aerogel having an SSA of up to 827 m^2/g were studied. The lowest and highest removal efficiencies were found as -8 % and 75.9 % for phenol and crotonaldehyde.

Sol-gel synthesized SiOC aerogels having an SSA of 198 m^2/g showed thermal conductivity of 0.027 $W \cdot m^{-1} \cdot K^{-1}$ (at R.T.).[172] Obtained SiOC provided thermal stability at 1200 ^{o}C in the air with a weight loss of 1.65 wt%. In other research,[173] sol-gel synthesized BN/SiOC (boron nitride/silicon oxycarbide) aerogels having an SSA of 142-566 m^2/g demonstrated thermal conductivity of 0.04-0.20 $W \cdot m^{-1} \cdot K^{-1}$ (at R.T.) depending on the BN contents from 0 to 15 vol%. Figure 2.20 (a) shows the increase in thermal conductivity as the temperature increases from R.T. up to 1300 °C. High

temperature thermal conductivity of sol-gel synthesized SiBCO aerogel was measured as 0.1380 $W \cdot m^{-1} \cdot K^{-1}$ under vacuum at 1500 °C.[174] Similarly, the thermal conductivity of polymer derived SiC nanowire aerogels were reported as 0.03-0.23 $W \cdot m^{-1} \cdot K^{-1}$ under He at R.T. to 900 °C.[260]

PDC aerogels have also been evaluated as gas and optic sensors. For instance, sol-gel synthesized SiOC aerogels were studied for CO, H_2, and NO_2 sensing behavior at different temperatures (300-550 °C).[168] It was shown that the SiOC aerogel having an SSA of 150 m^2/g showed the highest response to 5 ppm NO_2 at 300 °C, as shown in Figure 2.20 (b). The first transparent sol-gel synthesized SiOC aerogels (SSA of 171-615 m^2/g) pyrolyzed under a pure H_2 atmosphere at 800-1100 °C are possible candidates to be used as optical sensors for different gases.[169]

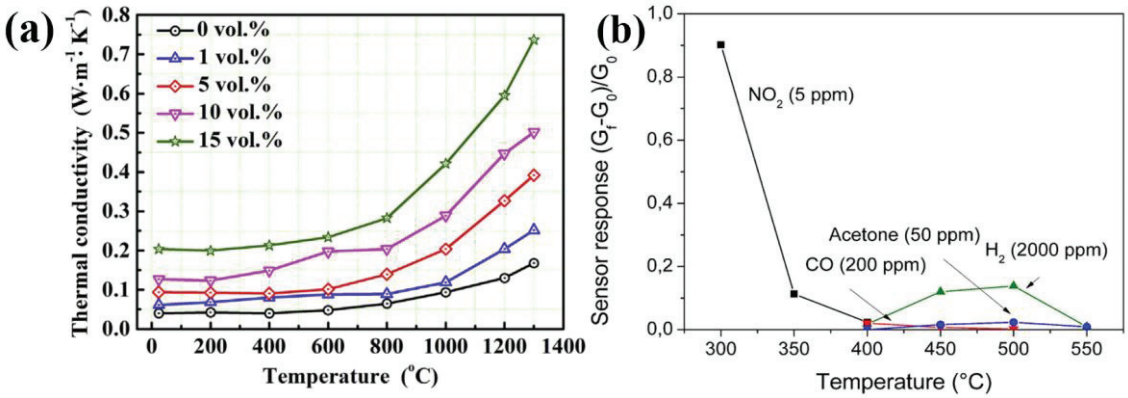

Figure 2.20. (a) Thermal conductivity vs. temperature of BN/SiOC aerogel with different BN contents from 0 to 15 vol%. (Source: Yang, H et al., 2020),[173] and (b) gas sensing behavior of SiOC aerogels from 300 to 550 °C. (Source: Karakuscu, A et al., 2013)[168]

CHAPTER 3

EXPERIMENTAL PROCEDURE

Published in part in: Semerci, T., de Mello Innocentini, M. D., Marsola, G. A., Lasso, P. R. O., Soraru, G. D., Vakifahmetoglu, C. "Hot air permeable preceramic polymer derived reticulated ceramic foams". ACS Applied Polymer Materials, 2(9), 4118-4126, (2020).

Published in part in: Semerci, T., Dizdar K.C., Kulkarni A., Dispinar D., Soraru G.D., Vakifahmetoglu C. "Polymer-derived ceramic molten metal filters". Journal of Materials Science, in press, (2022).

3.1. Materials

Polymer derived SiOC foams were produced using a mixture of commercially available polysiloxanes and four types of PU foams. Linear polyhydridomethylsiloxane (PHMS, MW ~2100−2400, 30-45 cSt, CAS: 63148-57-2, Gelest Inc., Morrisville, PA, USA) bearing Si-H moieties, a cyclic 2,4,6,8-tetramethyl-2,4,6,8-tetravinylcyclotetrasiloxane (TMTVS 97%, CAS: 2554-06-5, Alfa Aesar, Ward Hill, MA, USA) with Si-C=C reactive groups, and vinyl-terminated polydimethylsiloxane (PDMS, MW ~62,700, 10,000 cSt, CAS: 68083-19-2, Gelest Inc., Morrisville, PA, USA) were used as a precursor and crosslinking agents. As a catalyst, platinum-divinyltetramethyldisiloxane complex in xylene (2.1-2.4%Pt) (CAS: 68478-92-2, abcr GmbH, Kalsruhe, Germany) was diluted to 0.05% of Pt in the xylene and used for the hydrosilylation reaction between Si-H and C=C moieties of the crosslinker.[53] Additionally, acetone (CAS: 67-64-1, 99.5% extra pure), as impregnating solvent, was used to ease the process and it was shown that no structural change was observed in the PU bonds'.[13] As templates, four different types of PU foams were used (see Table 3.1):

three with open cells (10 ppi with bulk density 0.027 ± 0.002 g/cm^3, 65 ppi with bulk density 0.029 ± 0.001 g/cm^3, and 80 ppi with bulk density 0.030 ± 0.002 g/cm^3) and one with partially closed cells (59 ppi, bulk density 0.057 ± 0.002 g/cm^3, ARE S.r.l., Milan, Italy). The term porosity in foams is measured in ppi and refers to the number of pores in one linear inch.

SiOC(N) cellular structures and foams were obtained using a polysilazane (Durazane 1800, CAS: 503590-70-3, Merck, Darmstadt, Germany), Pt divinyltetramethyldisiloxane complex ~Pt 2% in xylene (CAS: 68478-92-2, Sigma-Aldrich, St. Louis, MO, USA) which was diluted to 0.1% as a catalyst and acetone (CAS: 67-64-1, >99% pure, Sigma-Aldrich). Commercially available thermoplastic polyurethane (TPU, 85A filament Ninjaflex, NinjaTech, PA, USA) and 10 ppi PU foam (bulk density 0.027 ± 0.002 g/cm^3, ARE S.r.l., Milan, Italy) were used for SiOC(N) cellular structures and foams.

Table 3.1. Porosities and bulk densities of PU templates.

Cell Structure	Porosity	Bulk Density (g/cm^3)
Open cell	10 ppi	0.027 ± 0.002
	65 ppi	0.029 ± 0.001
	80 ppi	0.030 ± 0.002
Partially closed cell	59 ppi	0.057 ± 0.002

SiOC aerogels were produced by using commercially available siloxane resin (Polymethylsilsesquioxane, PMS, Silres MK, Wacker-Chemie GmbH, Germany), acetone (CAS: 67-64-1, 99.5% extra pure), and tin(II) 2-ethylhexanoate (Tin, Sigma-Aldrich, CAS: 301-10-0, USA) was diluted to 15 vol% of Tin in the xylene as a catalyst.

3.2. Equipments and Characterization Techniques

The equipment used during the sample production is as follows: a magnetic stirrer (Weightlab, WN-H550) was used for the mixing of a preceramic polymer

solution. A convection oven (Memmert, UN55, France) was used for the crosslinking process. Alumina tube furnaces (Protherm PTF 16/75/450, Ankara, Turkey & Lindberg/Blue, USA) were used for heat treatment. An Lulzbot TAZ 6 open-source 3D printer (Fargo Additive Manufacturing Equipment 3D, LLC, USA) with 0.15 mm nozzles was used to print TPU filament. The solvothermal process was carried out in a stainless-steel static autoclave (Parr Instruments, Model 4748 acid digestion vessel, USA) with a PTFE Teflon cup.

Characterization techniques are explained in detail in the following subsections.

3.2.1. Structural Characterizations

The structural features of PU, TPU, and PDC components were analyzed by Fourier Transform Infrared Spectroscopy with attenuated total reflectance (FTIR-ATR, Spectrum Two with UATR fitted, Perkin Elmer, USA), wavenumber from 450 cm^{-1} to 4000 cm^{-1}, and 20 scans for each sample with 4 cm^{-1} resolution.

X-ray diffraction (XRD, Philips X'Pert Pro) with CuKα radiation, a step counting time of 3 s, and a scan of 0.05°, between 20° and 80° (2Θ) was carried out to analyze the structural nature of foams and cellular structures. FTIR and XRD data were plotted after normalization.

The thermal behavior of PU templates (10-80 ppi foam) and as-received preceramic polymers (PHMS, TMTVS, and PDMS) was studied by thermal gravimetric analysis (TGA) using equipment (Perkin Elmer Diamond TG/DTA, USA) with a heating rate of 5 ^{o}C/min, in the flow of N_2 up to 1000 ^{o}C. The pyrolytic process of PHMS/TMTVS crosslinked for 24 h at 60 °C was determined with a heating rate of 10 ^{o}C/min, in the flow of Ar up to 1000 ^{o}C. The thermal behavior of TPU was measured with equipment (Netzsch STA 409, Netzsch Gmbh, Selb, Germany) at 10 °C/min up to 1200 °C in air.

3.2.2. Morphological Characterizations

The microstructural features of the foam and cellular structures (fracture surfaces), tensile samples produced by using a filter or no filter, and aerogels were analyzed by a scanning electron microscope (SEM, FEI Quanta 250 FEG, Hillsboro, OR, USA) after surface coating with ~10 nm Au (Emitech K550X sputter coater, Quorum Technologies, UK). SEM images were subsequently analyzed using the ImageJ software (ImageJ 1.52a, National Institutes of Health, USA) to determine the effective cell, pore, and strut sizes of the samples. At least 100 measurements of each sample were analyzed and converted to 3D data by using the stereological equation: $D_{sphere} = D_{circle}/0.785$.[261]

A High-resolution X-ray micro-Computed Tomography (CT) system (SkyScan, model 1172, Aartselaar, Belgium) was used to determine the morphological parameters of SiOC foams. For each cylindrical sample, about 320 radial slice images (pixel size of 13.5 μm) were reconstructed to 8-bit BMP files (2000 × 2000 pixels) and analyzed as 3D images using the Brucker SkyScan software package (CTVOX, CTAN, CTVOL, and Dataviewer).

N_2 sorption tests were done by Gemini V (Micromeritics, Norcross, GA, USA). The ceramic samples were degassed at 200 ^oC for 12 h before analysis. SSA was obtained using the BET (Brunauer-Emmett-Teller) equation.[262] The pore size distribution was determined using the Barrett-Joyner-Halenda (BJH) method.[263]

The bulk densities of the SiOC aerogels and cast samples were measured according to Archimedes' principle by using DI water as a buoyant medium. The skeletal density (ρs) of powdered ceramic samples was determined by a helium pycnometer (AccuPyc 1330, Micromeritics, Norcross, GA, USA). The bulk density and total porosity (vol%) of the ceramic components were determined by relating their size and mass measurements, and total porosity (ε) was then calculated using both density values.

3.2.3. Mechanical Characterizations

The compression tests of PDC foams and AM cellular structures were acquired using a TA.XT plus Texture Analyzer (Stable Micro System Ltd., Godalming, Surrey, UK) and Instron 5969 testing machine, respectively. Each data set was obtained from 10 samples. SiOC(N) and SiOC foams having 10 ppi and AM-made SiOC(N) cellular structures were measured with a cubic shape (~10 x 10 x 10 mm^3) and a crosshead speed of 1 mm/min. Moreover, 59, 65, and 80 ppi SiOC foams were analyzed with a cubic shape (~5 x 5 x 5 mm^3) and a crosshead speed of 0.5 mm/s, and the measurements were continued until the occurrence of the first collapse. Following the casting, solidified alloys were prepared for tensile tests, carried out in Zwick Roell 8596.

3.3. Production of Porous PDC Components

In the following subsections, the production methods of porous PDC components will be explained separately.

3.3.1. Production of PDC Foams by Using Replica Technique

SiOC foams were produced by using the replica technique. Three different preceramic polymer blends were prepared from PU/PHMS/PDMS/TMTVS (in weight ratio): (i) 1/2/0/0.08, (ii) 1/1.7/0.3/0.08, and (iii) 1/1/1/0.08. The samples with PDMS were formed since it is known that such a polymer can be used to enhance the SSA of the components by creating hierarchical porosity.[264] First, preceramic polymers (PHMS, PDMS, and TMTVS) were dissolved in acetone while stirring at 250 rpm R.T. for 3 min. After homogenization, the Pt catalyst was added dropwise, and the mixture was stirred for 1 min at 200 rpm at R.T. Considering the ~22% linear shrinkage that occurred during the pyrolysis, the PU foams were cut to the desired sizes. The prepared

blends were then transferred into separate Petri dishes where PU foams were soaked and squeezed several times to remove the excess mixtures. This process was followed until all of the preceramic solutions were impregnated. The curing procedure was conducted under two different conditions to alter the final strut structure: (i) to yield dense struts: 80 °C for 7 h followed by R.T. curing for 23 h, and (ii) to yield hollow struts: 220 °C for 2 h. All the cured foams were pyrolyzed under Argon (Ar) flow (200 mL/min) with a heating rate of 2 °C/min to 1000 °C and 2 h (dwell time) in an alumina tube furnace.

Produced SiOC foams were categorized according to the cell density of the PU foam type (10, 59, 65, 80 ppi), strut structure (dense/hollow struts), and PDMS weight ratio. The experimental parameters for the production of SiOC foams are given in Table 3.2.

Table 3.2. Experimental parameters for SiOC foams production.

Sample Code*	**PU Foam Type**	**PU/PHMS/ PDMS/TMTVS (in weight ratio)**	**Curing Condition**	**Pyrolysis Temperature (°C) / Atmosphere / Time (h)**
C1-D	10 ppi (open porosity)	1/2/0/0.08	80°C/7h + R.T./23h	1000 / Ar / 2
C2-D	59 ppi (partial closed porosity)	1/2/0/0.08	80°C/7h + R.T./23h	
C2-H			220°C/2h	
C2-D-15		1/1.7/0.3/0.08	80°C/7h + R.T./23h	
C2-H-15			220°C/2h	
C2-D-50		1/1/1/0.08	80°C/7h + R.T./23h	
C2-H-50			220°C/2h	
C3-D	65 ppi (open porosity)	1/2/0/0.08	80°C/7h + R.T./23h	
C3-H			220°C/2h	
C3-D-15		1/1.7/0.3/0.08	80°C/7h + R.T./23h	
C3-H-15			220°C/2h	
C3-D-50		1/1/1/0.08	80°C/7h + R.T./23h	
C3-H-50			220°C/2h	

(cont. on next page)

Table 3.2 (cont.)

C4-D	80 ppi (open porosity)	1/2/0/0.08	80°C/7h + R.T./23h	1000 / Ar / 2
C4-H			220°C/2h	
C4-D-15		1/1.7/0.3/0.08	80°C/7h + R.T./23h	
C4-H-15			220°C/2h	
C4-D-50		1/1/1/0.08	80°C/7h + R.T./23h	
C4-H-50			220°C/2h	

*The representative sample code will be as follows; C: Ceramic, D: Dense strut.

SiOC(N) foams were produced by using a replica technique following a previously published method.[110] The preceramic polymer solution was prepared by mixing Durazane, acetone, and the Pt catalyst (100 μL of 0.1% Pt solution per 1 g of polymer precursor) while using a Durazane/PU ratio of 2. The volume of acetone was set equal to 1/5 of the volume of the PU foam. Considering the ~25% linear shrinkage that occurred during the pyrolysis, the PU foams were cut in the desired sizes. The impregnated PU foams were dried at R.T. for 24 h and pyrolyzed under N_2 flow (300 mL/min) with a heating rate of 5 °C/min to 1200 °C and 2 h (dwell time) followed by free cooling to R.T. in a tubular alumina furnace. The furnace was purged for 5 h with N_2 before pyrolysis to remove traces of oxygen and moisture. Pyrolysis temperatures and atmospheres (N_2 or Ar) affect the final ceramic composition derived from polysilazane. Nitrogen can be retained in the final ceramic structure by pyrolysis under an N_2 atmosphere. It was shown that pyrolysis under an N_2 atmosphere increases thermal stability with the formation of the Si_3N_4 crystalline phase, while an Ar atmosphere provides the final ceramic containing the SiC phase.[265] The production parameters of SiOC(N) foams are given in Table 3.3.

Commercial silicon carbide (SiC) foams with hollow struts were supplied by Foseco International Ltd.

Table 3.3. Experimental parameters for SiOC(N) foams production.

Sample Code*	PU Foam Type	PU/Durazane (in weight ratio)	Curing Condition	Pyrolysis Temperature (°C) / Atmosphere / Time (h)
C5-D	10 ppi (open porosity)	1/2	R.T. / 24h	1200 / N_2 / 2

*The representative sample codes will be as follows; C: Ceramic, D: Dense.

3.3.2 Production of PDC Cellular Structures by Using AM

AM-made SiOC(N) cellular structures were produced according to a previous study.[132] The structures were 3D printed with TPU filament using Fused Filament Fabrication (FFF). The TPU samples were 3D printed as cylindrical shapes with the dimensions of 67 mm in diameter and 13.5 mm in thickness to get the final dimensions of 50 mm in diameter and 10 mm in thickness, considering 25% linear shrinkage. Printed TPU samples were then impregnated with a Durazane solution of 5 g acetone and 500 µL of catalyst. After 15 min, 5 g of the preceramic polymer was added and kept for 4 h, changing the sides of the sample after 2 h. Drying was performed at R.T. in the air for 24 h. Crosslinking of the impregnated TPU samples was carried out at 160 °C for 3 h in airflow (400 cc/min) in a tubular furnace and then free cooling to R.T. The furnace was purged for 2 h with N_2 flow (400 cc/min) and following pyrolysis to 1200 °C with 1 h dwelling at the maximum temperature. The samples were then cooled to R.T. at 10 °C/min.

AM-made SiOC(N) cellular structures were made with two different cell sizes: the smaller cell size of 578.1 ± 14.7 µm (referred to as C6-D), and the larger cell size of 1040.8 ± 66.9 µm (referred to as C7-D).

3.4. Production of SiOC Aerogels

SiOC aerogels were obtained as follows: PMS was dissolved in acetone while stirring at 500 rpm at R.T. for 20 min. Subsequently, Tin catalyst (500 µl for 1 g of PMS) was added dropwise, and the mixture was stirred for 500 rpm at R.T. 10 min. The prepared mixture was transferred into a PTFE-lined autoclave and curing was carried out at 200 ^{o}C for 6 h. After the completion of the curing process, the autoclave was cooled down to R.T. The wet gels were removed from the autoclave and transferred into separate beakers either with fresh solvent (acetone, ethanol, n-hexane) or without solvent followed by drying at ambient pressure and temperature. After drying (~15 days), obtained polymeric aerogels were pyrolyzed under Ar flow (200 mL/min) with a heating rate of 2 °C/min to 1000 °C and 2 h (dwell time) in an alumina tube furnace to obtain SiOC aerogel.

Synthesis parameters were adjusted to have 60 and 80 vol% of the solvent (acetone) amount in the mixture and 35 and 65 vol% of autoclave filling. Exceeding reaction vessel pressure presents a risk of explosion in the autoclave; therefore, great caution was taken when determining autoclave filling volume. The details of experimental parameters for SiOC aerogels production are given in Table 3.4.

Table 3.4. Production parameters of SiOC aerogels.

Sample Code*	Solvent Amount (vol%)	Autoclave Filling (vol%)	Curing Condition	Pyrolysis Temperature (^{o}C) / Atmosphere / Time (h)
A1-SF	60	35	200 °C / 6h	1000 / Ar / 2
A1-Ace				
A1-EtOH				
A1-Nhex				
A2-SF	60	65		
A2-Ace				
A2-EtOH				
A2-Nhex				

(cont. on next page)

Table 3.4 (cont.)

A3-SF	80	35	200 °C / 6h	1000 / Ar / 2
A3-Ace				
A3-EtOH				
A3-Nhex				
A4-SF	80	65		
A4-Ace				
A4-EtOH				
A4-Nhex				

*The representative sample codes will be as follows; A: Aerogel, SF: Solvent-free, Ace: Acetone, EtOH: Ethanol, Nhex: n-hexane.

3.5. Permeability Measurements

Permeability parameters of produced ceramic foams were received from experimental data and fitting of Forchheimer's equation (see Eqn. 3.1):[266–268]

$$\frac{\Delta P}{L} = \frac{\mu}{k_1} \upsilon_s + \frac{\rho}{k_2} \upsilon_s^2 \quad (3.1)$$

where:

ΔP is the pressure drop,

υ_s is the superficial/face velocity of a fluid through the medium,

L is the medium length/thickness along the flow direction,

μ is the viscosity of the fluid,

ρ is the density of the fluid,

k_1 is the Darcian permeability coefficient,

k_2 is the non-Darcian permeability coefficient.

(Coefficients are according to Darcy's law)

Both permeability coefficients are considered based on the cell properties including cell morphology, size, and interconnectivity. These coefficients are used to estimate the $\Delta P \times v_s$ part for other fluids or flow conditions; provided that the actual viscosity and density of the fluid are corrected in Eqn. 3.1. k_1 and k_2 can be altered with temperature because of the reversible and irreversible changes in the porous microstructure.[266,268–270] For the compressible flow of gases or vapors, ΔP is calculated as (see Eqn. 3.2):

$$\Delta P = \frac{P_i^2 - P_0^2}{2P} \tag{3.2}$$

where:

P_i is the absolute fluid pressure at the entrance of the medium,

P_o is the absolute fluid pressures at the exit of the medium,

P is the pressure for which v_s, μ, and ρ are measured or calculated. ($P = P_o = P_{atm} = 94.9$ kPa)

To evaluate the representativeness of the resulting k_1 and k_2, Forchheimer's number (Fo) is used (see Eqn. 3.3):[267,268]

$$F_o = \frac{\rho \upsilon_s}{\mu}\left(\frac{k_1}{k_2}\right) \tag{3.3}$$

While Forchheimer's number is about the linearity in the pressure drop, Reynolds number (Re) is about the laminarity of flow in channels.[268] Combining Eqns. 3.1 and 3.3 yields:

$$\frac{\Delta P}{L} = \frac{\mu}{k_1}\upsilon_s(1 + F_o) \tag{3.4}$$

Comparing Eqns. 3.1 and 3.4 show that when Forchheimer's number << 1, $\left(\frac{\mu v_s}{k_1}\right)$ is related to estimate the $\left(\frac{\Delta P}{L}\right)$ as specified in Darcy's law. When Forchheimer's number >> 1, $\left(\frac{\Delta P}{L}\right)$ is estimated via $\left(\frac{\mu v_s^2}{k_2}\right)$. On the other hand, the whole Forchheimer's equation must be used to reliably use $\left(\frac{\Delta P}{L}\right)$ at any intermediate flow condition. The contributions of the terms viscous and inertia to the total pressure drop can be stated as (see Eqns. 3.5 and 3.6):[268]

$$Viscous\ (\%) = 100\left(\frac{1}{1+F_o}\right) \tag{3.5}$$

$$Inertial\ (\%) = 100\left(\frac{F_o}{1+F_o}\right) \tag{3.6}$$

The air permeability test of SiOC foams (two samples of each composition) was carried out in a steady-state regime with dry airflow at R.T. (T_o = 25-29 °C, $P_o = P_{atm}$ ~ 94.9 kPa) using a laboratory-made apparatus. The samples were produced cylindrical in shape with a diameter of 48.1±2.0 mm and a thickness of 4.6±0.2 mm for the permeability test. The obtained disk samples were placed sidewards in a cylindrical chamber providing a 5.36 cm^2 circular flow area for a 2.61 cm flow diameter. The pressure drop across the sample (P_i-P_o) is measured with a digital micromanometer (0-1000 Pa, Dwyer Mark III, series 475, Michigan, USA). The volumetric air flow rate (Q) is controlled by a needle valve and measured with rotameters (0-400 and 300-3000 L/h, Conaut, São Paulo, Brazil). The flow rate (Q) is obtained from $v_s = \left(\frac{Q_o}{A_{flow}}\right)$, where Q_o denotes the flow rate at the sample exit. P_i, P_o, and v_s values are obtained from at least 10 sets in a stationary gas flow regime. The obtained data were fitted using a least-square regression method with respect to the parabolic model of the type: $y = ax + bx^2$. In this model, x and y symbolize the fluid velocity (v_s) and the left side of Eqn. 3.1. Furthermore, Darcian and non-Darcian permeability coefficients are calculated by the fitted constants as $a(k_1 = \frac{\mu}{a})$ and $b(k_2 = \frac{\rho}{b})$.

The average fluid dynamic pore size (d_{pore}) for each sample was determined by the Ergun-related formula which is given in Eqn. 3.7:[268,269]

$$d_{pore} = \left(\frac{150k_1}{2.25\varepsilon}\right)^{0.5} \tag{3.7}$$

where:

ε is the open porosity,

k_1 is the Darcian permeability coefficient.

SiOC foams were measured at three different temperatures: ~25 °C, ~350 °C, and ~700 °C by using a laboratory-made hot gas permeameter (see Figure 3.1) for hot air permeability evaluation. The disk samples were tightly placed in a 310 stainless steel cylindrical sample holder with a diameter of 14 mm (circular flow area A_{flow} = 154 mm^2). Moreover, special heat-resistant O-rings were used to prevent leakage. The sample holder was placed in an electric furnace (7500 W) which was controlled via a proportional-integral-derivative (PID) control scheme to perform different temperature-time programs. Dry air supplied by an air compressor was preheated in a 2 m long 316 stainless-steel (SS-316) serpentine within the furnace chamber before reaching the sample. K-type thermocouples placed perpendicularly to the sample at the entrance and exit chambers were used to measure the temperature. Additionally, these were used near the pressure transducers to monitor the gas temperature before it entered the rotameter. The temperature was managed by the PID controller, and air flow was supplied upwards from the sample with a constant pressure of P_i.

Evaluation of the permeability coefficients was calculated by changing the air properties with temperature. The density (ρ) and viscosity (μ) of air were calculated following Eqns. 3.8 and 3.9:[268]

$$\rho = \frac{P_o MM_{air}}{RT_o} \tag{3.8}$$

$$\mu = 1.73x10^{-5} \left(\frac{T_o}{273}\right)^{1.5} \left(\frac{398}{T_o+125}\right) \quad (3.9)$$

where:

P_o is the pressure at the exit stream,

T_o is the temperature at the exit stream,

MM_{air} is the average molar mass of dry air (28.965×10^{-3} kg·mol^{-1}),

R is the ideal gas constant (8.314 Pa·m^3·mol^{-1}·K^{-1}).

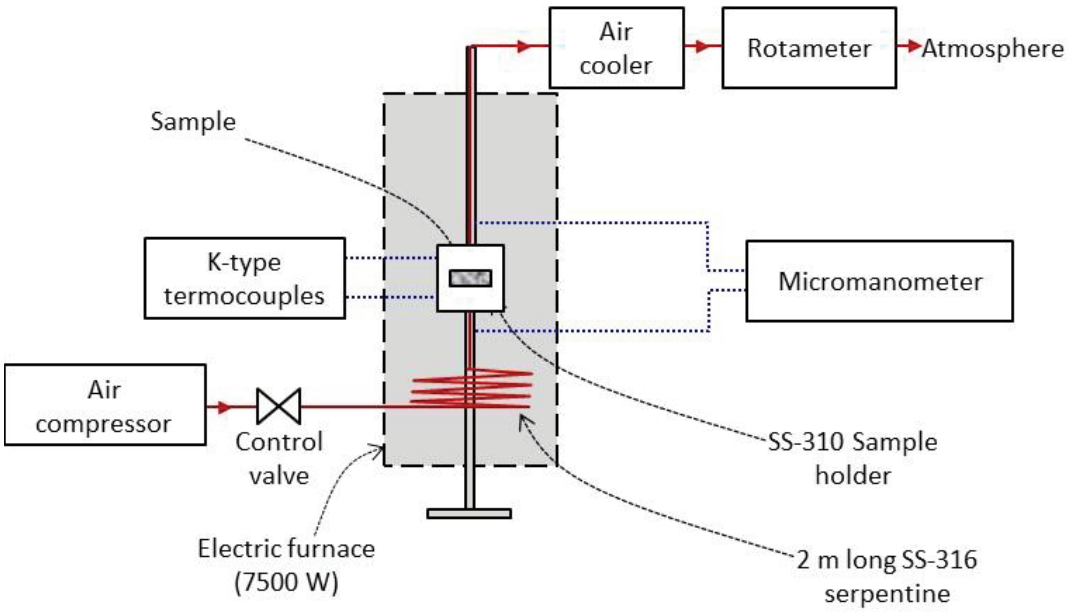

Figure 3.1. Schematic representation of the hot gas permeameter for the room and high-temperature tests. (Source: Semerci, T. et al., 2020)[13]

3.6. Casting Tests

Casting trials were done using a sand mold, with the details given in Figure 3.2. Ten cylindrical bars were produced with 8.5 mm diameters and 150 mm lengths. For

casting, A357 alloy was used, with the chemical composition given in Table 3.5. The thickness of all filters was specified between ~1 mm and ~1.5 mm.

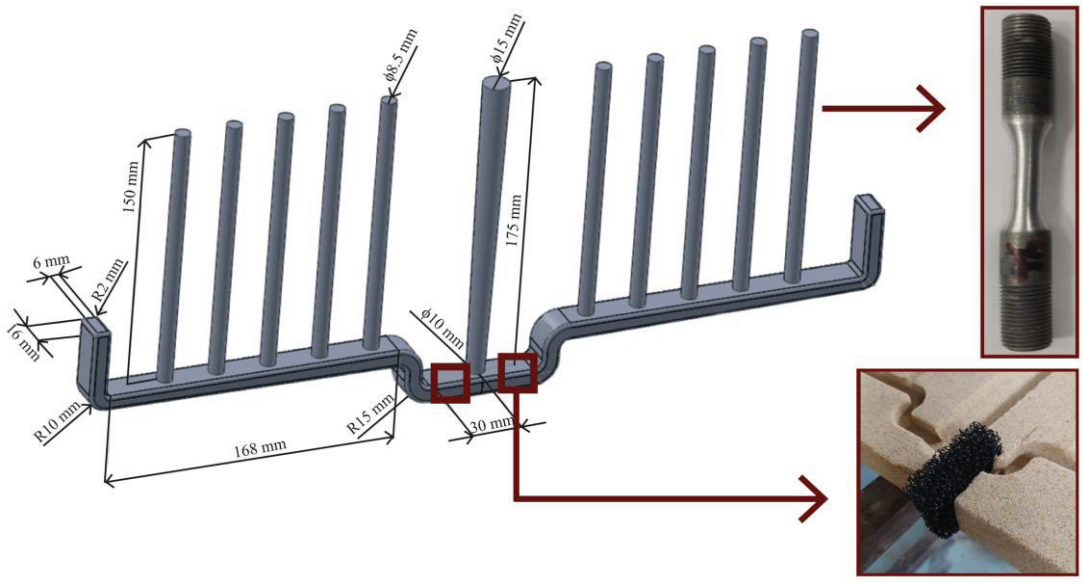

Figure 3.2. SolidWorks drawing of casting system with photographic images of real test place of ceramic filter (bottom right) and aluminum alloy bar after casting for the mechanical test (top right). (Source: Semerci, T. et al., 2022)[271]

Table 3.5. Chemical composition (wt%) of the A357 alloy.

Si	Fe	Cu	Mn	Mg	Ti	Al
7.485	0.173	0.021	0.018	0.529	0.126	91.45

The process steps for obtaining molten metal are given in Figure 3.3. Preheating was applied to the ICS induction furnace by increasing the power by 5 kW every 10 min period. After completing preheating, the furnace was operated at full power (~35 kW) to reduce the melting time. The temperature was controlled from the outside with a thermocouple (placed over the induction furnace depicted in Figure 3.3) during the process. 18 kg of A357 alloy was melted in an A50 SiC crucible at 750 ºC. No degassing or melt treatment was performed to compare the yield of the filter. After the

castings were completed, the samples were heat-treated with the solutionizing at 540 ºC for 6 h. Subsequently, the obtained samples were quenched in water at R.T. followed by aging at 160 °C for 4 h and machined (see Figure 3.4) according to the ASTM E8/E8M standard.

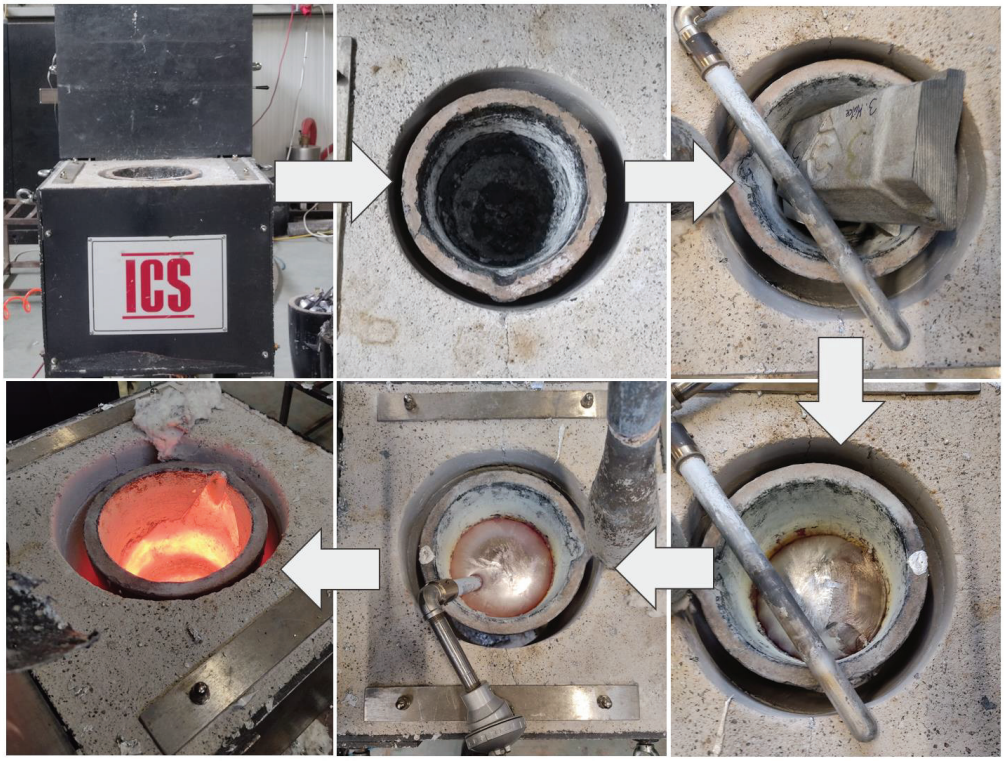

Figure 3.3. Photographic images of the melting of A357 alloy in an ICS induction furnace.

Weibull analysis was carried out and survivability tests were used to statistically compare the repeatability and reliability of the casting trials.

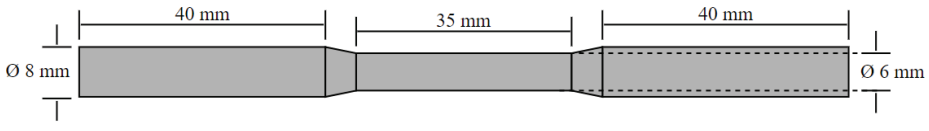

Figure 3.4. Schematic of the prepared aluminum alloy bar after casting for the mechanical test.

3.7. Heat Exchange Tests

Heat exchange between the furnace walls (TypeXTube, XERION Advanced Heating Ofentechnik GmbH, Freiberg, Germany) and air passing through the ceramic tube was conducted in a high temperature pressure drop (HTPD) apparatus (see, Figure 3.5). The alumina tube (Alumina C799, SCERAM Ceramics, Champagne au Mont d'Or, France) that was placed in the furnace was 500 mm in length and 20 mm in internal diameter (27 mm external diameter). The insulation part surrounding the ceramic tube, shown in green in Figure 3.5, consists of alumina. The heated distance area inside the tube is 100 mm and the tests were performed by placing 10 pieces of SiOC foams (approximately 100 mm) in a row. The experiments were conducted at furnace temperatures of 900 ^{o}C with three different airflow velocities (in terms of Reynolds numbers): 0.6 m/s (745), 1.2 m/s (1′ 490), and 1.8 m/s (2′235).

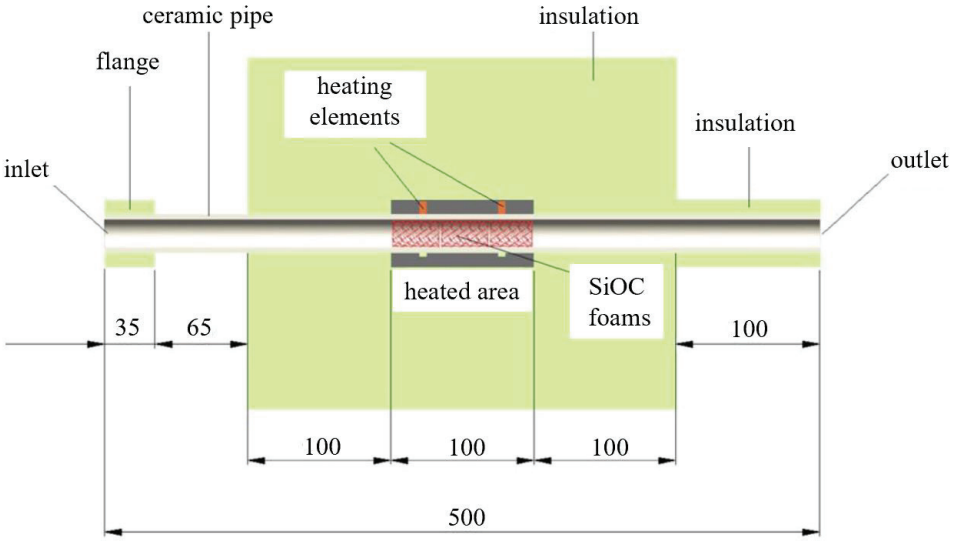

Figure 3.5. Schematic representation of the high temperature pressure drop (HTPD) apparatus developed at SUPSI. (Source: Pelanconi, M. et al., 2019)[246]

CHAPTER 4

RESULTS AND DISCUSSION

Published in part in: Semerci, T., de Mello Innocentini, M. D., Marsola, G. A., Lasso, P. R. O., Soraru, G. D., Vakifahmetoglu, C. "Hot air permeable preceramic polymer derived reticulated ceramic foams". ACS Applied Polymer Materials, 2(9), 4118-4126, (2020).

Published in part in: Semerci, T., Dizdar K.C., Kulkarni A., Dispinar D., Soraru G.D., Vakifahmetoglu C. "Polymer-derived ceramic molten metal filters". Journal of Materials Science, in press, (2022).

4.1. PDC Foams and Cellular Structures

In brief, the structural properties of PU templates, preceramic polymers, and produced PDC components, followed by morphological and mechanical properties of PDC components, and finally, details regarding applications including gas permeability (at R.T. and up to ~700 ºC), molten metal filtration and heat exchanger will be provided in the following subsections.

4.1.1. Structural Properties

4.1.1.1. Thermal Analysis of PU Templates and Preceramic Polymers

SiOC foams have been produced by the replica technique.[13,108,111,112,272] In this technique, a template/substrate, typically a flexible PU foam is infiltrated by a solution of preceramic polymer, followed by curing and pyrolysis. In general, PU starts to decompose at ~200 ºC in an inert atmosphere and acts as a sacrificial agent.[112,113]

PU foams and TPU were used as templates to produce PDC foams and AM-made cellular structures, respectively. TGA analyses were performed to determine the thermal behaviors of templates [see Figure 4.1 (a)]. All PUs (10-80 ppi foams) showed the largest thermal decomposition between ~250 °C and 450 °C. 59 ppi PU foam demonstrated the highest weight loss (99.8 wt%), followed by 10 ppi PU (98.9 wt%), 80 ppi PU (98.3 wt%), and 65 ppi PU (94.1 wt%) at 1000 °C. Contrarily, TPU started to decompose at 300 °C and continued until 500 °C with a weight loss of 94.1 wt% (at 1200 °C). Figure 4.1 (b) shows TGA analyses of as-received PHMS, TMTVS, PDMS, and crosslinked PHMS/TMTVS at 60°C/24h. The decomposition of as-received PHMS started at ~150 °C and completed at ~ 450 °C with a weight loss of 89.7 wt% (at 1000 °C). As-received TMTVS showed the largest thermal decomposition between ~50 °C and 150 °C. PHMS cured with a TMTVS crosslinking agent provided a ceramic yield of ~75 wt% at 1000 °C and the largest weight loss occurred between ~400 °C and 800 °C due to the organic-to-inorganic transformation. As-received PDMS remained thermally stable up to ~200 °C without loss of any weight, and pyrolytic decomposition was completed at ~ 600 °C.

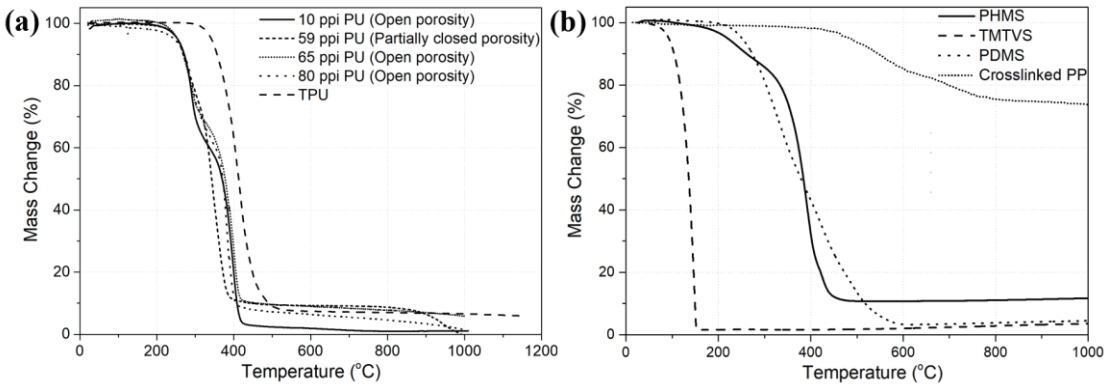

Figure 4.1. TGA data of as-received (a) PU templates (10-80 ppi foams), and TPU; (b) PHMS, TMTVS, PDMS, and crosslinked PP derived from PHMS/TMTVS.

4.1.1.2. Structural Properties of PU Templates

The FTIR spectra of PUs and TPU are given in Figure 4.2. All PUs showed the same peaks. The characteristic urethane peak of PU was observed around 3300 cm^{-1} as N-H stretching.[13,273] C-H stretching vibrations with asymmetric and symmetric vibrations of -CH_2- were seen around 2934 cm^{-1} and 2862 cm^{-1}.[274] C=O stretching and N-H band were observed around 1723 cm^{-1} and 1528 cm^{-1}.[275,276] In addition to the peaks of PU, TPU demonstrated the characteristic urethane bands ~1720 cm^{-1} and 1650 cm^{-1}, and the ester peak ~1167 cm^{-1}.[132]

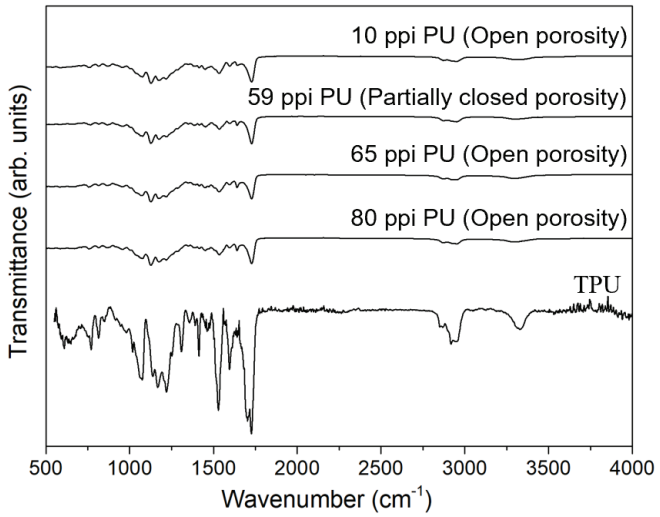

Figure 4.2. Normalized FTIR spectra of as-received PU foam templates having 10-80 ppi, and TPU.

The effects of the impregnation solvent (i.e., acetone) on the PU foams were investigated by FTIR analysis (see Figure 4.3). The results showed no structural change in PU, meaning that it is suitable to use acetone as an impregnation solvent.

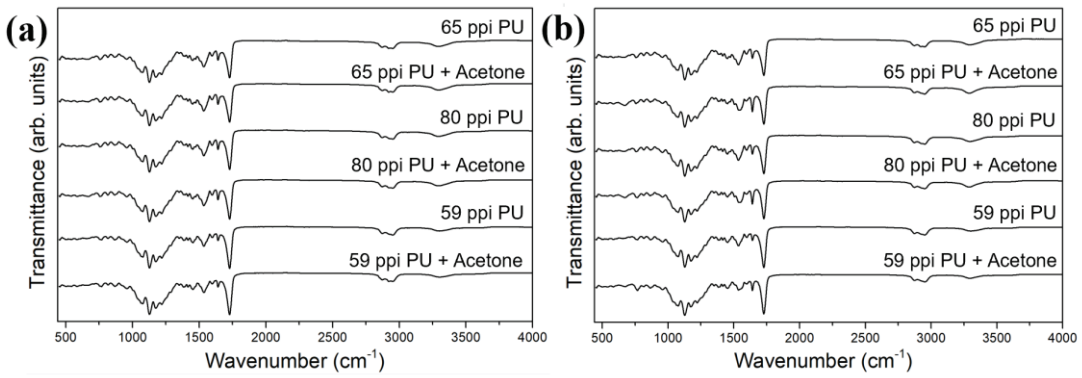

Figure 4.3. Normalized FTIR spectra of PU foams with acetone at (a) 80ºC/7h + R.T./23h, and (b) 220ºC/2h.

4.1.1.3. Structural Properties of Preceramic Polymers

Figure 4.4 shows the FTIR spectra of as-received chemicals and preceramic polymers crosslinked at 80°C/7h + R.T./23h and 220°C/2h. In the spectra of crosslinked preceramic polymers, peaks around 2165 and 900 cm^{-1} belonged to Si-H bond while peaks around 1260 and 770 cm cm^{-1} were associated with $Si-CH_3$ bond vibrations.[191] In addition, Si-O stretching bonds were observed around 1055 cm^{-1}.[191] Peaks at 3020-3057 cm^{-1} and 1408 cm^{-1} were assigned to vinyl groups in TMTVS and C-H vibrations of conjugated C atoms.[277] As depicted in Figure 4.4, the reduction of the Si-H and vinyl peak intensities imply progress through hydrosilylation reactions.[264,278,279] It is understood from the reduction of such Si-H peak and from the disappearance of the vinyl bond absorptions that the addition of TMTVS and vinyl-terminated PDMS improved the crosslinking, particularly when crosslinking was operated at a higher temperature. It is possible to state that the crosslinking was not finished for the low temperature cured samples (80°C/7h + R.T./23h).

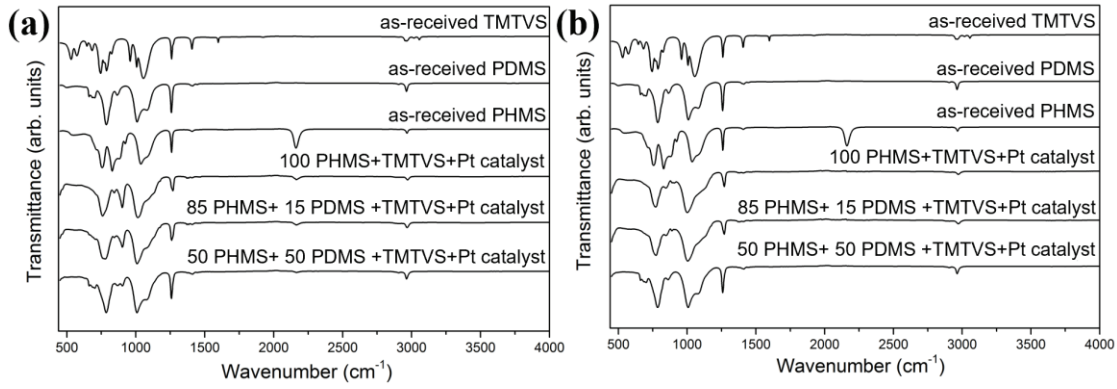

Figure 4.4. Normalized FTIR spectra of as-received PHMS, TMTVS, PDMS and preceramic polymers crosslinked at (a) 80°C/7h + R.T./23h, and (b) 220°C/2h.

4.1.1.4. Structural Properties of PDC Components

I) SiOC Foams

FTIR spectra of SiOC foams obtained from 65 and 80 ppi PU foams are given in Figure 4.5. All SiOC foams showed similar peaks: Si-O-Si deformation which belongs to the Si-O bond was around 450 cm^{-1}, and Si-C and Si-O stretching vibrations were around 800 cm^{-1}.[52,280] A broad peak around 1070 cm^{-1} is associated with the Si-O stretching in the Si-O-Si vibrations of the silicon oxycarbide network.[107,281]

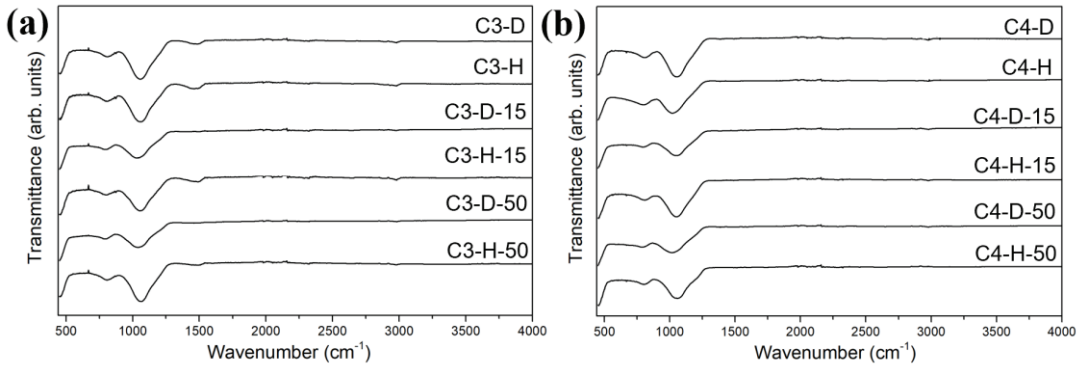

Figure 4.5. (a&b) Normalized FTIR spectra of SiOC foams with dense (D) or hollow (H) struts obtained from 65 ppi (C3) and 80 ppi (C4) PU foams. 15 and 50 represent PHMS/PDMS weight ratios of 1.7/0.3 and 1/1.

XRD patterns of SiOC foams are given in Figure 4.6. No crystalline phase was observed, but broad Bragg reflections were observed between 10° and 30° (2θ) associated with amorphous silicates.[281]

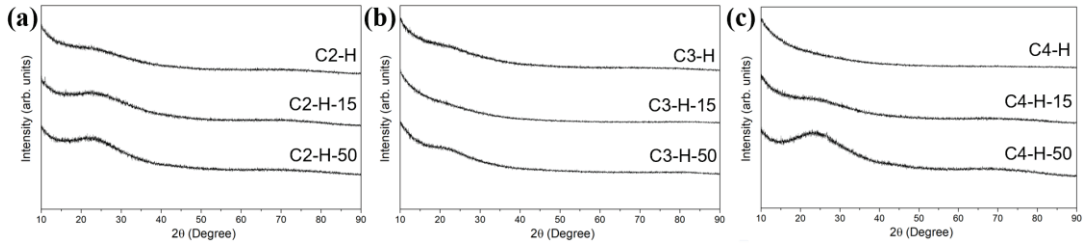

Figure 4.6. (a-c) Normalized XRD patterns of SiOC foams having hollow (H) strut obtained from 59 ppi (C2), 65 ppi (C3) and 80 ppi (C4) PU foams. PHMS/PDMS weight ratios of 1.7/0.3 and 1/1 refer to 15 and 50.

II) Foams and Cellular Structures

FTIR and XRD analyses of PDC components are given in Figure 4.7. Since SiOC(N) foam (C5-D) and AM-made cellular structures (C6-D and C7-D) were

produced using the same polymers and procedure, the rest of the data were given only for C7-D. In Figure 4.7 (a), AM-made SiOC(N) cellular structure (C7-D) showed a broad peak between 800 cm^{-1} and 1100 cm^{-1} due to the existence of Si-O, Si-C, and Si-N bonds. Peaks around 1600 cm^{-1} and 3400 cm^{-1} were associated with the presence of OH groups. In Figure 4.7 (b), the AM-made SiOC(N) cellular structure (C7-D) showed broad and smaller-broad peaks around 22.5° and 42.5° (2θ), which were related to the amorphous SiOC network and amorphous graphite. FTIR and XRD analyses results of SiOC foams (C1-D, C2-D, C3-D, and C-4) have already been given in Figures 4.5 and 4.6.

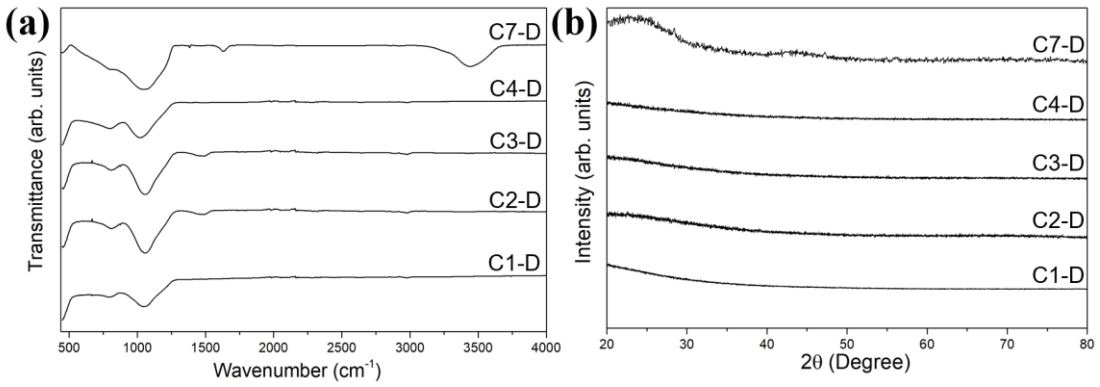

Figure 4.7. Normalized (a) FTIR spectra, and (b) XRD patterns of PDC components including dense (D) struts: SiOC foams obtained from 10 ppi (C1), 59 ppi (C2), 65 ppi (C3), and 80 ppi (C4) PU foams; and AM-made SiOC(N) cellular structure (C7-D).

4.1.2. Morphological Analyses

4.1.2.1. Microstructural Investigation of PU Templates by Using SEM

Four types of PU foams were used as templates to produce SiOC and SiOC(N) foams. Additionally, 3D printed PU templates obtained from commercially available

TPU were used to produce AM-made SiOC(N) cellular structures. Figure 4.8 shows that 10, 65, 80 ppi PU foams have reticulated structures with open cells (3D interconnected porous), while 59 ppi PU foam has a partially closed cell structure. SEM images were analyzed using the ImageJ software and pore sizes were measured as 2530.2 ± 427.4 μm (10 ppi), 498.9 ± 32.3 μm (59 ppi), 480.3 ± 23.8 μm (65 ppi), and 396.5 ± 42.5 μm (80 ppi). Pore size increased with the decrease in pore density (ppi).

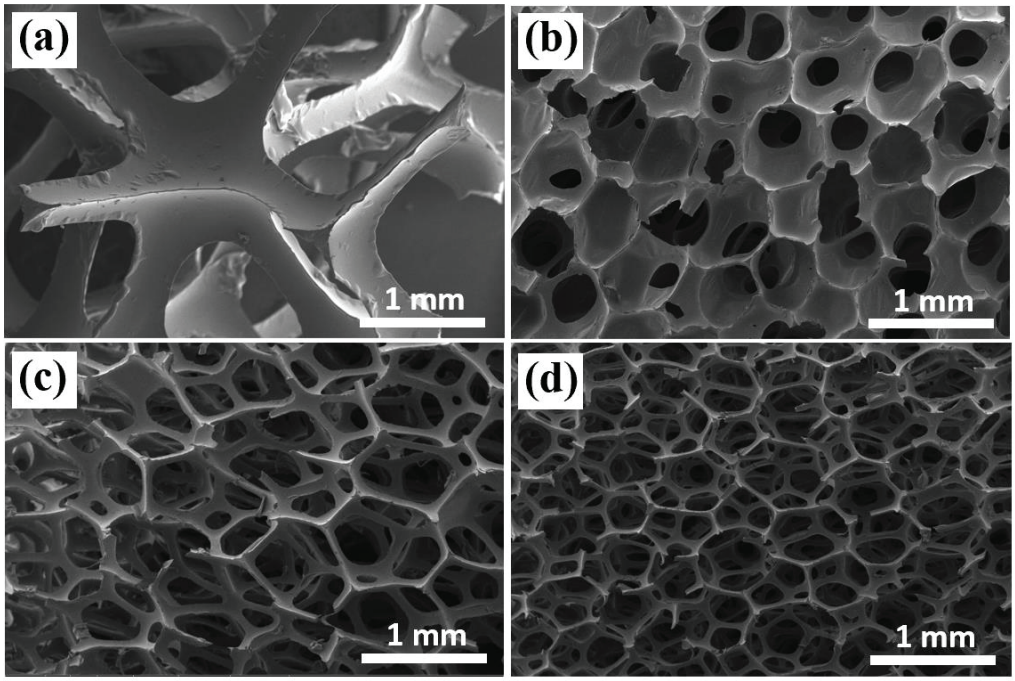

Figure 4.8. SEM images of as-received (a) 10 ppi, (b) 59 ppi, (c) 65 ppi, and (d) 80 ppi PU foam templates.

Bulk densities of PU foams were measured from mass and volume. The results were given in Table 4.1. Results show that bulk density increased with the increase in pore density.

Table 4.1. Properties of the as-received PU foam templates having 10-80 ppi.

Template Type	Cell Structure	Porosity	Pore Size (µm)	Bulk Density (g/cm^3)
PU foam	Open	10 ppi	2530.2 ± 427.4	0.027 ± 0.002
		65 ppi	480.3 ± 23.8	0.029 ± 0.001
		80 ppi	396.5 ± 42.5	0.030 ± 0.002
	Partially closed	59 ppi	498.9 ± 32.3	0.057 ± 0.002

4.1.2.2. Microstructural Investigation of PDC Components by Using SEM

SEM images obtained from the fracture surfaces of SiOC foams processed with 100% PHMS are given in Figure 4.9. The PU foams of 65 ppi and 80 ppi have open cell structures while the 59 ppi PU foam has a partially closed cell structure, resulting in the ceramic replicas shown in Figure 4.9 (a, d and g).

It was demonstrated that microstructural features of SiOC foams could be deliberately tuned to obtain "dense" or "hollow" struts. Figure 4.9 (c, f, and i) shows SiOC foams with dense struts while Figure 4.9 (b, e, and h) shows the hollow struts. The final strut morphology was impacted by the crosslinking conditions, specifically, 80°C/7h+R.T./23h and 220°C/2h. SiOC foams obtained by curing at 220°C/2h had hollow struts since the preceramic polymer blend had insufficient time to swell into the PU foam. The PU surface was coated like a film due to the sudden curing and the core became hollow after the thermal treatment and decomposition of the coated PU foam. SiOC foams obtained from the curing at 80°C/7h+R.T./23h had nearly homogenous dense struts since the solution had enough time to penetrate the PU foam matrix.

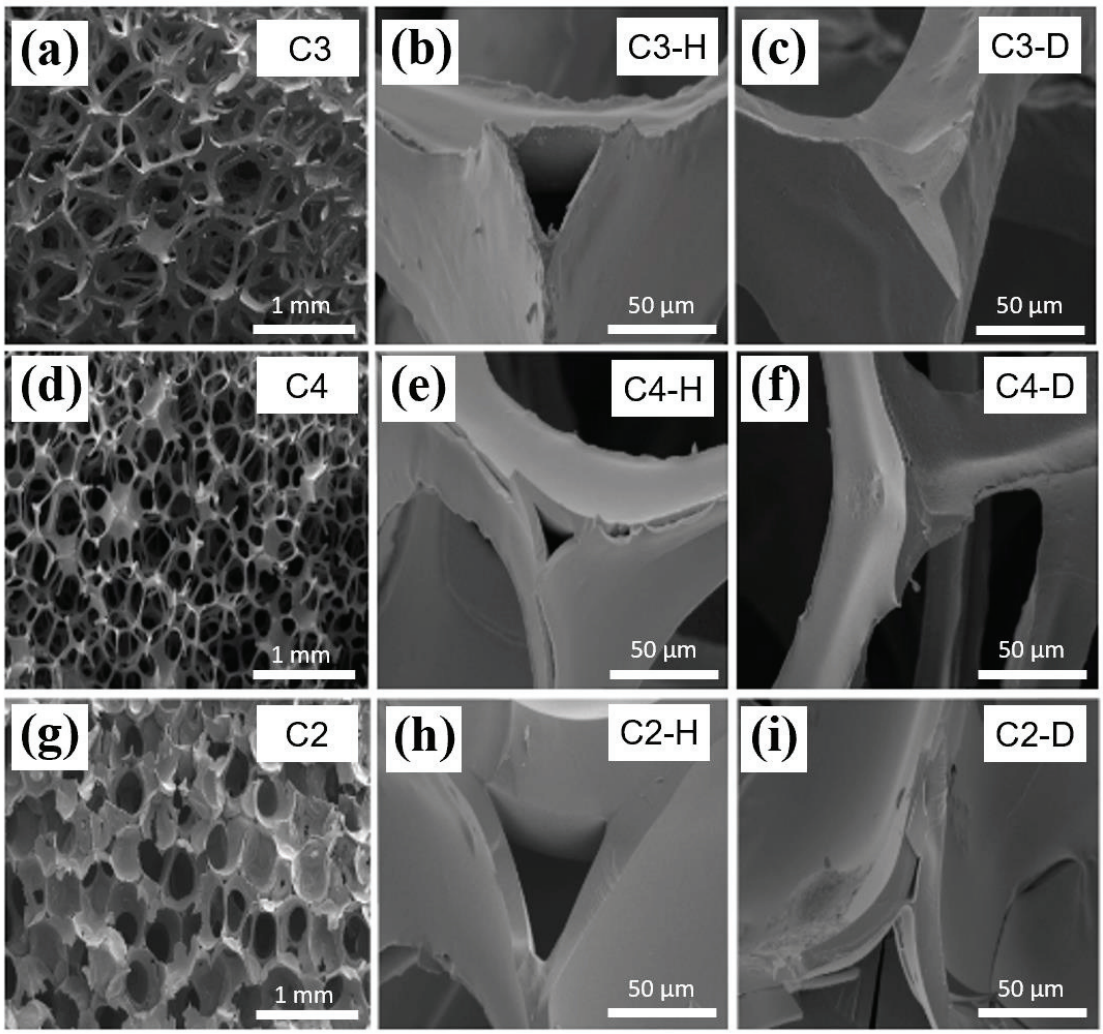

Figure 4.9. (a-i) SEM images of SiOC foams consisted by dense (D) or hollow (H) struts obtained from 59 ppi (C2), 65 ppi (C3), and 80 ppi (C4) PU foams.

Although Figure 4.9 shows only the samples made using 100% PHMS, very similar micrographs belonging to the rest of the sample set (with PDMS additions) can be seen in Figures 4.10 and 4.11. It can be seen that some cracks occurred in the structure with a PDMS addition as seen in Figure 4.10 (d), but no cracks were observed in other samples.

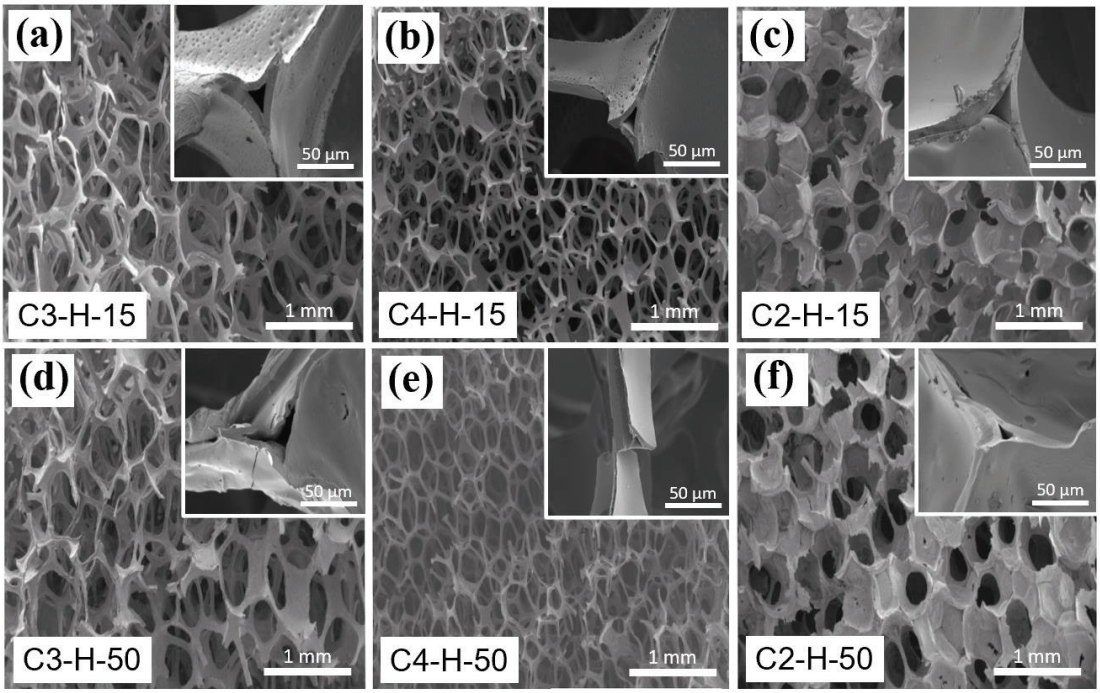

Figure 4.10. (a-f) SEM images of SiOC foams with hollow (H) strut obtained from 59 ppi (C2), 65 ppi (C3), and 80 ppi (C4) PU foams. The insets taken from higher magnification show the cross-section of the struts. 15 and 50 represent PHMS/PDMS weight ratios of 1.7/0.3 and 1/1.

Homogenous dense struts were observed as depicted in Figure 4.11 despite the PDMS addition. It was recently shown that ceramic foams produced with AM had some processing limitations to obtain strut diameters lower than 500 µm.[230] Here, it was demonstrated that SiOC foams having struts with less than around 60 µm thickness could be obtained.

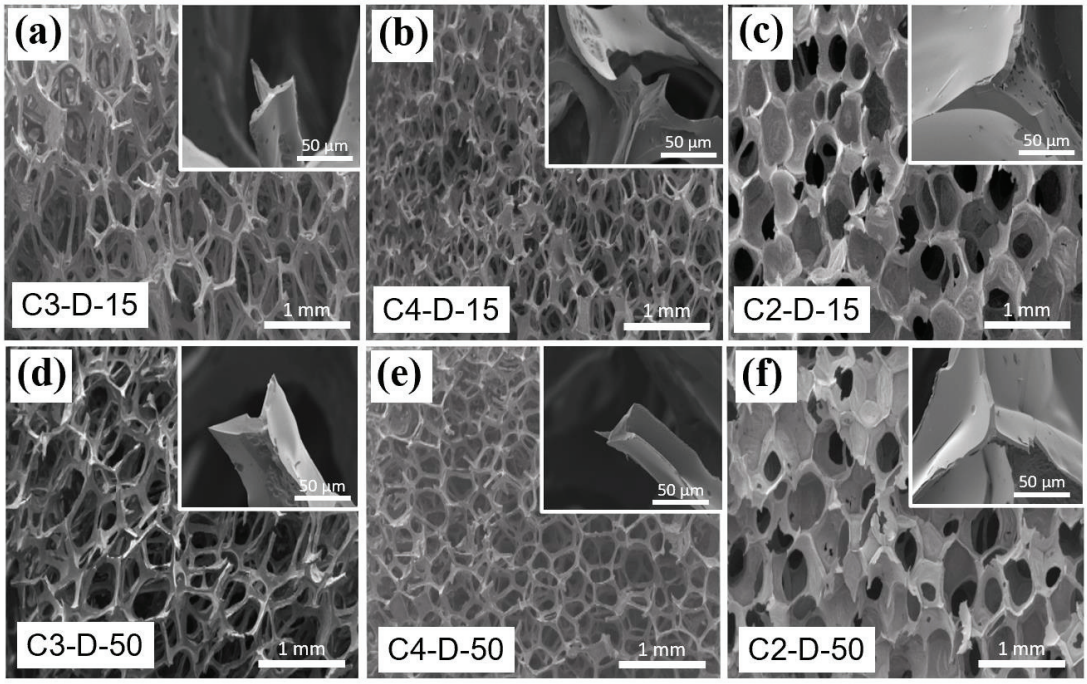

Figure 4.11. (a-f) SEM images of SiOC foams including dense (D) strut obtained from 59 ppi (C2), 65 ppi (C3), and 80 ppi (C4) PU foams. The insets show the cross-section of the struts. PHMS/PDMS weight ratios of 1.7/0.3 and 1/1 refer to 15 and 50.

Figure 4.12 shows the cell structures of SiOC foams having dense struts obtained from different PU foams. While SiOC foam (C2-D) showed a partially closed cell structure, SiOC foams (C1-D, C3-D, and C4-D) with reticulated structures showed a 3D interconnected porosity.

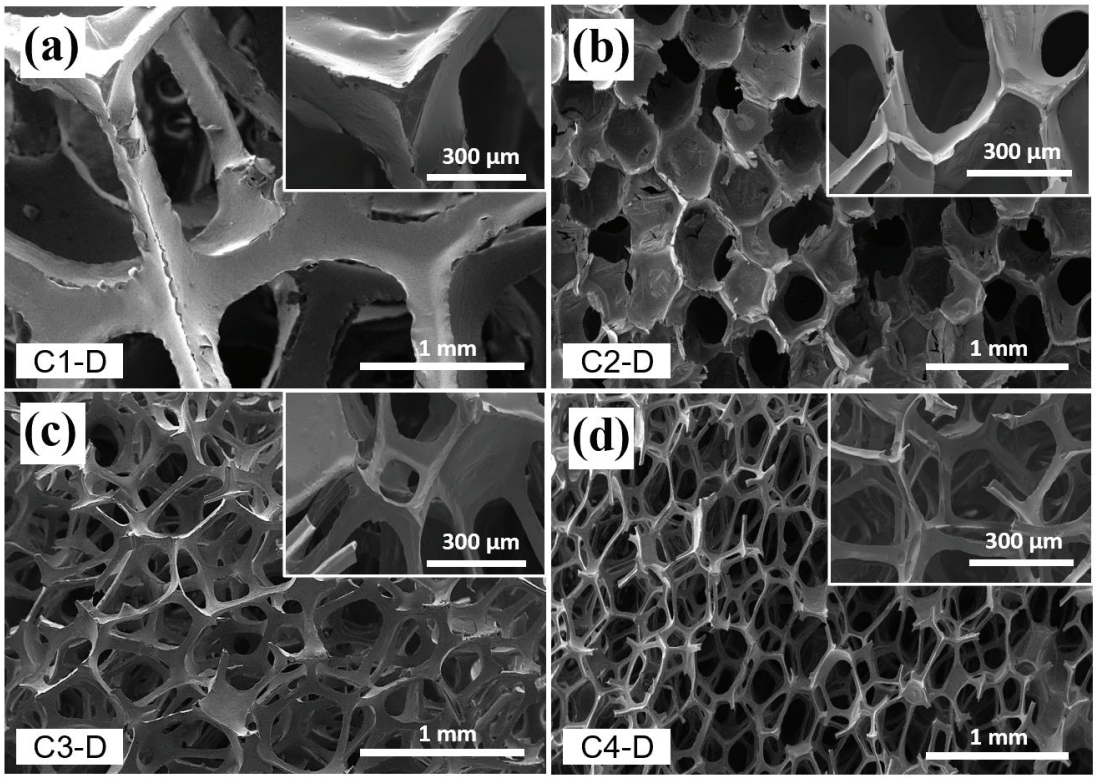

Figure 4.12. (a-d) SEM images of SiOC foams with dense (D) struts obtained from 10 ppi (C1), 59 ppi (C2), 65 ppi (C3), and 80 ppi (C4) PU foams. The insets taken from higher magnification show the cross-section of the struts.

SEM images obtained from the fracture surfaces of SiC, SiOC(N) foam, and AM-made cellular structures are shown in Figures 4.13 and 4.14. As can be seen in Figure 4.13 (a), C5-D has an open-cell (3D interconnected porous) structure, and the inset image shows that the struts are dense. SiC has an open cell structure and hollow struts as seen in Figure 4.13 (b).

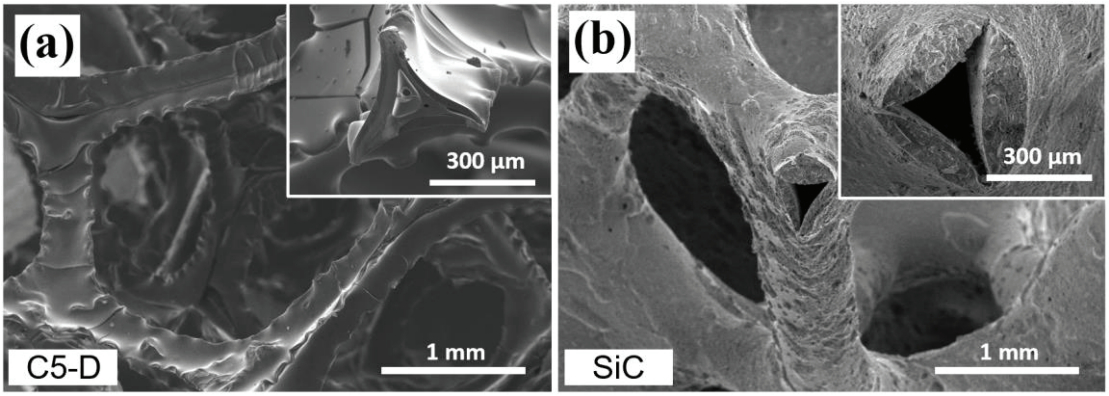

Figure 4.13. SEM images of (a) SiOC(N) foam having dense (D) strut, and (b) SiC foam with insets showing the cross-section of the struts.

Figure 4.14 shows the SEM images of AM-made SiOC(N) cellular structures, and the inset images demonstrate fully dense struts, indicating that the impregnation was complete. In this case, two different AM-made SiOC(N) cellular structures were produced: the one with a smaller cell size of 578.1 ± 14.7 µm (C6-D), and a larger cell size of 1040.8 ± 66.9 µm (C7-D), both having the strut thickness of ~150 µm.

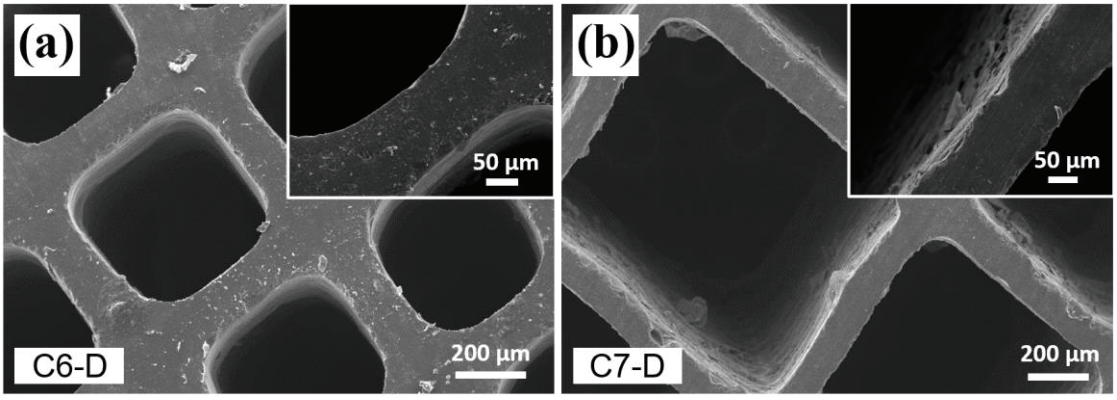

Figure 4.14. SEM images of AM-made SiOC(N) cellular structures: (a) the one with smaller cell sizes (C6-D), and (b) the one with larger cell sizes (C7-D). The insets taken from higher magnification show the cross-section of the struts.

After the analysis of the microstructural properties of the PDC component by SEM, measured cell, pore, and strut size values for all samples are given in Table 4.2. It is important to note here that for foams, cell size and pore size may differ when the cell has a small-sized opening on the cell face/wall, generally called a cell window (see Figure 2.5). For the samples produced via AM, cell size means the pore size since the cell window is virtually the same as cell size.[282]

Table 4.2. The properties of the tested porous PDC components in high temperature applications.

	Sample Code	Template Type	Cell Size (µm)	Pore Size (µm)	Strut Size (µm)
SiOC foam	C1	10 ppi PU	4039.3 ± 313.3	2042.8 ± 527.4	335.1 ± 65.8
	C2	59 ppi PU	656.2 ± 116.8	429.2 ± 66.1	61.5 ± 12.4
	C3	65 ppi PU	779.1 ± 202.9	390.9 ± 93.8	49.8 ± 11.2
	C4	80 ppi PU	693.8 ± 65.3	316.5 ± 75.3	36.3 ± 8.1
SiOC(N) foam	C5	10 ppi PU	4651.4 ± 518.2	2178.3 ± 226.1	380.1 ± 59.7
Commercial SiC foam	SiC	10 ppi PU	5968.1 ± 879.1	2750.2 ± 661.1	497.7 ± 240.6
AM-made SiOC(N) cellular structure	C6	TPU	578.1 ± 14.7		165.7 ± 6.2
	C7		1040.8 ± 66.9		153.7 ± 13.8

4.1.2.3. Microstructural Investigation of SiOC foams by CT

Figures 4.15 and 4.16 show the 2D and 3D tomographic images of SiOC having dense struts obtained from different PU foams and processed with 100% PHMS. One 2D image of SiOC foam (C2-D) showed the variation in the strut coating uniformity through the presence of darker regions in the radial slices in Figure 4.15 (c). It was not possible to determine the porosity and the cell size distribution by using 2D images because of the high degree of 3D interconnections of struts and cells and the interference caused by the superposition of solid and void fractions among the adjacent slices.

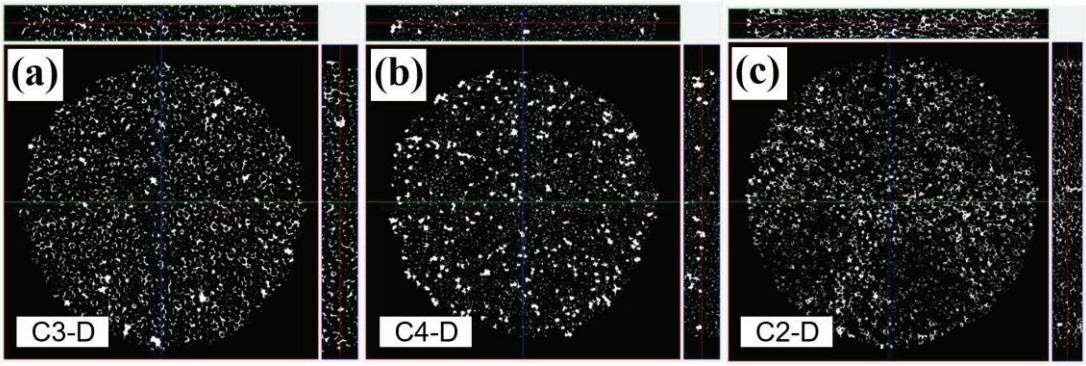

Figure 4.15. 2D tomographic images with radial and axial profiles of SiOC foams including dense (D) strut obtained from 65 ppi (C3), 80 ppi (C4), and 59 ppi (C2) PU foams.

Some macroscopic aspects were confirmed by comparison of 3D tomographic images given in Figure 4.16.

(i) C2 foam showed poor coating due to the difficulty to complete swelling of the closed cells,
(ii) C3 foam had a reticulated structure that was uniform, with larger fully interconnected, and nonaligned cells,
(iii) C4 foam showed thinner struts with smaller cells and some nonuniform coating.

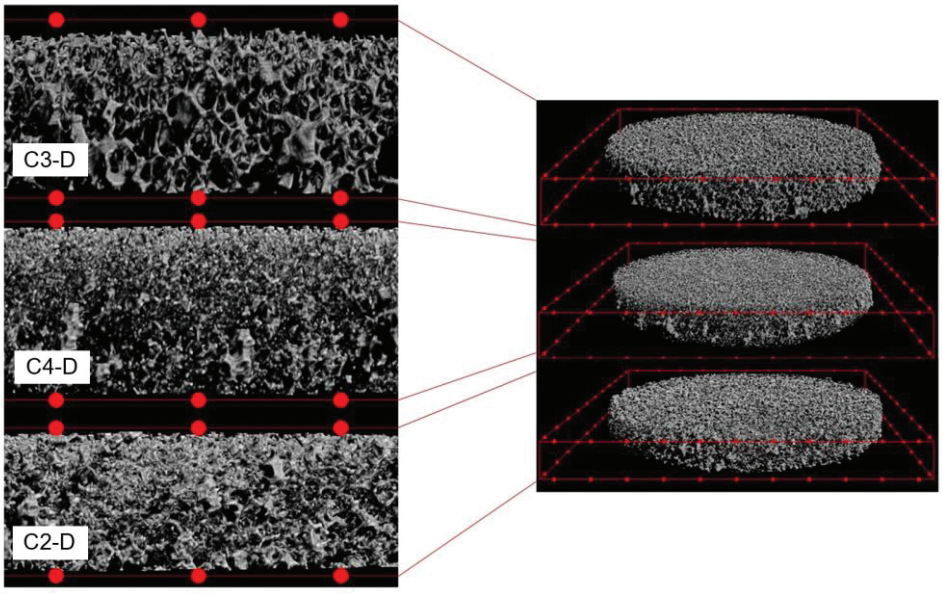

Figure 4.16. 3D tomographic images of SiOC foams with dense (D) strut obtained from 65 ppi (C3), 80 ppi (C4), and 59 ppi (C2) PU foams. The distance between two red grids is 2.5 mm.

4.1.2.4. Porosity and Surface Area of PDC Components

I) Porosity of PDC Components

The influence of the PU foam, curing conditions, and PDMS addition on the skeletal density, and total porosity of SiOC foams is shown in Figure 4.17. The average skeletal density of all SiOC foams was found to be 2226 ± 107 kg/m^3, which is in the typical range reported in the literature (from 1964 to 2380 kg/m^3).[206,223] Having dense (2229 ± 65 kg/m^3) or hollow struts (2227 ± 138 kg/m^3) did not change the skeletal density, and similar results were obtained. This means a possibly similar chemical composition for the obtained SiOC foams without any dependence on the curing condition. No conclusive influence was observed on the skeletal density of the used PU foam type, while a difference was observed in the total porosity. The average total porosity value for SiOCs was 95.7 ± 2.1 vol% - a clear increase in the PDMS in each

foam type - which in turn caused a further increase in the total porosity, as shown in Figure 4.17. The SiOC foam with the lowest total porosity (93.5 ± 1.2 vol% for dense and 92.8 ± 2.2 vol% for hollow strut) were those produced with the 59 ppi PU foam (C2) with partially closed cells.

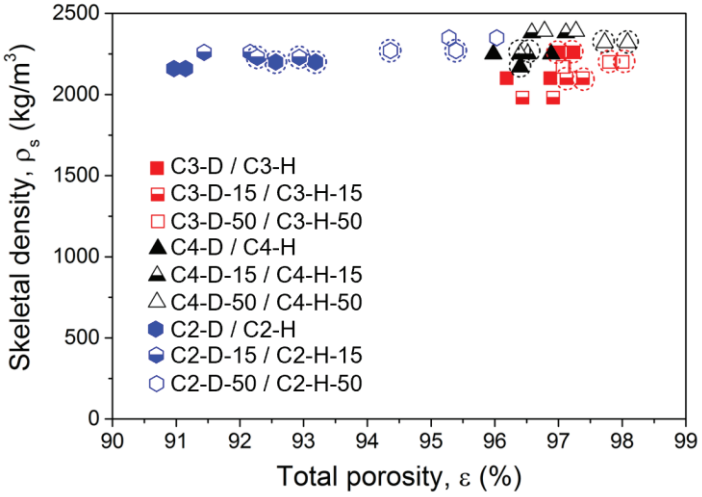

Figure 4.17. Skeletal density and porosity of SiOC foams consisting of dense (D) or hollow (H) struts obtained from 59 ppi (C2), 65 ppi (C3), and 80 ppi (C4) PU foams. 15 and 50 represent the PHMS/PDMS weight ratios of 1.7/0.3 and 1/1. The circles surrounding the data demonstrate the foams having dense struts while the regular data show the hollow struts.

Bulk densities of SiOC and SiOC(N) foams were measured to compare total porosities. SiOC (C1-D) and SiOC(N) (C5-D) foams showed similar bulk densities of 0.05 ± 0.01 g/cm^3 and 0.04 ± 0.01 g/cm^3 due to their similar pore sizes. The skeletal densities of SiOC and SiOC(N) were found to be 2.19 g/cm^3 (see Figure 4.17) and 2.12 g/cm^3.[132] Accordingly, the total porosities of C1-D and C5-D were calculated as 97.7 vol% and 98.1 vol%. In contrast to foams, AM-made SiOC(N) cellular structures (C6-D and C7-D) showed different bulk densities of 0.83 ± 0.02 g/cm^3 and 0.34 ± 0.01 g/cm^3 because C6-D had a smaller cell size (578.1 ± 14.7 µm) than that of the C7-D (1040.8 ± 66.9 µm). The total porosities of C6-D and C7-D were calculated as 60.8 vol% and 83.9 vol%.

II) Surface Area of PDC Components

N_2 sorption analysis isotherms with the pore size distributions of SiOC foams including hollow struts obtained from 65 ppi PU foam are given in Figure 4.18. Hierarchical pores that existed from 2 to 10 nm (peaking around 4 nm) were observed. It has already been shown that when preceramic polymer mixtures with similar PDMS (MW ~62,700) components are pyrolyzed, decomposition of the resulting material contains 5-20 nm ranged pores and enhances the SSA due to the decomposition of the PDMS component.[264] This result is consistent with the measured SSA and pore volume at 0.39 m^2/g and 0.0004 cm^3/g (C3-H), 7.65 m^2/g, and 0.012 cm^3/g (C3-H-15), 79.21 m^2/g and 0.096 cm^3/g (C3-H-50), respectively.

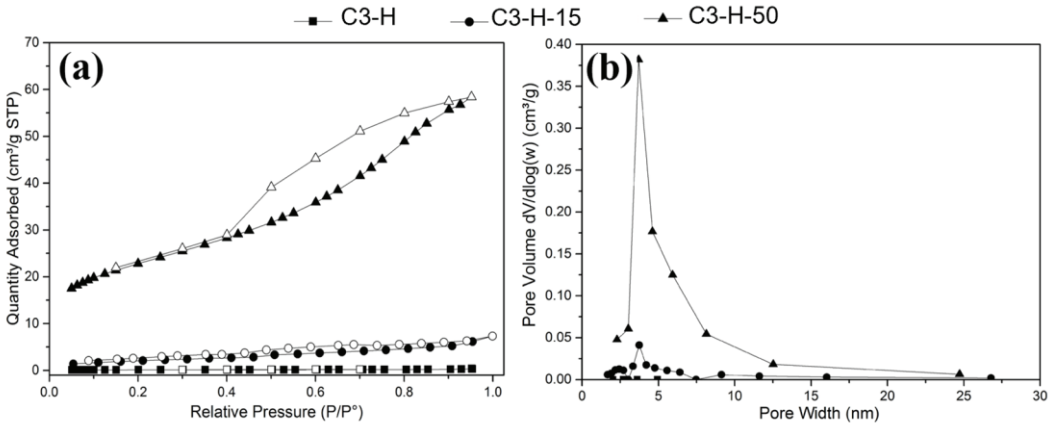

Figure 4.18. (a) N_2 sorption analysis isotherms and (b) the pore size distributions of SiOC foams having hollow (H) struts obtained from 65 ppi (C3) PU foam. PHMS/PDMS weight ratios of 1.7/0.3 and 1/1 refer to 15 and 50.

Specific surface area per unit volume (S_v) of PDC components, based on the work of Gibson and Ashby,[282] were calculated according to Richardson et al. (Eqn. 3.10):[283]

$$S_v = \frac{12.979\left[1-0.971(1-\varepsilon)^{0.5}\right]}{d_p(1-\varepsilon)^{0.5}} \quad (3.10)$$

where:

ε is the solid porosity,

dp is the pore diameter.

Table 4.3 shows the volumetric specific surface area of PDC components. The results indicate that PDC foams had a greater volumetric surface area (~35,000 - 37,000 $m^2 \cdot m^{-3}$) than that of the AM-made cellular structures (~14,000 - 18,000 $m^2 \cdot m^{-3}$).

Table 4.3. Volumetric surface areas (S_v) of PDC components.

	Sample Code*	**Porosity (vol%)**	**Sv ($m^2 \cdot m^{-3}$)**
SiOC foam	C1-D	97.72	35,957
SiOC(N) foam	C5-D	98.10	37,583
AM-made SiOC(N) cellular structure	C6-D	60.80	14,061
	C7-D	83.90	18,984

*The representative sample codes will be as follows; C: Ceramic, D: Dense.

Richardson et al.[283] proposed three different models to calculate the specific surface area per unit volume (S_v) of 10-65 ppi ceramic foams. It was suggested to use Eqn. 3.10. It was also stated that the calculated S_v is valid for uniform porosity with regular shapes, and the results may not be clear in irregular porous structures.[283] 8-45 ppi ceramic foams obtained from SiC-Al_2O_3 powders by the replica technique were measured for water/air permeability. It was shown that 45 ppi ceramic foam provided a higher S_v than that of 8 ppi foams.[284,285]

4.1.3. Mechanical Properties

4.1.3.1. SiOC Foams

A photographic image of produced SiOC foams (dimensions of ~5 x 5 x 5 mm^3) for the mechanical test is given in Figure 4.19.

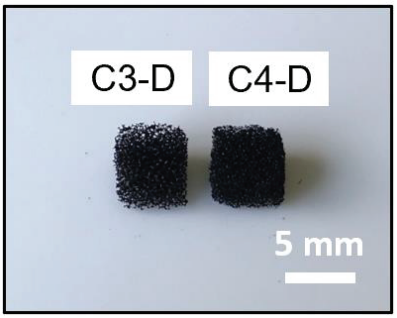

Figure 4.19. Photographic image of SiOC foams having dense strut (D) obtained from 65 ppi (C3) and 80 ppi (C4) PU foam.

The effect of porosity on compressive strength has been comprehensively discussed in recent reviews showing that ceramic materials with closed porosity have enhanced strength than those with open porosity.[70] Both relative density and the cell size affect the compressive strength; the increase in relative density causes an increase in strength. Hence, for the same relative density, the strength of the material decreases with the increase in pore size.[286] Table 4.4 shows that open-cell SiOC foams had lower crushing strength (0.208-0.244 MPa) when compared to those with partially closed porosity (~0.883 MPa) even though there was only a slight difference in the relative density values.

The effect of bulk density on the compressive strength of SiOC foams was shown by Colombo et al.[287,288] Macro-cellular (100-600 μm cell sizes) open-cell SiOC foams (0.25-0.58 g/cm^3 bulk density) showed a compressive strength of ~2-11 MPa.[287] Open-cell SiOC foams (~0.05-0.08 g/cm^3 bulk density) having cell sizes of 690-780 μm showed a compressive strength of ~0.16-0.24 MPa (see Table 4.4).

Table 4.4. Compressive strength of SiOC foams with dense (D) or hollow (H) struts obtained from 59 ppi (C2), 65 ppi (C3), and 80 ppi (C4) PU foams. 15 represents PHMS/PDMS weight ratio of 1.7/0.3.

Sample Code	Compressive Strength (MPa)	Total Porosity (vol%)
C2-D	0.883 ± 0.377	92.92 ± 0.358
C2-H	0.745 ± 0.220	91.81 ± 0.316
C2-D-15	0.671 ± 0.411	92.74 ± 0.536
C2-H-15	0.294 ± 0.184	92.59 ± 0.326
C3-D	0.234 ± 0.082	97.15 ± 0.072
C3-H	0.180 ± 0.104	96.77 ± 0.284
C3-D-15	0.208 ± 0.077	97.03 ± 0.425
C3-H-15	0.164 ± 0.049	97.18 ± 0.072
C4-D	0.244 ± 0.105	96.48 ± 0.129
C4-H	0.181 ± 0.106	96.97 ± 0.200
C4-D-15	0.214 ± 0.027	96.78 ± 0.070
C4-H-15	0.166 ± 0.033	97.25 ± 0.110

It was shown that SiOC foams having dense struts showed higher compressive strength (~0.52 MPa) than those with hollow struts (~0.44 MPa).[108] Similar results were obtained for the produced SiOC foams. SiOC foams having dense struts showed higher compressive strength (~0.24 MPa) than those with hollow struts (~0.18 MPa), as shown in Table 4.4 and Figure 4.20. It is also important to note that the strength values obtained from open-cell SiOC foams produced in this study were lower compared to what had been observed for other open-porous SiOC components.[108] Some factors including defect formation during sample preparation, differences in the relative density and cell size, and the presence of residual strut porosity can cause this difference. When PMDS was added to the structure matrix (also in the struts), compressive strength decreased, as seen in Figure 4.20. After the evaluation of all samples, results indicate that the decrease in pore size caused an increase in strength.

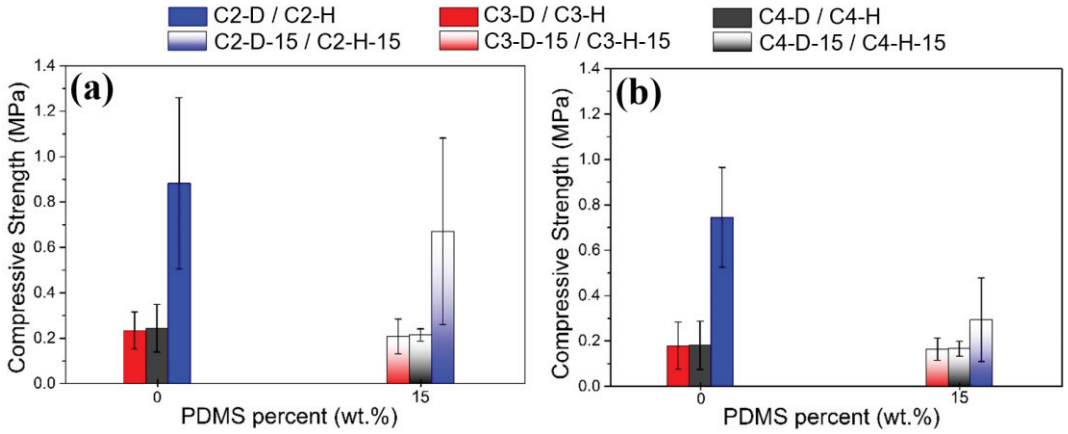

Figure 4.20. Compressive strength of SiOC foams including (a) dense (D), and (b) hollow (H) struts obtained from 59 ppi (C2), 65 ppi (C3) and 80 ppi (C4) PU foams. 15 represents PHMS/PDMS weight ratio of 1.7/0.3.

Stress-strain curves of SiOC foams having both dense and hollow struts processed with 100% PHMS are shown in Figure 4.21. The onset of brittle crushing was around 5% for open-cell SiOC foams [C3 and C4 samples, see Figure 4.21 (b&c)], which is a typical value for highly porous foams.[282,289]

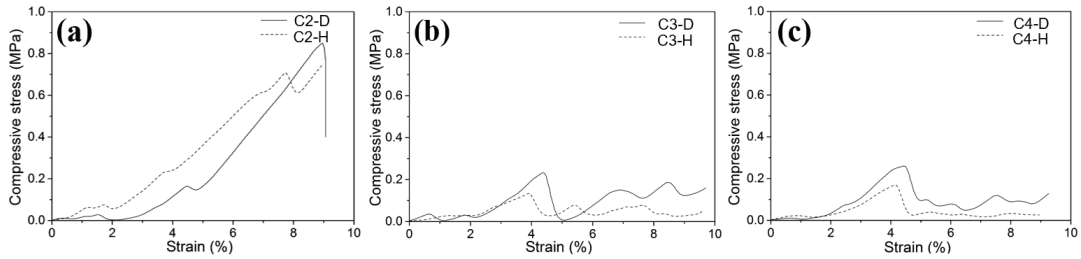

Figure 4.21. (a-c) Stress-strain curves of SiOC foams consisted by dense (D) or hollow (H) struts obtained from 59 ppi (C2), 65 ppi (C3) and 80 ppi (C4).

4.1.3.2. PDC Foams vs. Cellular Structures

Figure 4.22 shows the produced photographic image of SiOC foam (dimensions of ~10 x 10 x 10 mm^3) for the mechanical test.

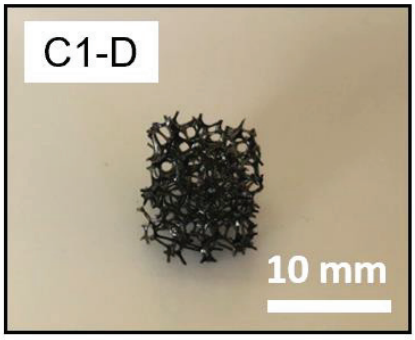

Figure 4.22. Photographic image of SiOC foam with a dense strut (D) obtained from 10 ppi PU (C1) foam.

It was shown that the mechanical strength of ceramic cellular structures produced by using AM of preceramic polymers could reach around 30 MPa. This value is almost an order of magnitude higher compared to those seen in the foams obtained via replica.[13,14,108,272] Additionally, total porosity (the difference of ~98 vol% of foams with ~80 vol% of AM filters), cell size/type (open/closed) and topology affect the strength.[70]

The average compressive strengths of C1-D and C5-D foams having dense struts were found to be 0.079 ± 0.005 MPa (4039.3 ± 313.3 μm cell size) and 0.027 ± 0.004 MPa (4651.8 ± 518.2 μm cell size). Commercial SiC foams with 80.7 vol% total porosity and pore size of ~2500 μm showed a compressive strength of ~1.2 MPa.[290] C6-D and C7-D cellular structures produced by the impregnation of the AM structure were found to be much stronger than those foams. For the samples with a cell size of 578.1 ± 14.7 μm (C6-D), the compressive strength was found to be 27 ± 3 MPa, and for the cell size of 1040.8 ± 66.9 μm (C7-D), the compressive strength was found to be 22 ± 3 MPa.

4.1.4. High Temperature Applications

The produced porous PDC structures were tested for gas permeability (at R.T. and up to ~700 ^{o}C), molten metal filtration, and heat exchanger. The results will be given in the following subsections.

4.1.4.1. Gas Permeability

The ranges of superficial air velocities (v_s) achieved in the ambient condition tests were 0-0.10 m/s for C2, 0-0.75 m/s for C3, and 0-0.23 m/s for C4 samples. Despite the apparent low v_s values, the maximum contribution of inertia on the total pressure drop was calculated by Eqns. 3.5 and 3.6 and reached 26-39% (C2), 37-75% (C3), and 25-47% (C4) as described by the caption of Figure 4.23. This indicates that the dependence of pressure drop with v_s was non-linear; therefore, Darcy's law should not be used for fitting purposes. Indeed, the Darcian (k_1) and non-Darcian (k_2) permeability coefficients were retrieved from high-quality parabolic fittings of Forchheimer's equation (Eqn. 3.1) and are given in Figure 4.23 (a&b) as a function of the total porosity of samples. The permeability level varied more than an order of magnitude for k_1 (0.28×10^{-9}-11.48×10^{-9} m^2) and two orders of magnitude for k_2 (0.34×10^{-5}-54.17×10^{-5} m) according to the PU foam used to produce the SiOC foams. The highest permeability was achieved for the C3 foams with larger cells, followed by the C4 foams, and finally the C2 foam with partially closed cells.

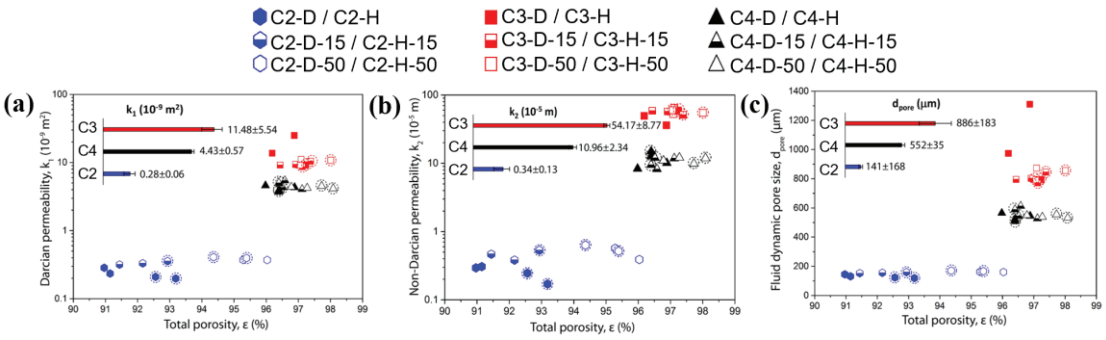

Figure 4.23. Fluid dynamic parameters obtained from the R.T. air flow permeation experiments: (a) Darcian permeability coefficient, (b) non-Darcian permeability coefficient, and (c) fluid dynamic pore size of SiOC foams having dense (D) or hollow (H) struts obtained from 59 ppi (C2), 65 ppi (C3), and 80 ppi (C4) PU foams. 15 and 50 represent PHMS/PDMS weight ratios of 1.7/0.3 and 1/1. The circles surrounding the data demonstrate the foams having dense struts while the regular data points show the ones with hollow struts.

The occurrence of dense or hollow struts did not affect the permeability coefficients since the airflow through foams is essentially macroscopic around the struts and not inside them. The literature has already identified some of the main variables that affect the macroscopic flow through ceramic replicas: cell and/or window sizes, porosity, and interconnectivity among cells.[231,268] Eqn. 3.5 was adapted from Ergun's equations that estimate the Darcian permeability coefficient (k_1) based on the knowledge of the pore size (d_{pore}) of the medium and its interconnected porosity (ε).[268] This equation is useful to estimate an effective fluid dynamic pore size once k_1 and ε of the structure is experimentally acquired. Figure 4.23 (c) gives the results for d_{pore} plotted as a function of the SiOC foam porosity. The calculated average values were 141 ± 16, 886 ± 183, and 552 ± 35 µm for the C2, C3, and C4 samples, respectively. This trend is in rough accordance with the ranges of cell size estimated from SEM images (656.2 ± 116.8, 779.1 ± 202.9, and 693.8 ± 65.3 µm). The greater discrepancy observed for the C2 samples can be explained by the lower porosity level and the presence of partially closed cell walls. This result implies that the lowest number of open pores is effective for flow and eventually affects the calculation of the fluid dynamic pore size.

SiOC foams produced in this work are compared to other porous structures in the permeability map adapted from Innocentini et al.,[206,266–270] shown in Figure 4.24. The map is made by using experimental k_1 and k_2 data extracted from the literature and used to define the permeability of porous materials. The data in the graph indicates that the manipulation of PU foams yielded SiOC foams with a broad range of permeability, as covered in the ceramic replica group. It is also worth noting that the little dispersion of $k_1 \times k_2$ data in the map for samples in each foam type, regardless of the variation of these coefficients with the pore size or porosity as depicted in Figure 4.23.

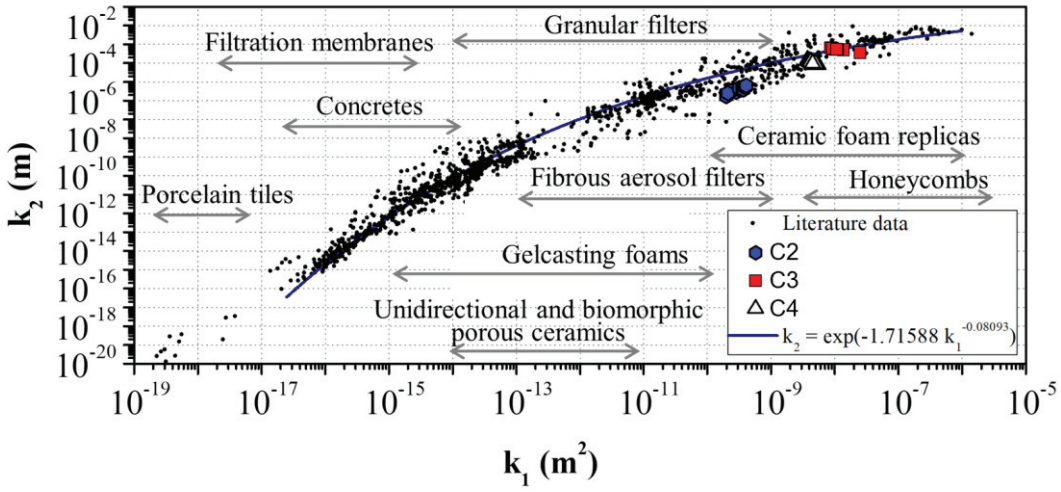

Figure 4.24. Application map for porous ceramics including SiOC foams obtained from 59 ppi (C2), 65 ppi (C3), and 80 ppi (C4) PU foams.

Hot gas permeability measurements were conducted only on the selected samples (C2-D-15, C3-D-15, and C4-D-15) since these foams had the combination of best permeability, surface area, and compressive strength. Such samples were evaluated for airflow permeation at three temperature levels: ~ 25 °C, ~ 350 °C, and ~ 700 °C. Figure 4.25 shows the length-normalized pressure drop curves ($\Delta P/L$) for the samples tested in the three temperature levels. As expected, Eqn. 3.1 was reliably fitted ($R^2 > 0.99$) to all experimental curves, confirming the significant contribution of the inertial-quadratic term [$\rho v_s^2/k_2$] to the pressure drop. The lowest $\Delta P/L$ level was achieved for the C3-D-15 sample with larger open cells, followed by the C4-D-15 sample and finally

the C2-D-15 sample with partially closed cells, corroborating the previous trends with tests at R.T.

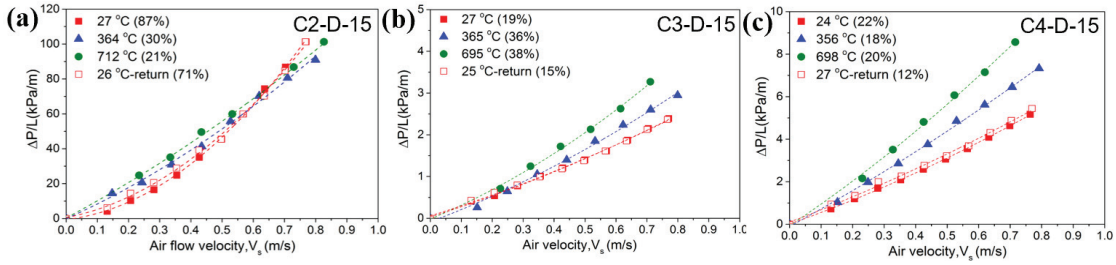

Figure 4.25. Permeation curves at increasing air flow temperatures for SiOC foams with dense (D) strut obtained from 59 ppi (C2), 65 ppi (C3), and 80 ppi (C4) PU foams. 15 represents PHMS/PDMS weight ratio of 1.7/0.3.

Airflow temperature affected the permeation profile as well. In the tested interval of 25-700 °C, a reduction of 69% in air density (from 1.11 to 0.34 kg/m^3) and an increase of ~127% in air viscosity (from 1.86x10^{-5} to 4.22x10^{-5} Pa.s) were predicted from Eqn. 3.8 and IX. Thus, proportional changes are respectively expected in the quadratic-inertial [$\rho v_s^2/k_2$] and in the linear-viscous [$\mu v_s/k_1$] terms of Eqn. 3.1. Considering the rise of the pressure drop from 25 °C to 700 °C as observed in Figure 4.25, the dominant effect was the increase in the gas viscosity.

Airflow permeation tests up to 700 °C might cause irreversible (oxidation) and/or reversible (thermal expansion effects) changes in the flow paths, which could affect both the pressure drop profile and the permeability coefficients k_1 and k_2. Nevertheless, the hypothesis of irreversible modification of the microstructure with damage to the struts by oxidation was disregarded, since permeation curves at R.T. before and after heating remained the same (see the red curves in Figure 4.25). On the other hand, Figure 4.26 shows the changes in the permeability coefficients k_1 and k_2 caused by thermal expansion during the temperature increase.

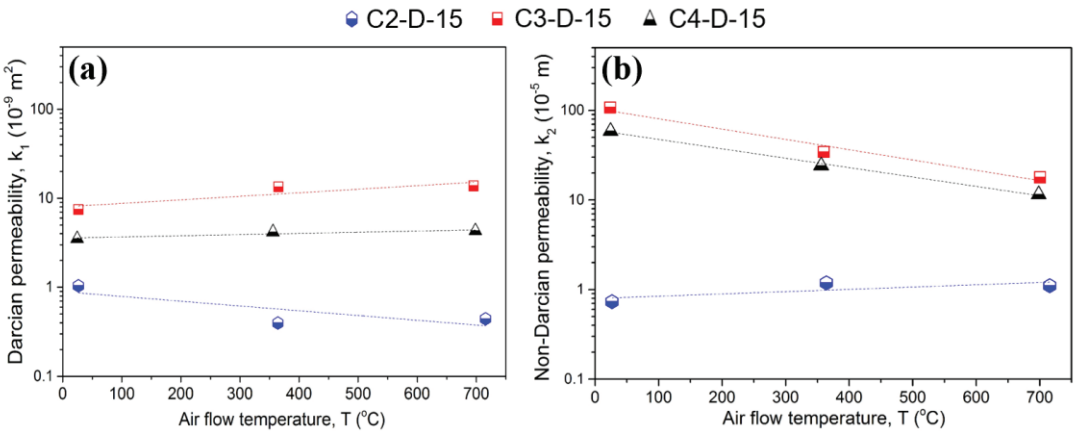

Figure 4.26. Influence of air flow temperature on the (a) Darcian and (b) non-Darcian permeabilities of SiOC foams including dense (D) strut obtained from 59 ppi (C2), 65 ppi (C3), and 80 ppi (C4) PU foams. 15 represents PHMS/PDMS weight ratio of 1.7/0.3. Dashed lines show linear fits.

The trends and ranges that can be seen in Figure 4.26 are in accordance with the values previously discussed for the tests conducted at R.T. Besides, foams C3 and C4 presented slight increases of k_1 and decreases of k_2 with the rise of the temperature to 700 °C. Similar trends were observed for freeze cast foams,[270] gel-casting foams,[269] porous lanthanum carbide discs,[291] and SiC granular filters.[266,292] Despite this, no conclusive explanation for this behavior has been proposed so far. On the other hand, the C2 foam presented opposite trends which could be related to the thermal expansion effects in the partially closed cells.

4.1.4.2. Molten Metal Filtration

SiOC (C1-D) and SiOC(N) (C5-D) foams and cellular structures (C6-D and C7-D) were analyzed for molten metal filtration and the obtained results were compared with that of the commercially used SiC foam filters.

Results for the AM-made C6-D filter were not reported since the 578.1 ± 14.7 µm channel size caused filter blocking and uncompleted fill (see Figure 4.27).

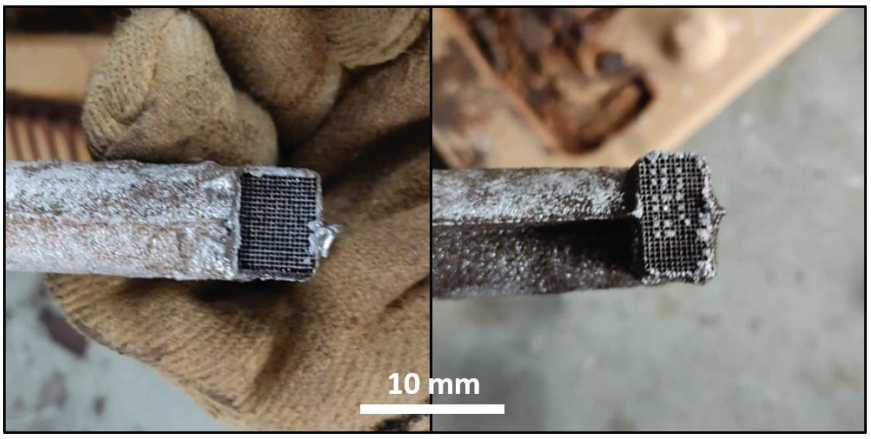

Figure 4.27. Photographic images showing the blockage of molten metal in the AM-made SiOC(N) cellular structure produced with a smaller cell size of 578.1 ± 14.7 μm.

In Figures 4.28 and 4.29, Weibull distributions and survivability plots of tensile properties which compare the different conditions are given. For the yield strength, it can be seen in Figure 4.28 (a) that apart from the sample obtained using a C5-D foam filter, almost all samples produced similar yield strength values. Weibull modulus of the ultimate tensile strength (UTS) results of the sample produced using C1-D foam was found to be 52 at the highest while the lowest value of 19 was obtained from the sample produced using no filter.

In general, UTS values for the samples produced using foam filters revealed enhanced reproducible results compared to that of the ones made by filtering via AM-made cellular monolithic filters as well as the ones without filtration. In fact, the sample obtained by using no filter had the least reliable values. A similar finding was revealed for elongation at fracture values. As seen in Figure 4.28 (c), the most reliable elongation values were observed in samples produced by using C1-D foam with 7.8, followed by C5-D foam with 7.1, while the Weibull modulus of the unfiltered castings had the lowest modulus of 2.8.

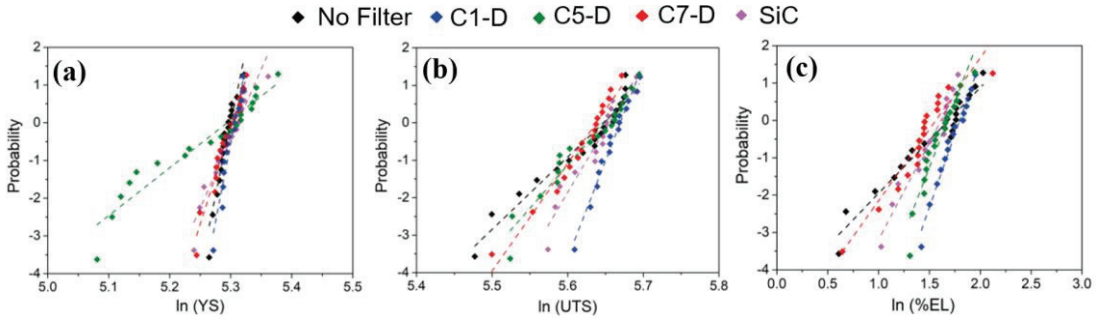

Figure 4.28. Weibull distributions of tensile test results (a) yield strength (YS), (b) ultimate tensile strength (UTS), (c) percent elongation (%EL) at fracture of SiC, SiOC foams with dense (D) strut obtained from 10 ppi (C1) PU foam, and SiOC(N) foams obtained from 10 ppi (C5) PU foam, and AM-made SiOC(N) cellular structure produced with a smaller cell size of 1040.8 ± 66.9 μm (C7).

Survivability plots are given in Figure 4.29. The plots for each parameter appear to be quite similar to each other. All yield strength values are almost overlapping as seen in Figure 4.29 (a). For UTS values, the samples produced by using C1-D foam located on the far right are followed by SiC, C5-D, and C7-D with similar slopes. The lowest slope with the highest scatter was observed for the unfiltered castings [Figure 4.29 (b)]. Almost the same sloped plot lines are seen for elongation at fracture values [Figure 4.29 (c)]. Analogous observations were reported by Nazari[293] demonstrating that minimum reliability was obtained in the unfiltered castings. Hasemi[294] and Davami[295] used Weibull statistics and showed that filtration improves reproducibility as well as enhances mechanical properties. Davami[296] proposed that 10 ppi filters were effective in reducing the oxides by around 70%, causing higher Weibull distribution in terms of tensile properties. Additionally, Basuny[297] reported that the Weibull modulus was increased three-fold when filters were used. Ardejhani[298] claimed that filtration efficiency should be over 65% to get a higher Weibull modulus.

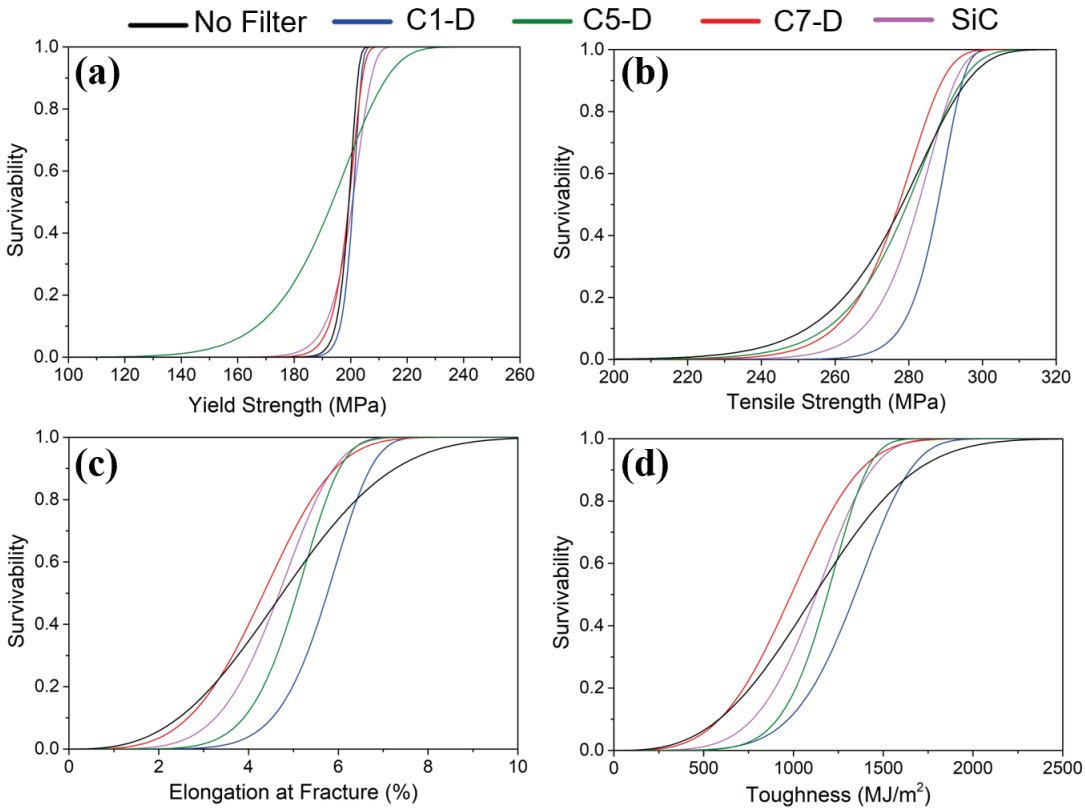

Figure 4.29. Survivability plots of tensile test results (a) yield strength, (b) ultimate tensile strength, (c) elongation at fracture, (d) ductility of SiC, SiOC foams consisted by dense (D) strut obtained from 10 ppi (C1) PU foam, and SiOC(N) foam having 10 ppi (C5) PU foam, and AM-made SiOC(N) cellular structure produced with a smaller cell size of 1040.8 ± 66.9 µm (C7).

SEM images obtained from the fracture surfaces of the cast sample that was produced by using no filter demonstrate pores around 150 µm together with a large cavity reaching 500 µm, as depicted in Figure 4.30. There are clear indications of the oxide presence, resembling a crumpled paper marked by the white arrows in Figure 4.30.[242]

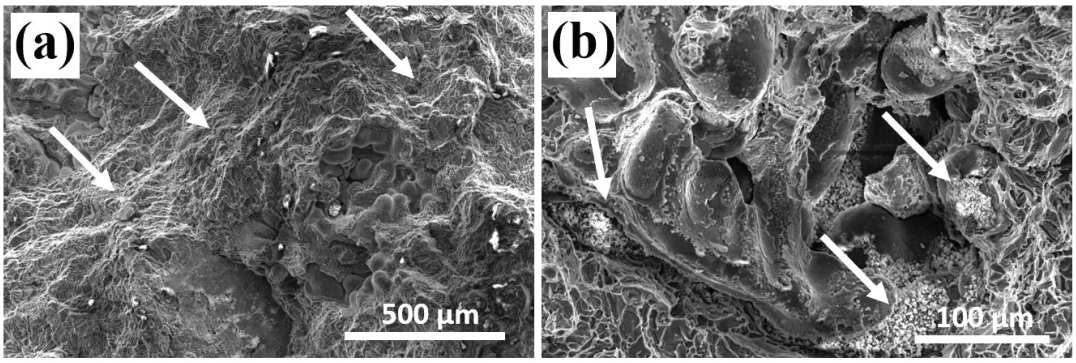

Figure 4.30. (a&b) SEM images of the fracture surface of the tensile sample produced by using no filter.

Morphological investigation of the samples that were produced by using casting filters showed a smaller number of pores/cavities, as seen in Figure 4.31. The bulk densities of samples obtained by using a C1-D foam and no filter were measured as 2.58 ± 0.01 g/cm^3 and 2.54 ± 0.02 g/cm^3. Accordingly, the total porosities were calculated as 3.4 vol% for the samples obtained using C1-D foam and 4.9 vol% for those with no filter (skeletal density of A357 alloy was taken as 2.67 g/cm^3.[299]) Samples obtained without any filter usage showed higher total porosity than that of the samples formed using C1-D foam. There were only a few dimples, and instead, more of a quasi-cleavage morphology was seen in these samples. The fracture surfaces showed no severe plastic deformation which was also confirmed by low elongation at fracture values as seen in Figure 4.29 (c). Since the fracture surfaces demonstrated similar morphologies, the ductility of these castings was also quite close to one another, with only minor differences in values [see Figure 4.29 (d)].

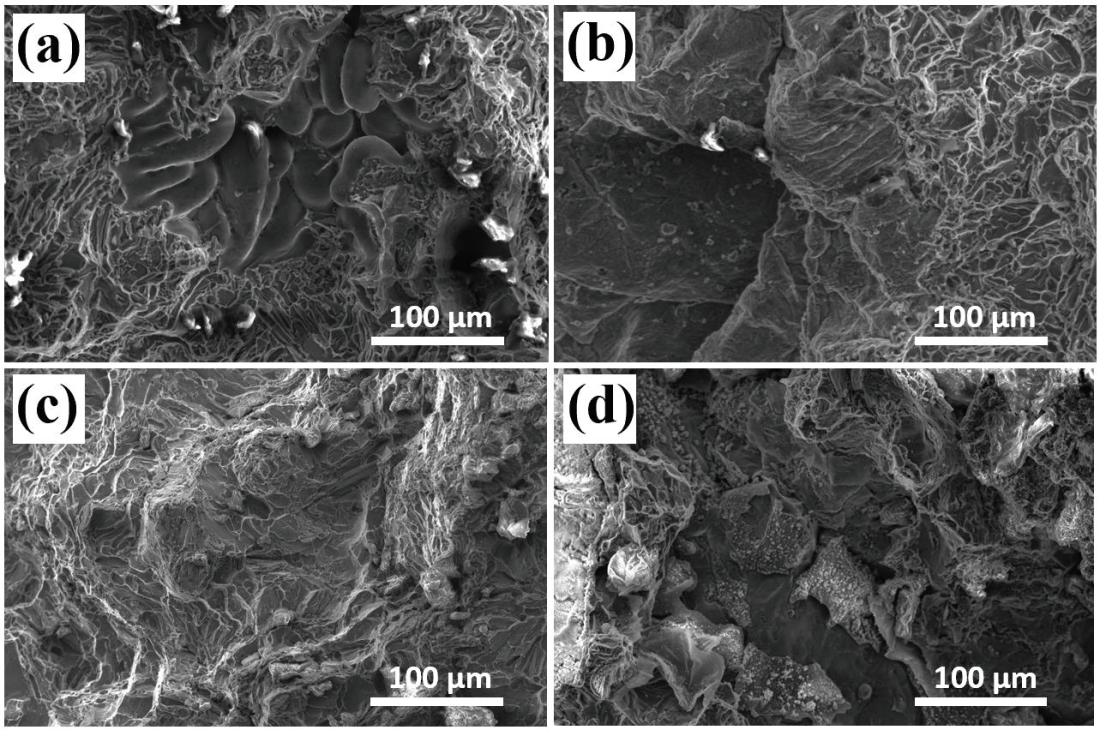

Figure 4.31. SEM images of the fracture surface of the tensile sample produced by using (a) SiOC foam having dense (D) strut obtained from 10 ppi (C1) PU foam, (b) SiOC(N) foam obtained from 10 ppi (C5) PU foam, (c) AM-made SiOC(N) cellular structure produced with a smaller cell size of 1040.8 ± 66.9 µm (C7), and (d) SiC foam.

When all backscattered electron images (Figure 4.32) obtained from the filters after casting trials were compared, it can be stated that C7-D filters had higher porosity with larger unwetted regions [indicated with white arrows in Figure 4.32(c)]. This is probably also reflected in the mechanical properties; when the data of the samples made using all other filters were compared, samples obtained by using a C7-D filter, after casting, revealed the lowest values (excluding the unfiltered castings, see above).

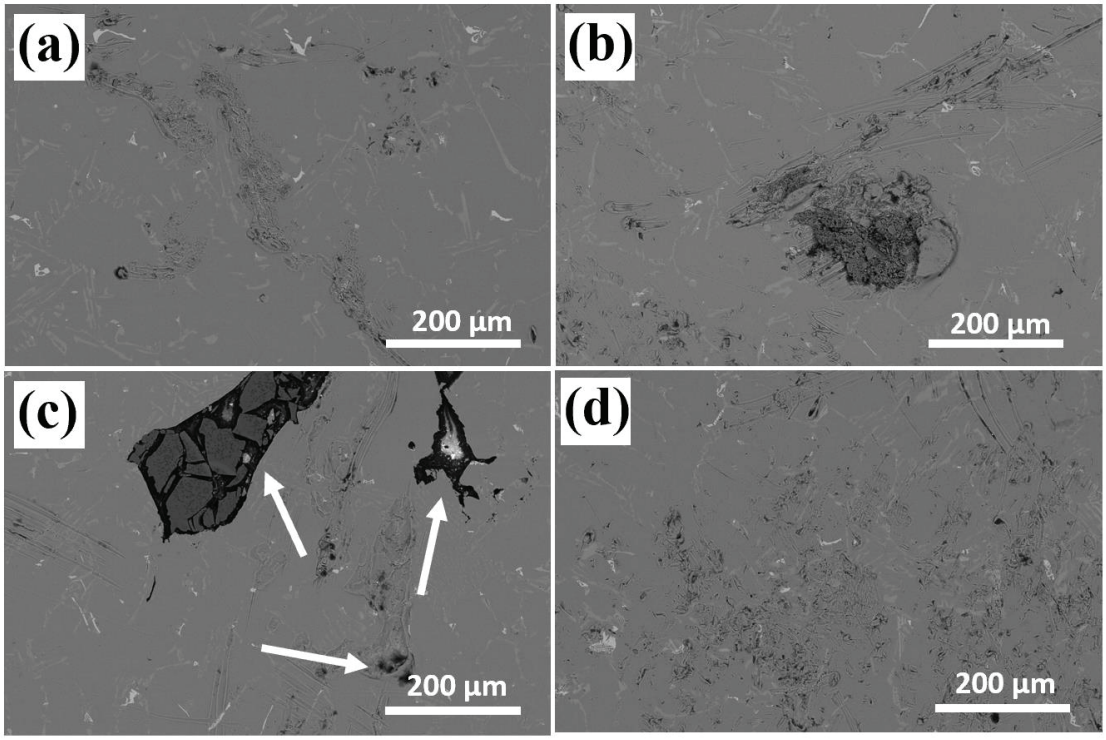

Figure 4.32. Backscattered electron images of filters after casting trials (a) SiOC foam with dense (D) strut obtained from 10 ppi (C1), (b) SiOC(N) foam consisted by 10 ppi (C5) PU foam, (c) AM-made SiOC(N) cellular structure produced with a smaller cell size of 1040.8 ± 66.9 µm (C7), and (d) SiC foam.

Although both UTS and elongation data obtained from the samples made by using C1-D foams, demonstrated slightly better performance than that of the other foam filters (C5-D and SiC), as a general trend, foams performed better in filtration than the AM-produced cellular filters. While the contributing factor might be the difference in the cell/pore size, another one is certainly the cell topology. Reticulated foams have 3D interconnected porosity, resulting in high filtration efficiency.[300] The 3D interconnected porous structures in foam filters provide a higher volumetric specific surface area, causing them to be better barriers for the inclusions and enhancing the efficiency of filtration compared to the uniaxial cellular structures formed via the AM process. Besides, it is known that 3D reticulated structures provide laminar flow. In other words, the critical velocity of the molten metal increases due to the reduction of turbulence

flow, preventing the surface defects that may occur during casting and resulting in enhanced strength values in the cast metal components.[293]

4.1.4.3. Heat Exchange

A heat exchange analysis was carried out to evaluate the heat transfer and pressure drop of the SiOC foams by taking advantage of their reticulated structure. Experiments were performed using SiOC sample (C1-D) at 900 °C furnace temperature with three different airflow rates: 0.59 (~0.6) m/s, 1.18 (~1.2) m/s, and 1.77 (~1.8) m/s. Table 4.5 shows the heat exchange test results according to air velocity.

Table 4.5. Heat exchange test results of SiOC foams including dense (D) strut and obtained from 10 ppi (C1) PU foam.

Air velocity (m/s)	T-furnace (°C)	T-sample (°C)	T-inlet (°C)	T-outlet (°C)	ΔP
0.59	900	794 ± 0.18	22 ± 0.1	260 ± 0.15	17 ± 2
1.18		786 ± 0.20		270 ± 0.56	38 ± 2
1.77		775 ± 0.25		265 ± 0.27	72 ± 2

Figure 4.33 shows that the outlet temperature (T-outlet, °C) increased in conjunction with the increase in air velocity, except for only the highest air velocity value (1.77 m/s). The reason for this decrease is the fact that the thermocouple in the output section of the alumina tube is not shielded, and it detects the radiation released from the center of the tube. Furthermore, the decrease in temperature of the sample (T-sample, °C) and increase in pressure drop (ΔP) were directly proportional to the rate of increase in the air velocity, as expected. These results are in accordance with the existing study.[246]

Further tests with different parameters (e.g., different furnace temperatures: 700 ^{o}C and 800 ^{o}C) for heat exchange are in progress and will be shared in future publications.

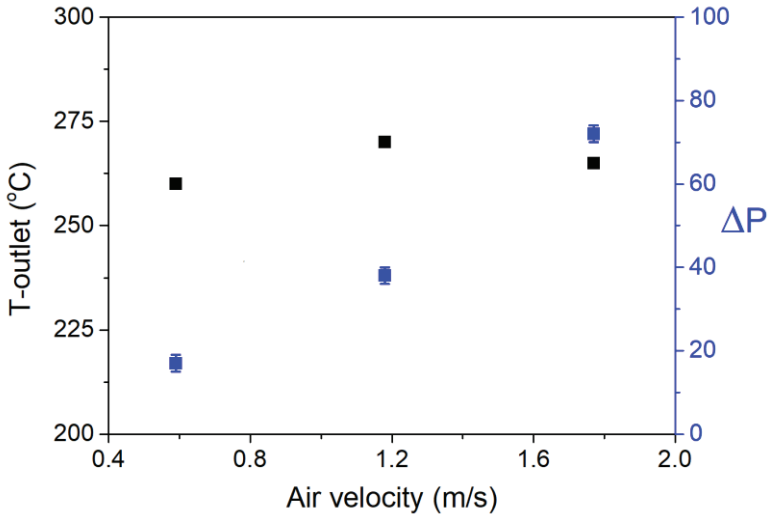

Figure 4.33. T-outlet (^{o}C) and pressure drop (ΔP) results of SiOC foams at three different air velocities: 0.59 m/s, 1.18 m/s, and 1.77 m/s. This plot also depicts the standard deviations of T-outlet temperatures; however, they are barely noticeable due to them being very small in value.

4.2. SiOC Aerogels

Structural property, porosity, and surface area of polymeric (polysiloxane) and polymer derived SiOC ceramic aerogel in addition to high temperature applications will be given in the following subsections.

4.2.1. Structural Properties of Polymeric and SiOC Aerogels

Two parameters were studied in aerogel production, the solvent amount in the mixture (vol%) and autoclave filling (vol%). Details of these production parameters for polymeric and ceramic aerogels are given in Table 3.4. Production of wet gel was not successful with a solvent amount of 80 vol% and an autoclave filling ratio of 35 vol%. Instead, when the autoclave filling was increased to 65 vol% while keeping the solvent amount at the same level (80 vol%), the reaction successfully yielded wet gel. The reason might be due to increased autogenous pressure in the reaction vessel when the autoclave filling was increased.[301]

FTIR spectra of as-received preceramic polymer (PMS), solvent (acetone), wet gels, polymeric and ceramic aerogels are shown in Figure 4.34. In the spectra of PMS, wet gels, and polymeric aerogels, absorptions of Si-CH_3 functional groups were located at 768 cm^{-1} and 1268 cm^{-1}.[281] While these peaks were present in both wet gels and polymeric aerogels, they disappeared in SiOC aerogels. The vibration band at 1100 cm^{-1} refers to the cage structure of the Si-O-Si bonds.[94,281] The absorption of C-H bond in the CH_3 group was located at 2971 cm^{-1}.[94] The spectra of polymeric aerogels showed all functional groups of PMS. Moreover, a sharp peak around 1700 cm^{-1} was associated with C=O stretching in acetone. This peak was present in wet gels, but it was not observed in polymeric aerogels. This result indicates that there was no acetone in the structure of the polymeric aerogels and the drying process was completed. Another important point was that the intensity of the C=O peak in the wet gel that had 60 vol% solvent amount (A2) was less than that of the wet gel with 80 vol% solvent amount (A4).

All the evaluated SiOC aerogels showed similar peaks. While the peak located around 446 cm^{-1} referred to Si-O-Si deformation that belongs to the Si-O bond, the Si-C, and Si-O stretching vibrations were observed around 800 cm^{-1}. [52,280] A broad peak around 1070 cm^{-1} was attributed to Si-O stretching in the Si-O-Si vibrations of the silicon oxycarbide network.[107,281]

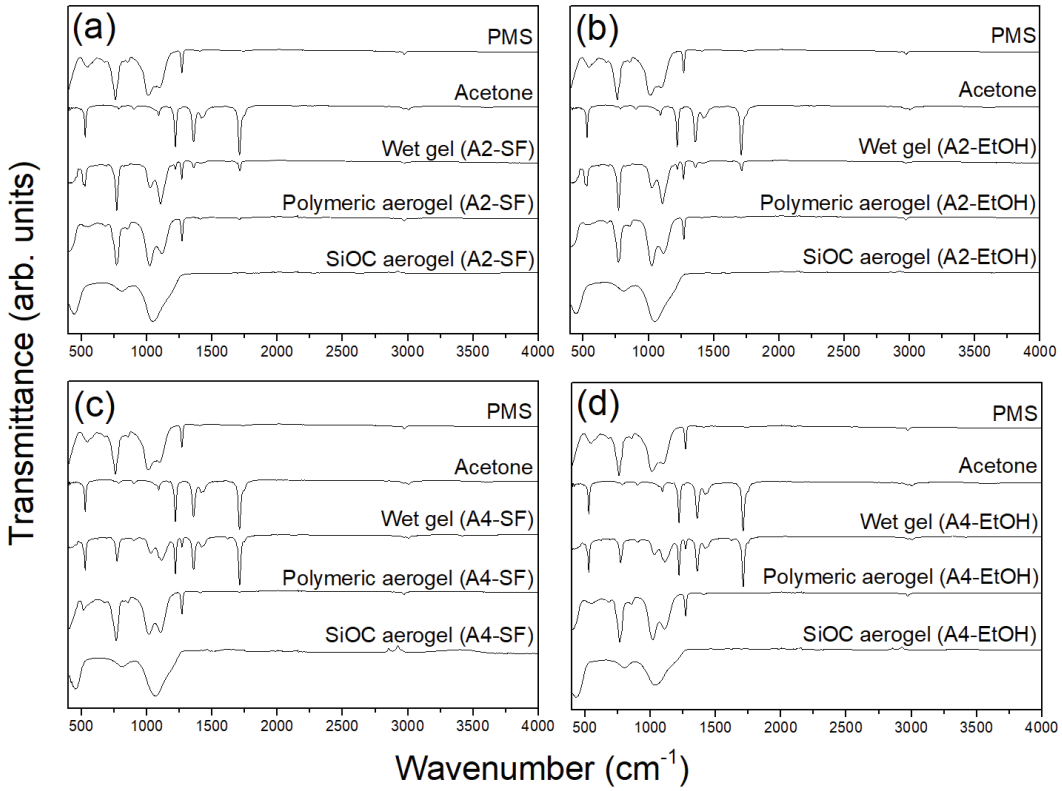

Figure 4.34. Normalized FTIR spectra of as-received PMS, acetone, wet gels, polymeric and SiOC aerogels having solvent amount & autoclave filling (vol%) as 60 & 65 (A2) and 80 & 65 (A4). SF and EtOH stand for solvent-free and ethanol drying.

4.2.2. Porosity and Surface Area of Polymeric and SiOC Aerogels

I) Polymeric siloxane aerogels

Figure 4.35 shows the photographic images of wet gels and polymeric aerogels with various solvent amounts and autoclave fillings. When autoclave fill was increased from 35 to 65 vol% while maintaining the solvent amount (60 vol%), an inhomogeneous wet gel was obtained, see Figure 4.35 (a&b). This wet gel was mostly opaque and white in color, while only the topmost part had a yellow tint. On the other hand, when autoclave filling was increased from 60 to 80 vol% while maintaining the solvent amount (65 vol%), a white and more homogeneous wet gel was obtained, as

depicted in Figure 4.35 (b&c). The effect of drying solvent on polymeric aerogel is shown in Figure 4.35 (d-f). Drying solvent did not cause a noticeable difference in polymeric aerogels. It was observed that the color difference of polymeric aerogels mostly depended on the color of the wet gel.

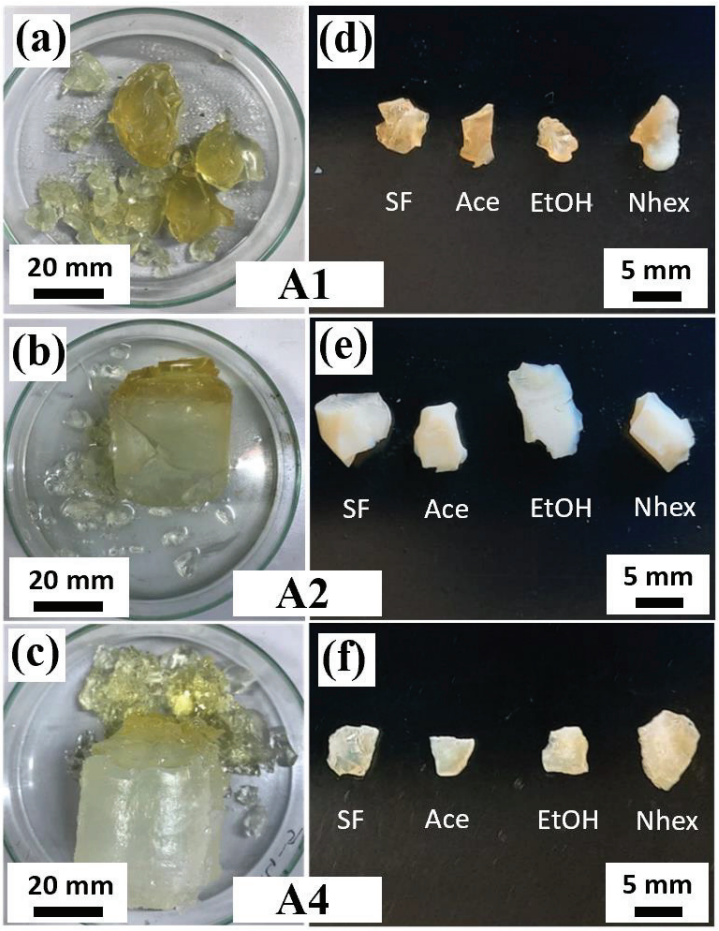

Figure 4.35. Photographic images of (a-c) wet gels, and (d-f) polymeric aerogels with solvent amount & autoclave filling (vol%) as 60 & 35 (A1), 60 & 65 (A2) and 80 & 65 (A4). Wet gels were dried with acetone (Ace), ethanol (EtOH), n-hexane (Nhex), or solvent-free (SF).

SSA values for polymeric aerogels are given in Table 4.6. The highest SSA (743.68 m^2/g) was obtained from the sample with the 60 vol% solvent amount, 35 vol% autoclave filling, and dried with ethanol; while the lowest SSA (540.82 m^2/g) was obtained from the sample with the 80 vol% solvent amount, 65 vol% autoclave filling,

and with solvent-free drying. Even though the usage of drying solvent caused a minor difference in SSA values, the type of solvent did not have any effect. It should be noted that ceramic aerogels with less SSA than polymeric aerogels are obtained due to the shrinkage of the micro/meso pores during the polymer to ceramic transformation.[187,189,196]

Table 4.6. SSA values for polymeric aerogels having solvent amount & autoclave filling (vol%) as 60 & 35 (A1), 60 & 65 (A2) and 80 & 65 (A4). The drying process was carried out with acetone (Ace), ethanol (EtOH), n-hexane (Nhex), or solvent-free (SF).

Sample Code	Solvent Amount (vol%)	Autoclave Filling (vol%)	SSA (m^2/g)
A1-SF	60	35	672.84
A1-Ace			717.80
A1-EtOH			743.68
A1-Nhex			709.43
A2-SF	60	65	654.47
A2-Ace			654.56
A2-EtOH			651.03
A2-Nhex			647.39
A4-SF	80	65	540.82
A4-Ace			551.74
A4-EtOH			616.27
A4-Nhex			576.37

II) Polymer derived SiOC aerogels

Bulk densities of SiOC aerogels were measured according to Archimedes' principle by taking the skeletal density as 2.19 g/cm^3 (see Figure 4.17). Total porosities (vol%) of the SiOC aerogels are given in Table 4.7. The trend in the SSA of polymeric aerogels was also observed in the total porosity of the SiOC aerogels. The highest total

porosity (81.84 vol%) was obtained from ethanol drying with 60 vol% solvent and 35 vol% autoclave filling. While the total porosity of ceramic aerogels obtained with 60 vol% solvent and 35 vol% autoclave filling differ according to the type of drying solvent, no difference was observed when the autoclave filling was increased to 65 vol%. It was shown that SiOC aerogel produced by using CO_2 supercritical drying had a total porosity of 72 vol%.[194] Thus, it can be said that a SiOC aerogel with a solvent amount of 60 vol% and an autoclave filling of 65 vol% provides the desired amount of total porosity that aerogels should have.

Table 4.7. Total porosities (vol%) of obtained SiOC aerogels with solvent amount & autoclave filling (vol%) as 60 & 35 (A1), 60 & 65 (A2) and 80 & 65 (A4). The drying process of wet gels was carried out with acetone (Ace), ethanol (EtOH), n-hexane (Nhex), or solvent-free (SF).

Sample Code	Solvent Amount (vol%)	Autoclave Filling (vol%)	Total Porosity (vol%)
A1-SF-SiOC	60	35	36.37
A1-Ace-SiOC			39.59
A1-EtOH-SiOC			81.84
A1-Nhex-SiOC			69.11
A2-SF-SiOC	60	65	77.85
A2-Ace-SiOC			78.80
A2-EtOH-SiOC			78.35
A2-Nhex-SiOC			78.75
A4-SF-SiOC	80	65	27.18
A4-Ace-SiOC			35.48
A4-EtOH-SiOC			40.53
A4-Nhex-SiOC			24.13

Samples were selected among SiOC aerogels according to their total porosity to determine their SSA values. The samples with the lowest and highest porosity were selected, and their SSA values are given in Table 4.8. It was shown in recent studies that SiOC aerogels dried in CO_2 supercritical drying had SSA below 200 m^2/g.[187,192,194]

Obtained total porosities and SSA values of SiOC aerogels showed a direct proportional trend, and a SiOC aerogel with high porosity (78.35 vol%) had a high SSA value (250.80 m^2/g). When the solvent amount was increased from 60 to 80 vol%, a significant decrease was observed in SSA values. The effect of the solvent amount on microstructural properties of the SiOCN aerogel (obtained from freeze drying) showed that total porosity and pore size were increased as the solvent amount in the mixture was increased, but no such trend was observed in SSA.[196]

Table 4.8. SSA values for produced SiOC aerogels with solvent amount & autoclave filling (vol%) as 60 & 65 (A2) and 80 & 65 (A4). Ethanol (EtOH) or solvent-free (SF) drying was applied to the wet gels.

Sample Code	Solvent Amount (vol%)	Autoclave Filling (vol%)	SSA (m^2/g)
A2-SF-SiOC	60	65	244.16
A2-EtOH-SiOC			250.80
A4-SF-SiOC	80	65	50.60
A4-EtOH-SiOC			147.76

After evaluating the obtained total porosity and SSA values, it is reasonable to suggest that the aerogel sample produced with a solvent amount of 60 vol% and autoclave filling of 65 vol% is promising for future studies.

4.2.3. High Temperature Applications of PDC Aerogels

One of the most popular high temperature applications of PDC aerogels is thermal insulation since these aerogels possibly provide low thermal conductivity even at high temperatures. Pure silica aerogels sinter above 600 °C, causing a significant increase in density, hence limiting pore stability.[302,303] Therefore, silica aerogels can be used as a thermal insulator up to ~600 °C, while PDC aerogels maintain an SSA value

of ~90 m^2/g up to 1600 °C.[203] The same study also suggests that the pore collapse experienced in silica aerogels was partially observed in PDC aerogels.

Another novel high temperature application of aerogels is related to the casting industry. Traditionally, the casting of metals and alloys is performed in a sand mold made with a resin-based biner.[304] Sand molds should have high gas permeability to prevent blowholes that cause pore formation in the casting due to binder decomposition.[304,305] The surface of the casting material is most desirable when it is without any casting defects. Therefore, some additives are used to overcome casting defects. For this purpose, aerogels having a high surface area and stability at high temperatures were proposed to adsorb gases formed by the thermal decomposition of the resin-based binder that is used in sand molds.[304–306] SiOC aerogels were synthesized by the sol-gel method and pyrolyzed at 1000 °C to be tested in terms of usability as casting additives.[305] Obtained aerogels were evaluated by measuring the surface roughness of the cast material and the gas permeability of the sand. It was found that when the aerogel content increased from 1 to 2 vol%, the surface roughness of the casting material decreased, but it was still higher than the surface roughness obtained from the conventional additive sand core. In the same study, it was also shown that the gas permeability of the sand core increased while the aerogel addition increased. Thus, due to their high specific surface area, aerogels increase the casting quality by absorbing the gases formed during casting.

CHAPTER 5

CONCLUSIONS AND PERSPECTIVES

Although there are many comprehensive works on the production techniques and characterization of porous polymer-derived ceramics (PCDs), the works on the applications, especially those oriented explicitly for high temperatures, are still very limited in number. Accordingly, in this thesis, porous PDC components such as three-dimensionally interconnected porosity foams, uniaxial channeled, additively manufactured honeycomb-like cellular structures, and aerogels were produced, characterized in depth, followed by testing for gas permeability (from room temperature up to ~700 ^{o}C), molten metal filtration, and heat exchanger.

Production of SiOC and SiOC(N) foams was carried out via replica technique. Briefly, commercial polyurethane foams with different cell densities ranging from 10 ppi to 80 ppi were cut, impregnated with Polymethylhydrosiloxane, crosslinked (80°C/7h + R.T./23h or 220°C/2h), and pyrolyzed at 1000 ^{o}C under Argon flow yielding SiOC foams with various pore sizes. In the additive manufacturing process, honeycomb-like SiOC(N) cellular structures were produced by fused filament fabrication of thermoplastic polyurethane, succeeded by crosslinking (160°C/3h) and pyrolysis at 1200 ^{o}C under N_2 flow. Differently, preceramic aerogels were synthesized using a commercial PMS (Polymethylsilsesquioxane) polymer, cured in acetone placed in a sealed stainless-steel autoclave at 200 ^{o}C for 6h. The formed gel was then dried at room temperature and ambient pressure to be transferred into polymer-derived ceramic aerogel.

It was demonstrated that the microstructural properties of SiOC foams could be tuned by changing processing parameters such as the PU template type (cell density and open/closed cells), crosslinking conditions (temperature, time, catalyst type), and the PDMS ratio of the preceramic blend. SiOC foam struts could be deliberately changed to be “dense” or “hollow” just by altering the crosslinking conditions. At a high temperature (220°C/2h), curing occurred quickly and did not allow the preceramic solution to swell the PU template. As a result of the pyrolysis, the PU thermally

decomposed and left behind a cavity. On the other hand, when crosslinking was conducted at a low temperature (80°C/7h + R.T./23h), curing occurred sluggishly, giving the precursor enough time to swell the PU template, forming dense struts. Additionally, it was shown that it was possible to produce ceramic replicas even with closed cells, which could not be obtained by other conventional methods. Hierarchical porosity was able to be incorporated into the SiOC structure using a vinyl-terminated PDMS that also decomposed and left behind a submicron porosity with a corresponding increase of specific surface area reaching around 80 m^2/g. The average total porosity of open cell reticulated SiOC foams was around 96 vol%, and the highest compressive strength was ~0.2 MPa.

The partially closed cell SiOC foams (total porosity of ~92 vol%) showed a compressive strength of around 1.0 MPa. This value is not adequate for many practical applications. However, there are several options that might be followed to enhance the observed strength values. For instance, multiple impregnations can be applied, or the preceramic polymer to solvent ratio can be increased, i.e., deliberate alteration of the rheological properties, during the production step. Besides those, reactive/inert fillers, including the 1D forms, e.g., fibers, of the same chemical composition PDC can be added to the mother PDC matrix. Consequently, further systematic investigations should be performed to provide foams having higher skeletal density and thicker/denser struts for obtaining better mechanical properties.

The SiOC(N) foams produced with pore sizes of 2178.9 ± 226.1 μm and total porosity of 98 vol%, showed a relatively low compressive strength of ~0.03 MPa. Instead, AM-made SiOC(N) cellular structures were produced with two different cell sizes: the one with smaller cells of 578.1 ± 14.7 μm (total porosity of 60.8 vol%), and the one with a larger cell size of 1040.8 ± 66.9 μm (total porosity of 83.9 vol%) with a strut thickness of ~150 μm for both. Compared to previously manufactured reticulated foams, these structures demonstrated to have much higher strength. The compressive strength was found to be ~27 MPa for smaller cells, which was ~22 MPa for the larger cell-sized components.

In the polymeric and SiOC aerogel production, two parameters were investigated, the solvent in the mixture (vol%) and autoclave filling (vol%). SiOC aerogel was not obtained with 80 vol% solvent and an autoclave filling ratio of 35 vol%. When the autoclave filling was increased to 65 vol% while keeping the solvent amount at the same level (80 vol%), the reaction successfully yielded a wet gel. For

polymeric aerogels, the highest SSA (~744 m^2/g) was obtained from a 60 vol% solvent and 35 vol% autoclave filling in ethanol drying. The drying solvent type had a minor effect on the SSA values, and no trend was observed between the different solvents. As a result of the pyrolysis at 1000 ^oC under Ar atmosphere, SiOC aerogel with total porosity of 78 vol% and an SSA reaching up to 250 m^2/g was produced successfully.

The PDC aerogel studies can be improved in several ways, as some of them are already in progress in our laboratories. For example, preceramic aerogels are generally pyrolyzed at temperatures above 800 ^oC to produce PDC aerogels. If one does the pyrolysis between 600-800 ^oC, ceramer aerogels with enhanced SSA due to transient porosity can be formed. Moreover, PDC aerogels have limited applications due to their low mechanical properties. For this reason, some reinforcements, i.e., fibers, can be added to enhance the aerogel strength. It is essential to note that several properties of PDC aerogels, such as mechanical strength, creep, thermal shock resistance, etc., have not been investigated yet. Therefore, there needs to be more experimenting, testing, and understanding of those structures. The resulting, appropriate PDC aerogels can be tested in future works for high-temperature applications, including as an additive for sand molds used in the foundry industry or thermal insulation. There are many other applications in which such structures may find usage. For instance, they can be used for battery anodes or as electromagnetic interference shielding materials due to their favorable dielectric properties.

For high-temperature applications, first, SiOC foams having dense and hollow struts obtained from open and partially closed cell PU foams were tested for gas permeability (from R.T. and up to ~700 ^oC). Permeability measurements obtained at R.T. indicated a variation of more than one order of magnitude for k_1 (0.28×10^{-9} - 11.48×10^{-9} m^2) and two orders for k_2 (0.34×10^{-5} - 54.17×10^{-5} m) according to the PU template used to produce the SiOC foams. The highest gas permeability was achieved for SiOC foam with open cells and followed by those with partially closed cells. Additionally, the formation of dense or hollow struts did not affect the k_1 and k_2 coefficients. Results from high temperature measurements (up to ~700°C) were proportional to the trend with tests at R.T. Hot gas permeation tests showed that the SiOC foams were stable up to 700 °C in the air without any loss of functionality. As a result, they are envisioned to be employed as reusable air filtration devices for pollutants (viruses, bacteria, dust, etc.), catalytic supports, and porous components for reactions occurring in aggressive environments.

Molten metal filtration tests were conducted using two different PDC filter types: SiOC/SiOC(N) foams and AM-made SiOC(N) honeycomb-like cellular structures. In addition, cast samples were obtained without a filter, and commercial SiC foams that are actively used in the foundry industry were tested to be compared with the produced ceramic filters. In all tests, molten aluminum alloy (A357) was used and the obtained Al samples, at the end of filtration, were characterized for their mechanical properties. Tensile test results of the unfiltered castings exhibited the highest scatter in terms of yield, ultimate tensile strength (UTS), and elongation at fracture. Overall, the samples produced with a filter demonstrated more reproducible and reliable mechanical properties when compared to the samples obtained without any filtration. The yield strength values of the cast alloys were not affected when different filters were used, and the data points stayed in the range of 190-205 MPa. Instead, the cast samples obtained by using a SiOC foam with a 4039.3 ± 313.3 μm cell size gave the highest UTS and elongation at fracture with the highest reproducible results. Considering all the filters produced and tested, the cast alloy samples that were produced by using an AM-made SiOC(N) filter with uniaxial channels of 1040.8 ± 66.9 μm demonstrated the lowest tensile. An AM-made SiOC(N) filter with 578.1 ± 14.7 μm uniaxial channels resulted in pore blocking and incomplete fill due to small cell size. Besides, foams showed a higher filtration capacity, likely due to their 3D interconnected porosity, providing a higher volumetric specific surface area than that of the cellular structures with uniaxial channels.

The AM-made cellular ceramics (total porosity of ~84 vol%) showed much higher mechanical strength than those of the foams. But they gave a low filtration capacity due to the low volumetric specific surface area compared to PDC foams with 3D interconnected porosity. It is important to note here that the pore and cell sizes of AM-cellular structures should be arranged properly since small-sized (e.g., ~500 μm) cells did not let the molten metal flow, i.e., pore blocking. However, still, if the AM foams were able to be designed well, they could find a potential application in the foundry industry. Additionally, the effect of pore size/shape/topology should be examined in future studies specifically oriented to mentioned practical applications.

Heat exchange analysis of SiOC foams was performed to evaluate the heat transfer and pressure drop at 900 °C with three different airflow rates: 0.59 m/s, 1.18 m/s, and 1.77 m/s. It was found that the outlet temperature of the tube increased alongside the increase in the airflow rate, with the only exception being the highest air

flow rate. Additionally, a decrease in the temperature of the foam and an increase in the pressure drop was directly proportional to the rate of increase in the air velocity. For heat exchangers, thermal conductivity and specific surface area are important key factors. Both the structural features and composition of the produced PDC can be tailored to enhance those properties.

REFERENCES

(1) Wen, Q.; Yu, Z.; Riedel, R. The Fate and Role of in Situ Formed Carbon in Polymer-Derived Ceramics. *Progress in Materials Science* 2020, *109*, 100623.

(2) Renlund, G. M.; Prochazka, S.; Doremus, R. H. Silicon Oxycarbide Glasses: Part II. Structure and Properties. *Journal of Materials Research* 1991, *6* (12), 2723–2734.

(3) Stabler, C.; Roth, F.; Narisawa, M.; Schliephake, D.; Heilmaier, M.; Lauterbach, S.; Kleebe, H.-J.; Riedel, R.; Ionescu, E. High-Temperature Creep Behavior of a SiOC Glass Ceramic Free of Segregated Carbon. *J Eur Ceram Soc* 2016, *36* (15), 3747–3753.

(4) Wang, Y.; Fan, Y.; Zhang, L.; Zhang, W.; An, L. Polymer-Derived SiAlCN Ceramics Resist Oxidation at 1400 C. *Scr Mater* 2006, *55* (4), 295–297.

(5) Yuan, J.; Galetz, M.; Luan, X. G.; Fasel, C.; Riedel, R.; Ionescu, E. High-Temperature Oxidation Behavior of Polymer-Derived SiHfBCN Ceramic Nanocomposites. *J Eur Ceram Soc* 2016, *36* (12), 3021–3028. https://doi.org/https://doi.org/10.1016/j.jeurceramsoc.2015.12.006.

(6) Takahashi, T.; Münstedt, H.; Modesti, M.; Colombo, P. Oxidation Resistant Ceramic Foam from a Silicone Preceramic Polymer/Polyurethane Blend. *J Eur Ceram Soc* 2001, *21* (16), 2821–2828. https://doi.org/https://doi.org/10.1016/S0955-2219(01)00220-5.

(7) Colombo, P. *Polymer Derived Ceramics: From Nano-Structure to Applications*; DEStech Publications, Inc, 2010.

(8) Colombo, P.; Mera, G.; Riedel, R.; Soraru, G. D. Polymer-derived Ceramics: 40 Years of Research and Innovation in Advanced Ceramics. *Journal of the American Ceramic Society* 2010, *93* (7), 1805–1837.

(9) Colombo, P.; Riedel, R.; Sorarù, G. D.; Kleebe, H. K. Historical Review of the Development of Polymer Derived Ceramics (PDCs). *Polymer Dervied Ceramics: From Nanostructure to Apllications* 2009, 1–12.

(10) Danko, G. A.; Silberglitt, R.; Colombo, P.; Pippel, E.; Woltersdorf, J. Comparison of Microwave Hybrid and Conventional Heating of Preceramic Polymers to Form Silicon Carbide and Silicon Oxycarbide Ceramics. *Journal of the American Ceramic Society* 2000, *83* (7), 1617–1625.

(11) Colombo, P.; Paulson, T. E.; Pantano, C. G. Synthesis of Silicon Carbide Thin Films with Polycarbosilane (PCS). *Journal of the American Ceramic Society* 1997, *80* (9), 2333–2340.

(12) Yu, Z.; Lv, X.; Mao, K.; Yang, Y.; Liu, A. Role of In-Situ Formed Free Carbon on Electromagnetic Absorption Properties of Polymer-Derived SiC Ceramics. *Journal of Advanced Ceramics* 2020, *9* (5), 617–628.

(13) Semerci, T.; de Mello Innocentini, M. D.; Marsola, G. A.; Lasso, P. R. O.; Soraru, G. D.; Vakifahmetoglu, C. Hot Air Permeable Preceramic Polymer Derived Reticulated Ceramic Foams. *ACS Applied Polymer Materials* 2020, *2* (9), 4118–4126. https://doi.org/10.1021/acsapm.0c00734.

(14) Li, Z.; Chen, Z.; Liu, J.; Fu, Y.; Liu, C.; Wang, P.; Jiang, M.; Lao, C. Additive Manufacturing of Lightweight and High-Strength Polymer-Derived SiOC Ceramics. *Virtual and Physical Prototyping* 2020, *15* (2), 163–177. https://doi.org/10.1080/17452759.2019.1710919.

(15) Gao, Y.; Mera, G.; Nguyen, H.; Morita, K.; Kleebe, H.-J.; Riedel, R. Processing Route Dramatically Influencing the Nanostructure of Carbon-Rich SiCN and SiBCN Polymer-Derived Ceramics. Part I: Low Temperature Thermal Transformation. *J Eur Ceram Soc* 2012, *32* (9), 1857–1866. https://doi.org/https://doi.org/10.1016/j.jeurceramsoc.2011.09.012.

(16) Mahmoudi, M.; Kim, S.; Arifuzzaman, A. M.; Saito, T.; Cramer, C. L.; Minary-Jolandan, M. Processing and 3D Printing of SiCN Polymer-Derived Ceramics. *International Journal of Applied Ceramic Technology* 2022, *19* (2), 939–948. https://doi.org/https://doi.org/10.1111/ijac.13927.

(17) Saha, A.; Raj, R.; Williamson, D. L.; Kleebe, H.-J. Characterization of Nanodomains in Polymer-Derived SiCN Ceramics Employing Multiple Techniques. *Journal of the American Ceramic Society* 2005, *88* (1), 232–234. https://doi.org/https://doi.org/10.1111/j.1551-2916.2004.00034.x.

(18) Widgeon, S.; Mera, G.; Gao, Y.; Sen, S.; Navrotsky, A.; Riedel, R. Effect of Precursor on Speciation and Nanostructure of SiBCN Polymer-Derived Ceramics. *Journal of the American Ceramic Society* 2013, *96* (5), 1651–1659. https://doi.org/https://doi.org/10.1111/jace.12192.

(19) Wu, C.; Pan, X.; Lin, F.; Cui, Z.; Li, X.; Chen, G.; Liu, X.; He, Y.; He, G.; Hai, Z.; Chen, Q.; Sun, D. High-Temperature Electrical Properties of Polymer-Derived Ceramic SiBCN Thin Films Fabricated by Direct Writing. *Ceramics International* 2022, *48* (11), 15293–15302. https://doi.org/https://doi.org/10.1016/j.ceramint.2022.02.063.

(20) Chelliah, N. M.; Singh, H.; Raj, R.; Surappa, M. K. Processing, Microstructural Evolution and Strength Properties of in-Situ Magnesium Matrix Composites Containing Nano-Sized Polymer Derived SiCNO Particles. *Materials Science and Engineering: A* 2017, *685*, 429–438. https://doi.org/https://doi.org/10.1016/j.msea.2017.01.001.

(21) Duan, R.-G.; Mukherjee, A. K. Synthesis of SiCNO Nanowires Through Heat-Treatment of Polymer-Functionalized Single-Walled Carbon Nanotubes. *Advanced Materials* 2004, *16* (13), 1106–1109. https://doi.org/https://doi.org/10.1002/adma.200306564.

(22) Schiavon, M. A.; Armelin, N. A.; Yoshida, I. V. P. Novel Poly(Borosiloxane) Precursors to Amorphous SiBCO Ceramics. *Materials Chemistry and Physics* 2008, *112* (3), 1047–1054. https://doi.org/https://doi.org/10.1016/j.matchemphys.2008.07.041.

(23) Liebau, V.; Hauser, R.; Riedel, R. Amorphous SiBCO Ceramics Derived from Novel Polymeric Precursors. *Comptes Rendus Chimie* 2004, *7* (5), 463–469. https://doi.org/https://doi.org/10.1016/j.crci.2003.11.012.

(24) Terauds, K.; Raj, R.; Kroll, P. Ab Inito and FTIR Studies of HfSiCNO Processed from the Polymer Route. *Journal of the American Ceramic Society* 2014, *97* (3), 742–749. https://doi.org/https://doi.org/10.1111/jace.12779.

(25) Ionescu, E.; Kleebe, H.-J.; Riedel, R. Silicon-Containing Polymer-Derived Ceramic Nanocomposites (PDC-NCs): Preparative Approaches and Properties. *Chemical Society Reviews* 2012, *41* (15), 5032–5052.

(26) Yu, Z.; Yang, L.; Min, H.; Zhang, P.; Zhou, C.; Riedel, R. Single-Source-Precursor Synthesis of High Temperature Stable SiC/C/Fe Nanocomposites from a Processable Hyperbranched Polyferrocenylcarbosilane with High Ceramic Yield. *Journal of Materials Chemistry C* 2014, *2* (6), 1057–1067.

(27) Eckel, Z. C.; Zhou, C.; Martin, J. H.; Jacobsen, A. J.; Carter, W. B.; Schaedler, T. A. Additive Manufacturing of Polymer-Derived Ceramics. *Science (1979)* 2016, *351* (6268), 58–62.

(28) Kumar, B. V. M.; Kim, Y.-W. Processing of Polysiloxane-Derived Porous Ceramics: A Review. *Sci Technol Adv Mater* 2010.

(29) Takahashi, T.; Colombo, P. SiOC Ceramic Foams through Melt Foaming of a Methylsilicone Preceramic Polymer. *Journal of Porous Materials* 2003, *10* (2), 113–121.

(30) Takahashi, T.; Münstedt, H.; Colombo, P.; Modesti, M. Thermal Evolution of a Silicone Resin/Polyurethane Blend from Preceramic to Ceramic Foam. *J Mater Sci* 2001, *36* (7), 1627–1639.

(31) Eom, J.-H.; Kim, Y.-W.; Park, C. B.; Wang, C. Effect of Forming Methods on Porosity and Compressive Strength of Polysiloxane-Derived Porous Silicon Carbide Ceramics. *Journal of the Ceramic Society of Japan* 2012, *120* (1401), 199–203.

(32) Guo, A.; Roso, M.; Modesti, M.; Liu, J.; Colombo, P. Preceramic Polymer-Derived SiOC Fibers by Electrospinning. *Journal of Applied Polymer Science* 2014, *131* (3). https://doi.org/https://doi.org/10.1002/app.39836.

(33) Wolff, F.; Ceron Nicolat, B.; Fey, T.; Greil, P.; Münstedt, H. Extrusion Foaming of a Preceramic Silicone Resin with a Variety of Profiles and Morphologies. *Advanced Engineering Materials* 2012, *14* (12), 1110–1115. https://doi.org/10.1002/adem.201100351.

(34) Young-Wook, K. I. M.; Kyoung-Ho, L. E. E.; Sung-Hee, L. E. E.; Chul B, P. Fabrication of Porous Silicon Oxycarbide Ceramics by Foaming Polymer Liquid and Compression Molding. *Journal of the Ceramic Society of Japan* 2003, *111* (1299), 863–864.

(35) Barroso, G. *Thermal Barrier Coating by Polymer-Derived Ceramic Technique for Application in Exhaust Systems*; Cuvillier Verlag, 2018; Vol. 12.

(36) Dibandjo, P.; Dirè, S.; Babonneau, F.; Soraru, G. D. New Insights into the Nanostructure of High-C SiOC Glasses Obtained via Polymer Pyrolysis. *Glass Technology-European Journal of Glass Science and Technology Part A* 2008, *49* (4), 175–178.

(37) Kleebe, H.-J.; Blum, Y. D. SiOC Ceramic with High Excess Free Carbon. *J Eur Ceram Soc* 2008, *28* (5), 1037–1042.

(38) Mera, G.; Riedel, R.; Poli, F.; Müller, K. Carbon-Rich SiCN Ceramics Derived from Phenyl-Containing Poly (Silylcarbodiimides). *J Eur Ceram Soc* 2009, *29* (13), 2873–2883.

(39) Blum, Y. D.; MacQueen, D. B.; Kleebe, H.-J. Synthesis and Characterization of Carbon-Enriched Silicon Oxycarbides. *J Eur Ceram Soc* 2005, *25* (2), 143–149. https://doi.org/https://doi.org/10.1016/j.jeurceramsoc.2004.07.019.

(40) Riedel, R.; Toma, L.; Janssen, E.; Nuffer, J.; Melz, T.; Hanselka, H. Piezoresistive Effect in SiOC Ceramics for Integrated Pressure Sensors. *Journal of the American Ceramic Society* 2010, *93* (4), 920–924. https://doi.org/https://doi.org/10.1111/j.1551-2916.2009.03496.x.

(41) Sorarù, G. D.; Modena, S.; Guadagnino, E.; Colombo, P.; Egan, J.; Pantano, C. Chemical Durability of Silicon Oxycarbide Glasses. *Journal of the American Ceramic Society* 2002, *85* (6), 1529–1536.

(42) Kim, K. J.; Eom, J.-H.; Kim, Y.-W.; Seo, W.-S. Electrical Conductivity of Dense, Bulk Silicon-Oxycarbide Ceramics. *J Eur Ceram Soc* 2015, *35* (5), 1355–1360. https://doi.org/https://doi.org/10.1016/j.jeurceramsoc.2014.12.007.

(43) Trassl, S.; Puchinger, M.; Rössler, E.; Ziegler, G. Electrical Properties of Amorphous SiCxNyHz-Ceramics Derived from Polyvinylsilazane. *J Eur Ceram Soc* 2003, *23* (5), 781–789. https://doi.org/https://doi.org/10.1016/S0955-2219(02)00155-3.

(44) Ionescu, E.; Balan, C.; Kleebe, H.; Müller, M. M.; Guillon, O.; Schliephake, D.; Heilmaier, M.; Riedel, R. High-temperature Creep Behavior of SiOC

Glass-ceramics: Influence of Network Carbon versus Segregated Carbon. *Journal of the American Ceramic Society* 2014, *97* (12), 3935–3942.

(45) Mera, G.; Ionescu, E. Silicon-containing Preceramic Polymers. *Encyclopedia of polymer science and technology* 2002.

(46) Günthner, M.; Wang, K.; Bordia, R. K.; Motz, G. Conversion Behaviour and Resulting Mechanical Properties of Polysilazane-Based Coatings. *J Eur Ceram Soc* 2012, *32* (9), 1883–1892.

(47) Barroso, G.; Li, Q.; Bordia, R. K.; Motz, G. Polymeric and Ceramic Silicon-Based Coatings–a Review. *Journal of materials chemistry A* 2019, *7* (5), 1936–1963.

(48) Flores, O.; Bordia, R. K.; Nestler, D.; Krenkel, W.; Motz, G. Ceramic Fibers Based on SiC and SiCN Systems: Current Research, Development, and Commercial Status. *Advanced Engineering Materials* 2014, *16* (6), 621–636.

(49) Eckel, Z. C.; Zhou, C.; Martin, J. H.; Jacobsen, A. J.; Carter, W. B.; Schaedler, T. A. Additive Manufacturing of Polymer-Derived Ceramics. *Science (1979)* 2016, *351* (6268), 58–62. https://doi.org/doi:10.1126/science.aad2688.

(50) Su, D.; Li, Y.-L.; An, H.-J.; Liu, X.; Hou, F.; Li, J.-Y.; Fu, X. Pyrolytic Transformation of Liquid Precursors to Shaped Bulk Ceramics. *J Eur Ceram Soc* 2010, *30* (6), 1503–1511.

(51) He, W.; Chen, L.; Peng, F. Coating Formed by SiBCN Single Source Precursor via UV-Photopolymerization. *Materials Letters* 2017, *206*, 121–123.

(52) Liu, X.; Li, Y.-L.; Hou, F. Fabrication of SiOC Ceramic Microparts and Patterned Structures from Polysiloxanes via Liquid Cast and Pyrolysis. *Journal of the American Ceramic Society* 2009, *92* (1), 49–53. https://doi.org/10.1111/j.1551-2916.2008.02849.x.

(53) Hourlier, D.; Venkatachalam, S.; Ammar, M.-R.; Blum, Y. Pyrolytic Conversion of Organopolysiloxanes. *Journal of Analytical and Applied Pyrolysis* 2017, *123*, 296–306. https://doi.org/https://doi.org/10.1016/j.jaap.2016.11.016.

(54) Kleebe, H. J.; Gregori, G.; Babonneau, F.; Blum, R.; MacQueen, D. B.; Masse, S. Evolution of C-Rich SiOC Ceramics. Part I. Characterization by Integral

Spectroscopic Techniques: Electron Energy-Loss Spectroscopy, High Resolution TEM and Energy-Filtered TEM. *International journal of materials research* 2006, *97*, 710–720.

(55) Choong Kwet Yive, N. S.; Corriu, R. J. P.; Leclercq, D.; Mutin, P. H.; Vioux, A. Silicon Carbonitride from Polymeric Precursors: Thermal Cross-Linking and Pyrolysis of Oligosilazane Model Compounds. *Chemistry of Materials* 1992, *4* (1), 141–146. https://doi.org/10.1021/cm00019a029.

(56) Qazzazie-Hauser, A.; Honnef, K.; Hanemann, T. Crosslinking Behavior of UV-Cured Polyorganosilazane as Polymer-Derived Ceramic Precursor in Ambient and Nitrogen Atmosphere. *Polymers* . 2021. https://doi.org/10.3390/polym13152424.

(57) Martínez-Crespiera, S.; Ionescu, E.; Kleebe, H.-J.; Riedel, R. Pressureless Synthesis of Fully Dense and Crack-Free SiOC Bulk Ceramics via Photo-Crosslinking and Pyrolysis of a Polysiloxane. *J Eur Ceram Soc* 2011, *31* (5), 913–919. https://doi.org/https://doi.org/10.1016/j.jeurceramsoc.2010.11.019.

(58) Greil, P. Polymer Derived Engineering Ceramics. *Adv Eng Mater* 2000, *2* (6), 339–348.

(59) Adam, M.; Vakifahmetoglu, C.; Colombo, P.; Wilhelm, M.; Grathwohl, G. Polysiloxane-Derived Ceramics Containing Nanowires with Catalytically Active Tips. *Journal of the American Ceramic Society* 2014, *97* (3), 959–966. https://doi.org/10.1111/jace.12708.

(60) Kleebe, H.-J.; Turquat, C.; Sorarù, G. D. Phase Separation in an SiCO Glass Studied by Transmission Electron Microscopy and Electron Energy-Loss Spectroscopy. *Journal of the American Ceramic Society* 2001, *84* (5), 1073–1080. https://doi.org/https://doi.org/10.1111/j.1151-2916.2001.tb00792.x.

(61) Trassl, S.; Kleebe, H.; Störmer, H.; Motz, G.; Rössler, E.; Ziegler, G. Characterization of the Free-Carbon Phase in Si-C-N Ceramics: Part II, Comparison of Different Polysilazane Precursors. *Journal of the American Ceramic Society* 2002, *85* (5), 1268–1274.

(62) Burns, G. T.; Angelotti, T. P.; Hanneman, L. F.; Chandra, G.; Moore, J. A. Alkyl- and Arylsilsesquiazanes: Effect of the R Group on Polymer Degradation and Ceramic Char Composition. *Journal of Materials Science* 1987, *22* (7), 2609–2614. https://doi.org/10.1007/BF01082152.

(63) Hurwitz, F. I.; Heimann, P.; Farmer, S. C.; Hembree, D. M. Characterization of the Pyrolytic Conversion of Polysilsesquioxanes to Silicon Oxycarbides. *Journal of Materials Science* 1993, *28* (24), 6622–6630.

(64) Mutin, P. H. Control of the Composition and Structure of Silicon Oxycarbide and Oxynitride Glasses Derived from Polysiloxane Precursors. *Journal of Sol-Gel Science and Technology* 1999, *14* (1), 27–38. https://doi.org/10.1023/A:1008769913083.

(65) Narisawa, M.; Funabiki, F.; Iwase, A.; Wakai, F.; Hosono, H. Effects of Atmospheric Composition on the Molecular Structure of Synthesized Silicon Oxycarbides. *Journal of the American Ceramic Society* 2015, *98* (10), 3373–3380. https://doi.org/10.1111/jace.13756.

(66) Vakifahmetoglu, C.; Zeydanli, D.; Colombo, P. Porous Polymer Derived Ceramics. *Materials Science and Engineering R: Reports* 2016, *106*, 1–30. https://doi.org/10.1016/j.mser.2016.05.001.

(67) Riedel, R.; Mera, G.; Hauser, R.; Klonczynski, A. Silicon-Based Polymer-Derived Ceramics: Synthesis Properties and Applications-a Review Dedicated to Prof. Dr. Fritz Aldinger on the Occasion of His 65th Birthday. *Journal of the Ceramic Society of Japan* 2006, *114* (1330), 425–444.

(68) Stabler, C.; Ionescu, E.; Graczyk-Zajac, M.; Gonzalo-Juan, I.; Riedel, R. Silicon Oxycarbide Glasses and Glass-Ceramics: “All-Rounder” Materials for Advanced Structural and Functional Applications. *Journal of the American Ceramic Society* 2018, *101* (11), 4817–4856. https://doi.org/10.1111/jace.15932.

(69) Saha, A.; Raj, R.; Williamson, D. L. A Model for the Nanodomains in Polymer-Derived SiCO. *Journal of the American Ceramic Society* 2006, *89* (7), 2188–2195. https://doi.org/https://doi.org/10.1111/j.1551-2916.2006.00920.x.

(70) Vakifahmetoglu, C.; Semerci, T.; Soraru, G. D. Closed Porosity Ceramics and Glasses. *Journal of the American Ceramic Society* 2020, *103* (5), 2941–2969.

(71) Studart, A. R.; Gonzenbach, U. T.; Tervoort, E.; Gauckler, L. J. Processing Routes to Macroporous Ceramics: A Review. *Journal of the American Ceramic Society* 2006, *89* (6), 1771–1789. https://doi.org/10.1111/j.1551-2916.2006.01044.x.

(72) Scheffler, M.; Colombo, P. *Cellular Ceramics: Structure, Manufacturing, Properties and Applications*; John Wiley & Sons, 2006.

(73) Colombo, P.; Biasetto, L.; Bernardo, E.; Costacurta, S.; Vakifahmetoglu, C.; Peña-Alonso, R.; Sorarù, G. D.; Pippel, E.; Woltersdorf, J. Hierarchical Porosity Ceramic Components from Preceramic Polymers. In *31st International Conference on Advanced Ceramics and Composites, Wiley, Daytona Beach, Florida*; 2007; pp 3–11.

(74) T., M. J.; G., D. P.; Logan, W.; J., G. L.; A., L. J. Architected Cellular Ceramics with Tailored Stiffness via Direct Foam Writing. *Proceedings of the National Academy of Sciences* 2017, *114* (8), 1832–1837. https://doi.org/10.1073/pnas.1616769114.

(75) Hadi, A.; Emadi, R.; Baghshahi, S.; Naghavi, S. H. Different Pore Size Alumina Foams and Study of Their Mechanical Properties. *Ceramics-Silikaty* 2015, *59* (1), 6–9.

(76) IUPAC. Compendium of Chemical Terminology. *the "Gold Book." Blackwell Scientific Publications Oxford* 1997.

(77) Hammel, E. C.; Ighodaro, O. L. R.; Okoli, O. I. Processing and Properties of Advanced Porous Ceramics: An Application Based Review. *Ceramics International* 2014, *40* (10, Part A), 15351–15370. https://doi.org/https://doi.org/10.1016/j.ceramint.2014.06.095.

(78) Sing, K. S. W.; Schüth, F.; Weitkamp, T. Handbook of Porous Solids. *Handb. Porous Solids* 2002, *3*, 1543–1591.

(79) Manoj Kumar, B. v; Kim, Y.-W. Processing of Polysiloxane-Derived Porous Ceramics: A Review. *Science and Technology of Advanced Materials* 2010, *11* (6), 69801. https://doi.org/10.1088/1468-6996/11/6/069801.

(80) Vakifahmetoglu, C. Zeolite Decorated Highly Porous Acicular Calcium Silicate Ceramics. *Ceramics International* 2014, *40* (8 PART A), 11925–11932. https://doi.org/10.1016/j.ceramint.2014.04.028.

(81) Colombo, P. Conventional and Novel Processing Methods for Cellular Ceramics. *Philosophical Transactions of the Royal Society A: Mathematical, Physical and Engineering Sciences* 2006, *364* (1838), 109–124. https://doi.org/10.1098/rsta.2005.1683.

(82) Biasetto, L.; Colombo, P.; Innocentini, M. D. M.; Mullens, S. Gas Permeability of Microcellular Ceramic Foams. *Industrial & Engineering Chemistry Research* 2007, *46* (10), 3366–3372. https://doi.org/10.1021/ie061335d.

(83) Biasetto, L.; Francis, A.; Palade, P.; Principi, G.; Colombo, P. Polymer-Derived Microcellular SiOC Foams with Magnetic Functionality. *Journal of Materials Science* 2008, *43* (12), 4119–4126. https://doi.org/10.1007/s10853-007-2224-3.

(84) Vakifahmetoglu, C.; Menapace, I.; Hirsch, A.; Biasetto, L.; Hauser, R.; Riedel, R.; Colombo, P. Highly Porous Macro- and Micro-Cellular Ceramics from a Polysilazane Precursor. *Ceramics International* 2009, *35* (8), 3281–3290. https://doi.org/https://doi.org/10.1016/j.ceramint.2009.05.022.

(85) Yan, J.; Hong, L. Y.; Wang, A. J.; Kim, D. P. Facile Synthesis of SiCN Ceramic Foam via Self-Sacrificial Template Method. *Solid State Phenomena* 2007, *124–126*, 727–730. https://doi.org/10.4028/www.scientific.net/SSP.124-126.727.

(86) Reschke, V.; Laskowsky, A.; Kappa, M.; Wang, K.; Bordia, R. K.; Scheffler, M. Polymer Derived Ceramic Foams with Additional Strut Porosity. *Épìtöanyag* 2011, No. 3/4, 57.

(87) Strachota, A.; Černý, M.; Chlup, Z.; Rodzeń, K.; Depa, K.; Halasová, M.; Šlouf, M.; Schweigstillová, J. Preparation of Finely Macroporous SiOC Foams with High Mechanical Properties and with Hierarchical Porosity via Pyrolysis of a

Siloxane/Epoxide Composite. *Ceramics International* 2015, *41* (7), 8402–8410. https://doi.org/https://doi.org/10.1016/j.ceramint.2015.03.037.

(88) Chlup, Z.; Černý, M.; Strachota, A.; Svítilová, J.; Halasová, M. Effect of Ageing at 1200°C in Oxidative Environment on the Mechanical Response of SiOC Foams. *Ceramics International* 2015, *41* (7), 9030–9034. https://doi.org/https://doi.org/10.1016/j.ceramint.2015.03.273.

(89) Colombo, P.; Modesti, M. Silicon Oxycarbide Foams from a Silicone Preceramic Polymer and Polyurethane. *J Solgel Sci Technol* 1999, *14* (1), 103–111.

(90) Colombo, P.; Griffoni, M.; Modesti, M. Ceramic Foams from a Preceramic Polymer and Polyurethanes: Preparation and Morphological Investigations. *J Solgel Sci Technol* 1998, *13* (1), 195–199.

(91) Yan, X.; Tsotsis, T. T.; Sahimi, M. Fabrication of High-Surface Area Nanoporous SiOC Materials Using Pre-Ceramic Polymer Blends and a Sacrificial Template. *Microporous and Mesoporous Materials* 2015, *210*, 77–85. https://doi.org/https://doi.org/10.1016/j.micromeso.2015.02.006.

(92) Yan, X.; Sahimi, M.; Tsotsis, T. T. Fabrication of High-Surface Area Nanoporous SiOC Ceramics Using Pre-Ceramic Polymer Precursors and a Sacrificial Template: Precursor Effects. *Microporous and Mesoporous Materials* 2017, *241*, 338–345. https://doi.org/https://doi.org/10.1016/j.micromeso.2016.12.027.

(93) Zeschky, J.; Höfner, T.; Arnold, C.; Weißmann, R.; Bahloul-Hourlier, D.; Scheffler, M.; Greil, P. Polysilsesquioxane Derived Ceramic Foams with Gradient Porosity. *Acta Materialia* 2005, *53* (4), 927–937. https://doi.org/https://doi.org/10.1016/j.actamat.2004.10.039.

(94) Li, Q.; Tsai, C.-C.; Scheffler, M.; Joshi, S.; Bordia, R. K. Macrostructural Design of Highly Porous SiOC Ceramic Foams by Preceramic Polymer Viscosity Tailoring. *Ceramics International* 2022, *48* (1), 224–231. https://doi.org/https://doi.org/10.1016/j.ceramint.2021.08.379.

(95) Tian, H.; Ma, Q. Effects of Heating Rate on the Structure and Properties of SiOC Ceramic Foams Derived from Silicone Resin. *Ceramics International* 2012, *38* (3), 2101–2104. https://doi.org/https://doi.org/10.1016/j.ceramint.2011.10.048.

(96) Tian, H.; Ma, Q. Effects of Exterior Gas Pressure on the Structure and Properties of Highly Porous SiOC Ceramics Derived from Silicone Resin. *Materials Letters* 2012, *66* (1), 13–15. https://doi.org/https://doi.org/10.1016/j.matlet.2011.08.051.

(97) Tian, H.; Ma, Q.; Pan, Y.; Liu, W. Effects of Inert Filler Addition on the Structure and Properties of Porous SiOC Ceramics Derived from Silicone Resin. *Ceramics International* 2012, *38* (6), 5039–5043. https://doi.org/https://doi.org/10.1016/j.ceramint.2012.03.005.

(98) Chen, H.; Parthasarathy, T. A.; Cinibulk, M. K.; Chen, M.-Y. Processing, Characterization, and Modeling of Room-Temperature-Vulcanized Silicone-Derived Ceramic Foams. *Journal of the American Ceramic Society* 2014, *97* (3), 733–741. https://doi.org/https://doi.org/10.1111/jace.12754.

(99) Idesaki, A.; Colombo, P. Synthesis of a Ni-Containing Porous SiOC Material From Polyphenylmethylsiloxane by a Direct Foaming Technique. *Advanced Engineering Materials* 2012, *14* (12), 1116–1122. https://doi.org/https://doi.org/10.1002/adem.201100354.

(100) Wolff, F.; Münstedt, H. Continuous Direct Melt Foaming of a Preceramic Polymer Using Carbon Dioxide: Extrusion Device and First Results. *Journal of Materials Science* 2011, *46* (18), 6162–6167. https://doi.org/10.1007/s10853-011-5679-1.

(101) Kim, Y.-W.; Kim, S.-H.; Wang, C.; Park, C. B. Fabrication of Microcellular Ceramics Using Gaseous Carbon Dioxide. *Journal of the American Ceramic Society* 2003, *86* (12), 2231–2233. https://doi.org/10.1111/j.1151-2916.2003.tb03641.x.

(102) Fukushima, M.; Colombo, P. Silicon Carbide-Based Foams from Direct Blowing of Polycarbosilane. *J Eur Ceram Soc* 2012, *32* (2), 503–510. https://doi.org/https://doi.org/10.1016/j.jeurceramsoc.2011.09.009.

(103) Naviroj, M.; Miller, S. M.; Colombo, P.; Faber, K. T. Directionally Aligned Macroporous SiOC via Freeze Casting of Preceramic Polymers. *J Eur Ceram Soc* 2015, *35* (8), 2225–2232. https://doi.org/https://doi.org/10.1016/j.jeurceramsoc.2015.02.013.

(104) Yoon, B.-H.; Lee, E.-J.; Kim, H.-E.; Koh, Y.-H. Highly Aligned Porous Silicon Carbide Ceramics by Freezing Polycarbosilane/Camphene Solution. *Journal of the American Ceramic Society* 2007, *90* (6), 1753–1759. https://doi.org/https://doi.org/10.1111/j.1551-2916.2007.01703.x.

(105) Schmidt, H.; Koch, D.; Grathwohl, G.; Colombo, P. Micro-/Macroporous Ceramics from Preceramic Precursors. *Journal of the American Ceramic Society* 2001, *84* (10), 2252–2255. https://doi.org/https://doi.org/10.1111/j.1151-2916.2001.tb00997.x.

(106) Wilhelm, M.; Soltmann, C.; Koch, D.; Grathwohl, G. Ceramers—Functional Materials for Adsorption Techniques. *J Eur Ceram Soc* 2005, *25* (2), 271–276. https://doi.org/https://doi.org/10.1016/j.jeurceramsoc.2004.08.008.

(107) Icin, O.; Vakifahmetoglu, C. Dye Removal by Polymer Derived Ceramic Nanobeads. *Ceramics International* 2021, *47* (19), 27050–27057. https://doi.org/https://doi.org/10.1016/j.ceramint.2021.06.118.

(108) Choudhary, A.; Pratihar, S. K.; Agrawal, A. K.; Behera, S. K. Macroporous SiOC Ceramics with Dense Struts by Positive Sponge Replication Technique. *Advanced Engineering Materials* 2018, *20* (3), 1700586.

(109) Schwartzwalder, K.; Somers, H.; Somers, A. v. U. S. Pat. No. 3090094, 1963.

(110) Santhosh, B.; Vakifahmetoglu, C.; Ionescu, E.; Reitz, A.; Albert, B.; Soraru, G. D. Processing and Thermal Characterization of Polymer Derived SiCN (O) and SiOC Reticulated Foams. *Ceramics International* 2020, *46* (5), 5594–5601.

(111) Soraru, G. D.; Campostrini, R.; Ejigu, A. A.; Zera, E.; Jana, P. Processing and Characterization of Polymer Derived SiOC Foam with Hierarchical Porosity by HF Etching. *Journal of the Ceramic Society of Japan* 2016, *124* (10), 1023–1029. https://doi.org/10.2109/jcersj2.16072.

(112) Ceron-Nicolat, B.; Fey, T.; Greil, P. Processing of Ceramic Foams with Hierarchical Cell Structure. *Advanced Engineering Materials* 2010, *12* (9), 884–892. https://doi.org/https://doi.org/10.1002/adem.201000114.

(113) Pan, J.; Yan, X.; Cheng, X.; Lu, Q.; Wang, M.; Zhang, C. Preparation of SiC Nanowires-Filled Cellular SiCO Ceramics from Polymeric Precursor. *Ceramics International* 2012, *38* (8), 6823–6829. https://doi.org/https://doi.org/10.1016/j.ceramint.2012.05.081.

(114) Jana, P.; Bruzzoniti, M. C.; Appendini, M.; Rivoira, L.; del Bubba, M.; Rossini, D.; Ciofi, L.; Sorarù, G. D. Processing of Polymer-Derived Silicon Carbide Foams and Their Adsorption Capacity for Non-Steroidal Anti-Inflammatory Drugs. *Ceramics International* 2016, *42* (16), 18937–18943. https://doi.org/10.1016/j.ceramint.2016.09.045.

(115) Schelm, K.; Morales, E. A.; Scheffler, M. Mechanical and Surface-Chemical Properties of Polymer Derived Ceramic Replica Foams. *Materials* 2019, *12* (11). https://doi.org/10.3390/ma12111870.

(116) Jana, P.; Zera, E.; Sorarù, G. D. Processing of Preceramic Polymer to Low Density Silicon Carbide Foam. *Materials and Design* 2017, *116*, 278–286. https://doi.org/10.1016/j.matdes.2016.12.010.

(117) Choudhary, A.; Pratihar, S. K.; Behera, S. K. Hierarchically Porous Biomorphic Polymer Derived C–SiOC Ceramics. *RSC Advances* 2016, *6* (98), 95897–95902. https://doi.org/10.1039/C6RA21206A.

(118) Yuan, X.; Jin, H.; Yan, X.; Cheng, L.; Hu, L.; Xue, Q. Synthesis of Ordered Mesoporous Silicon Oxycarbide Monoliths via Preceramic Polymer Nanocasting. *Microporous and Mesoporous Materials* 2012, *147* (1), 252–258. https://doi.org/https://doi.org/10.1016/j.micromeso.2011.06.025.

(119) Painuly, A.; P.P., S.; George, B. K.; K., P. Preparation of Cellular SiBOC Foams by Precipitating Methylvinylborosiloxane Oligomers within Melamine Formaldehyde Foam Scaffold. *J Eur Ceram Soc* 2021, *41* (1), 290–299. https://doi.org/https://doi.org/10.1016/j.jeurceramsoc.2020.09.013.

(120) Essmeister, J.; Altun, A. A.; Staudacher, M.; Lube, T.; Schwentenwein, M.; Konegger, T. Stereolithography-Based Additive Manufacturing of Polymer-Derived SiOC/SiC Ceramic Composites. *J Eur Ceram Soc* 2022. https://doi.org/https://doi.org/10.1016/j.jeurceramsoc.2022.06.021.

(121) Pelanconi, M.; Colombo, P.; Ortona, A. Additive Manufacturing of Silicon Carbide by Selective Laser Sintering of PA12 Powders and Polymer Infiltration and Pyrolysis. *J Eur Ceram Soc* 2021, *41* (10), 5056–5065. https://doi.org/https://doi.org/10.1016/j.jeurceramsoc.2021.04.014.

(122) Fu, Z.; Schlier, L.; Travitzky, N.; Greil, P. Three-Dimensional Printing of SiSiC Lattice Truss Structures. *Materials Science and Engineering: A* 2013, *560*, 851–856. https://doi.org/https://doi.org/10.1016/j.msea.2012.09.107.

(123) Franchin, G.; Wahl, L.; Colombo, P. Direct Ink Writing of Ceramic Matrix Composite Structures. *Journal of the American Ceramic Society* 2017, *100* (10), 4397–4401. https://doi.org/https://doi.org/10.1111/jace.15045.

(124) Brodnik, N. R.; Schmidt, J.; Colombo, P.; Faber, K. T. Analysis of Multi-Scale Mechanical Properties of Ceramic Trusses Prepared from Preceramic Polymers. *Additive Manufacturing* 2020, *31*, 100957.

(125) Li, S.; Zhang, Y.; Zhao, T.; Han, W.; Duan, W.; Wang, L.; Dou, R.; Wang, G. Additive Manufacturing of SiBCN/Si 3 N 4 w Composites from Preceramic Polymers by Digital Light Processing. *RSC Adv* 2020, *10* (10), 5681–5689.

(126) Pierin, G.; Grotta, C.; Colombo, P.; Mattevi, C. Direct Ink Writing of Micrometric SiOC Ceramic Structures Using a Preceramic Polymer. *J Eur Ceram Soc* 2016, *36* (7), 1589–1594. https://doi.org/https://doi.org/10.1016/j.jeurceramsoc.2016.01.047.

(127) Huang, K.; Elsayed, H.; Franchin, G.; Colombo, P. 3D Printing of Polymer-Derived SiOC with Hierarchical and Tunable Porosity. *Additive Manufacturing* 2020, *36*, 101549. https://doi.org/https://doi.org/10.1016/j.addma.2020.101549.

(128) Huang, K.; Elsayed, H.; Franchin, G.; Colombo, P. Additive Manufacturing of SiOC Scaffolds with Tunable Structure-Performance Relationship. *J Eur Ceram*

Soc 2021, *41* (15), 7552–7559. https://doi.org/https://doi.org/10.1016/j.jeurceramsoc.2021.08.043.

(129) Zanchetta, E.; Cattaldo, M.; Franchin, G.; Schwentenwein, M.; Homa, J.; Brusatin, G.; Colombo, P. Stereolithography of SiOC Ceramic Microcomponents. *Advanced Materials* 2016, *28* (2), 370–376.

(130) Zocca, A.; Gomes, C. M.; Staude, A.; Bernardo, E.; Günster, J.; Colombo, P. SiOC Ceramics with Ordered Porosity by 3D-Printing of a Preceramic Polymer. *Journal of Materials Research* 2013, *28* (17), 2243–2252.

(131) Kulkarni, A.; Sorarù, G. D.; Pearce, J. M. Polymer-Derived SiOC Replica of Material Extrusion-Based 3-D Printed Plastics. *Additive Manufacturing* 2020, *32*, 100988. https://doi.org/https://doi.org/10.1016/j.addma.2019.100988.

(132) Kulkarni, A.; Pearce, J.; Yang, Y.; Motta, A.; Sorarù, G. D. SiOC(N) Cellular Structures with Dense Struts by Integrating Fused Filament Fabrication 3D Printing with Polymer-Derived Ceramics. *Advanced Engineering Materials* 2021, *23* (12), 2100535. https://doi.org/https://doi.org/10.1002/adem.202100535.

(133) Yang, Y.; Kulkarni, A.; Soraru, G. D.; Pearce, J. M.; Motta, A. 3D Printed SiOC(N) Ceramic Scaffolds for Bone Tissue Regeneration: Improved Osteogenic Differentiation of Human Bone Marrow-Derived Mesenchymal Stem Cells. *International Journal of Molecular Sciences* 2021, *22* (24), 13676.

(134) Xiao, J.; Liu, D.; Cheng, H.; Jia, Y.; Zhou, S.; Zu, M. Carbon Nanotubes as Light Absorbers in Digital Light Processing Three-Dimensional Printing of SiCN Ceramics from Preceramic Polysilazane. *Ceramics International* 2020, *46* (11, Part B), 19393–19400. https://doi.org/https://doi.org/10.1016/j.ceramint.2020.04.282.

(135) Xiao, J.; Jia, Y.; Liu, D.; Cheng, H. Three-Dimensional Printing of SiCN Ceramic Matrix Composites from Preceramic Polysilazane by Digital Light Processing. *Ceramics International* 2020, *46* (16, Part A), 25802–25807. https://doi.org/https://doi.org/10.1016/j.ceramint.2020.07.061.

(136) Jana, P.; Santoliquido, O.; Ortona, A.; Colombo, P.; Sorarù, G. D. Polymer-derived SiCN Cellular Structures from Replica of 3D Printed Lattices. *Journal of the American Ceramic Society* 2018, *101* (7), 2732–2738.

(137) Kistler, S. S. Coherent Expanded Aerogels and Jellies. *Nature* 1931, *127* (3211), 741.

(138) Hou, X.; Zhang, R.; Fang, D. Novel Whisker-Reinforced Al2O3–SiO2 Aerogel Composites with Ultra-Low Thermal Conductivity. *Ceramics International* 2017, *43* (12), 9547–9551.

(139) Bancheri, J.; Seuntjens, J.; Sarfehnia, A.; Renaud, J. Density Effects of Silica Aerogel Insulation on the Performance of a Graphite Probe Calorimeter. *Medical Physics* 2019, *46* (4), 1874–1882. https://doi.org/10.1002/mp.13426.

(140) Qiu, Z.; Zhang, T.; Yue, X.; Fang, Y.; Yang, D.; Qiu, F. 3D Hierarchical MnO2 Aerogels with Superhydrophobicity for Selective Oil–Water Separation. *Applied Organometallic Chemistry* 2019, *33* (9), e5073.

(141) Jiao, C.; Li, T.; Wang, J.; Wang, H.; Zhang, X.; Han, X.; Du, Z.; Shang, Y.; Chen, Y. Efficient Removal of Dyes from Aqueous Solution by a Porous Sodium Alginate/Gelatin/Graphene Oxide Triple-Network Composite Aerogel. *Journal of Polymers and the Environment* 2020, *28* (5), 1492–1502. https://doi.org/10.1007/s10924-020-01702-1.

(142) Mao, J.; Iocozzia, J.; Huang, J.; Meng, K.; Lai, Y.; Lin, Z. Graphene Aerogels for Efficient Energy Storage and Conversion. *Energy and Environmental Science* 2018, *11* (4), 772–799. https://doi.org/10.1039/c7ee03031b.

(143) Juanjuan, Z.; Ruiyi, L.; Zaijun, L.; Junkang, L.; Zhiguo, G.; Guangli, W. Synthesis of Nitrogen-Doped Activated Graphene Aerogel/Gold Nanoparticles and Its Application for Electrochemical Detection of Hydroquinone and o-Dihydroxybenzene. *Nanoscale* 2014, *6* (10), 5458–5466.

(144) Sun, X. Y.; Luo, W. B.; Meng, J.; Qing, X.; Fu, W. Y.; Shuai, Y.; Wu, C. G. Monolithic Pyroelectric Infrared Detectors Using SiO2 Aerogel Thin Films. *Sensors and Actuators, A: Physical* 2015, *228*, 69–74. https://doi.org/10.1016/j.sna.2015.03.006.

(145) Shao, G.; Ovsianytskyi, O.; Bekheet, M. F.; Gurlo, A. On-Chip Assembly of 3D Graphene-Based Aerogels for Chemiresistive Gas Sensing. *Chemical Communications* 2020, *56* (3), 450–453. https://doi.org/10.1039/c9cc09092d.

(146) Zhuo, H.; Hu, Y.; Chen, Z.; Peng, X.; Liu, L.; Luo, Q.; Yi, J.; Liu, C.; Zhong, L. A Carbon Aerogel with Super Mechanical and Sensing Performances for Wearable Piezoresistive Sensors. *Journal of Materials Chemistry A* 2019, *7* (14), 8092–8100.

(147) Li, M.; Qin, Z.; Cui, Y.; Yang, C.; Deng, C.; Wang, Y.; Kang, J. S.; Xia, H.; Hu, Y. Ultralight and Flexible Monolithic Polymer Aerogel with Extraordinary Thermal Insulation by A Facile Ambient Process. *Advanced Materials Interfaces* 2019, *6* (13). https://doi.org/10.1002/admi.201900314.

(148) Zhao, X.; Yang, F.; Wang, Z.; Ma, P.; Dong, W.; Hou, H.; Fan, W.; Liu, T. Mechanically Strong and Thermally Insulating Polyimide Aerogels by Homogeneity Reinforcement of Electrospun Nanofibers. *Composites Part B: Engineering* 2020, *182*. https://doi.org/10.1016/j.compositesb.2019.107624.

(149) Fan, W.; Zhang, X.; Zhang, Y.; Zhang, Y.; Liu, T. Lightweight, Strong, and Super-Thermal Insulating Polyimide Composite Aerogels under High Temperature. *Composites Science and Technology* 2019, *173*, 47–52. https://doi.org/10.1016/j.compscitech.2019.01.025.

(150) Ghaffari Mosanenzadeh, S.; Alshrah, M.; Saadatnia, Z.; Park, C. B.; Naguib, H. E. Double Dianhydride Backbone Polyimide Aerogels with Enhanced Thermal Insulation for High-Temperature Applications. *Macromolecular Materials and Engineering* 2020, *305* (4). https://doi.org/10.1002/mame.201900777.

(151) Zhang, J.; Kong, Y.; Shen, X. Polyvinylidene Fluoride Aerogel with High Thermal Stability and Low Thermal Conductivity. *Materials Letters* 2020, *259*. https://doi.org/10.1016/j.matlet.2019.126890.

(152) Li, K.; Wang, K.; Zhang, Y.; Liu, H.; Wang, J. A Polyvinylidene Fluoride (PVDF)–Silica Aerogel (SiAG) Insulating Membrane for Improvement of Thermal Efficiency during Membrane Distillation. *Journal of Membrane Science* 2020, *597*. https://doi.org/10.1016/j.memsci.2019.117632.

(153) Luo, G.; Gu, X.; Zhang, J.; Zhang, R.; Shen, Q.; Li, M.; Zhang, L. Microstructural, Mechanical, and Thermal-Insulation Properties of Poly(Methyl Methacrylate)/Silica Aerogel Bimodal Cellular Foams. *Journal of Applied Polymer Science* 2017, *134* (6). https://doi.org/10.1002/app.44434.

(154) Ding, J.; Wu, X.; Shen, X.; Cui, S.; Zhong, Y.; An, C.; Cui, Y.; Chen, X. Synthesis and Textural Evolution of Mesoporous Si3N4 Aerogel with High Specific Surface Area and Excellent Thermal Insulation Property via the Urea Assisted Sol-Gel Technique. *Chemical Engineering Journal* 2020, *382*. https://doi.org/10.1016/j.cej.2019.122880.

(155) Kong, Y.; Zhang, J.; Zhao, Z.; Jiang, X.; Shen, X. Monolithic Silicon Nitride-Based Aerogels with Large Specific Surface Area and Low Thermal Conductivity. *Ceramics International* 2019, *45* (13), 16331–16337. https://doi.org/10.1016/j.ceramint.2019.05.160.

(156) An, Z.; Zhang, R.; Fang, D. Synthesis of Monolithic SiC Aerogels with High Mechanical Strength and Low Thermal Conductivity. *Ceramics International* 2019, *45* (9), 11368–11374. https://doi.org/10.1016/j.ceramint.2019.02.216.

(157) Yoon, S.; Han, G. D.; Jang, D. Y.; Kim, J. W.; Kim, D. H.; Shim, J. H. Fabrication of Yttria-Stabilized Zirconia Aerogel for High-Performance Thermal Barrier Coating. *Journal of Alloys and Compounds* 2019, *806*, 1430–1434. https://doi.org/10.1016/j.jallcom.2019.07.156.

(158) Xiang, X.; Qiangqiang, Z.; Menglong, H.; Yuan, H.; Zhaoyang, L.; Lele, P.; Tao, W.; Xuexin, R.; Chen, W.; Zipeng, Z.; Chengzhang, W.; Huilong, F.; Lei, W.; Jian, Z.; Hongtao, S.; Wenli, C.; Tao, D.; Biwei, D.; J., C. G.; Imran, S.; Chris, D.; S., F. T.; Xiang, Z.; Hui, L.; Yu, H.; Xiangfeng, D. Double-Negative-Index Ceramic Aerogels for Thermal Superinsulation. *Science (1979)* 2019, *363* (6428), 723–727. https://doi.org/10.1126/science.aav7304.

(159) IUPAC. Compendium of Chemical Terminology (the “Gold Book”) Compiled by A. D. McNaught and A. Wilkonsonitle. *Blackwell Scientic Publicaitons: Oxford.*

(160) Beckman, E. J. Supercritical and Near-Critical CO2 in Green Chemical Synthesis and Processing. *Journal of Supercritical Fluids* 2004, *28* (2–3), 121–191. https://doi.org/10.1016/S0896-8446(03)00029-9.

(161) Werner, B. G.; Hotchkiss, J. H. Continuous Flow Nonthermal CO2 Processing: The Lethal Effects of Subcritical and Supercritical CO2 on Total Microbial Populations and Bacterial Spores in Raw Milk. *Journal of Dairy Science* 2006, *89* (3), 872–881.

(162) Vakifahmetoglu, C.; Semerci, T.; Gurlo, A.; Soraru, G. D. Polymer Derived Ceramic Aerogels. *Current Opinion in Solid State and Materials Science* 2021, *25* (4), 100936. https://doi.org/10.1016/j.cossms.2021.100936.

(163) Chi, F. K. Carbon-Containing Monolithic Glasses via the Sol-Gel Process. In *7th Annual Conference on Composites and Advanced Ceramic Materials: Ceramic Engineering and Science Proceedings*; 2009; Vol. 4, pp 704–717.

(164) Singh, A. K.; Pantano, C. G. The Role of Si-H Functionality in Oxycarbide Glass Synthesis. *MRS Online Proceedings Library* 1992, *271* (1), 795–800. https://doi.org/10.1557/PROC-271-795.

(165) Babonneau, F.; Bois, L.; Livage, J. Silicon Oxycarbides via Sol-Gel Route: Characterization of the Pyrolysis Process. *Journal of Non-Crystalline Solids* 1992, *147–148*, 280–284. https://doi.org/https://doi.org/10.1016/S0022-3093(05)80630-1.

(166) Zhang, H.; Pantano, C. G. Synthesis and Characterization of Silicon Oxycarbide Glasses. *Journal of the American Ceramic Society* 1990, *73* (4), 958–963. https://doi.org/https://doi.org/10.1111/j.1151-2916.1990.tb05143.x.

(167) Aravind, P. R.; Soraru, G. D. Porous Silicon Oxycarbide Glasses from Hybrid Ambigels. *Microporous and Mesoporous Materials* 2011, *142* (2), 511–517. https://doi.org/https://doi.org/10.1016/j.micromeso.2010.12.033.

(168) Karakuscu, A.; Ponzoni, A.; Aravind, P. R.; Sberveglieri, G.; Soraru, G. D. Gas Sensing Behavior of Mesoporous SiOC Glasses. *Journal of the American Ceramic Society* 2013, *96* (8), 2366–2369. https://doi.org/10.1111/jace.12491.

(169) Dirè, S.; Borovin, E.; Narisawa, M.; Sorarù, G. D. Synthesis and Characterization of the First Transparent Silicon Oxycarbide Aerogel Obtained through H2 Decarbonization. *Journal of Materials Chemistry A* 2015, *3* (48), 24405–24413. https://doi.org/10.1039/c5ta06669g.

(170) Ma, J.; Ye, F.; Lin, S.; Zhang, B.; Yang, H.; Ding, J.; Yang, C.; Liu, Q. Large Size and Low Density SiOC Aerogel Monolith Prepared from Triethoxyvinylsilane/Tetraethoxysilane. *Ceramics International* 2017, *43* (7), 5774–5780.

(171) Wu, Z.; Cheng, X.; Zhang, L.; Li, J.; Yang, C. Sol-Gel Synthesis of Preceramic Polyphenylsilsesquioxane Aerogels and Their Application toward Monolithic Porous SiOC Ceramics. *Ceramics International* 2018, *44* (12), 14947–14951. https://doi.org/10.1016/j.ceramint.2018.05.115.

(172) Feng, J.; Feng, J.; Xiao, Y.; Jiang, Y. Synthesis, Structure, and Properties of Silicon Oxycarbide Aerogels Derived from Tetraethylortosilicate /Polydimethylsiloxane. *Ceramics International* 2015, *41* (4), 5281–5286. https://doi.org/10.1016/j.ceramint.2014.11.111.

(173) Yang, H.; Li, C.; Yue, X.; Huo, J.; Ye, F.; Liu, J.; Shi, F.; Ma, J. New BN/SiOC Aerogel Composites Fabricated by the Sol-Gel Method with Excellent Thermal Insulation Performance at High Temperature. *Materials and Design* 2020, *185*. https://doi.org/10.1016/j.matdes.2019.108217.

(174) Li, X.; Feng, J.; Yin, J.; Jiang, Y.; Feng, J. Preparation and Properties of SiBCO Aerogel and Its Composites. *Nanomaterials* 2018, *9* (1), 40.

(175) Chai, S.; Dai, X.; Wu, T.; Liu, B.; Yao, H.; Yuan, Y.; Wu, Q. Synthesis of Si/O/C/N Quaternary Composite Aerogels with Micro/Mesoporous Structures and Their Selective Adsorption Property for Volatile Carbonyl Compounds in Cigarette Smoke. *Microporous and Mesoporous Materials* 2020, *301*. https://doi.org/10.1016/j.micromeso.2020.110164.

(176) Weinberger, M.; Puchegger, S.; Fröschl, T.; Babonneau, F.; Peterlik, H.; Hüsing, N. Sol-Gel Processing of a Glycolated Cyclic Organosilane and Its Pyrolysis to Silicon Oxycarbide Monoliths with Multiscale Porosity and Large Surface Areas. *Chemistry of Materials* 2010, *22* (4), 1509–1520. https://doi.org/10.1021/cm903031d.

(177) Chen, K.; Bao, Z.; Du, A.; Zhu, X.; Wu, G.; Shen, J.; Zhou, B. Synthesis of Resorcinol–Formaldehyde/Silica Composite Aerogels and Their Low-

Temperature Conversion to Mesoporous Silicon Carbide. *Microporous and Mesoporous Materials* 2012, *149* (1), 16–24.

(178) Kong, Y.; Zhong, Y.; Shen, X.; Cui, S.; Yang, M.; Teng, K.; Zhang, J. Facile Synthesis of Resorcinol–Formaldehyde/Silica Composite Aerogels and Their Transformation to Monolithic Carbon/Silica and Carbon/Silicon Carbide Composite Aerogels. *J Non Cryst Solids* 2012, *358* (23), 3150–3155.

(179) Kong, Y.; Zhong, Y.; Shen, X.; Gu, L.; Cui, S.; Yang, M. Synthesis of Monolithic Mesoporous Silicon Carbide from Resorcinol–Formaldehyde/Silica Composites. *Materials Letters* 2013, *99*, 108–110.

(180) Hasegawa, G.; Kanamori, K.; Nakanishi, K.; Hanada, T. Fabrication of Macroporous Silicon Carbide Ceramics by Intramolecular Carbothermal Reduction of Phenyl-Bridged Polysilsesquioxane. *Journal of Materials Chemistry* 2009, *19* (41), 7716–7720.

(181) Hasegawa, G.; Kanamori, K.; Nakanishi, K.; Hanada, T. A New Route to Monolithic Macroporous SiC/C Composites from Biphenylene-Bridged Polysilsesquioxane Gels. *Chemistry of Materials* 2010, *22* (8), 2541–2547.

(182) Zirakjou, A.; Kokabi, M. SiC/C Aerogels from Biphenylene-Bridged Polysilsesquioxane/Clay Mineral Nanocomposite Aerogels. *Ceramics International* 2020, *46* (2), 2194–2205.

(183) Xie, M.; Wu, X.; Liu, J.; Zhang, K. In-Situ Synthesis and Textural Evolution of the Novel Carbonaceous SiC/Mullite Aerogel via Polymer-Derived Ceramics Route. *Ceramics International* 2017, *43* (13), 9896–9905.

(184) Seraji, M. M.; Ghafoorian, N. S.; Bahramian, A. R.; Alahbakhsh, A. Preparation and Characterization of C/SiO2/SiC Aerogels Based on Novolac/Silica Hybrid Hyperporous Materials. *Journal of Non-Crystalline Solids* 2015, *425*, 146–152.

(185) Seraji, M. M.; Ghafoorian, N. S.; Bahramian, A. R. Investigation of Microstructure and Mechanical Properties of Novolac/Silica and C/SiO2/SiC Aerogels Using Mercury Porosimetry Method. *Journal of Non-Crystalline Solids* 2016, *435*, 1–7.

(186) Wu, X.; Shao, G.; Shen, X.; Cui, S.; Chen, X. Evolution of the Novel C/SiO2/SiC Ternary Aerogel with High Specific Surface Area and Improved Oxidation Resistance. *Chemical Engineering Journal* 2017, *330*, 1022–1034.

(187) Pradeep, V. S.; Ayana, D. G.; Graczyk-Zajac, M.; Soraru, G. D.; Riedel, R. High Rate Capability of SiOC Ceramic Aerogels with Tailored Porosity as Anode Materials for Li-Ion Batteries. *Electrochimica Acta* 2015, *157*, 41–45. https://doi.org/https://doi.org/10.1016/j.electacta.2015.01.088.

(188) Zera, E.; Perolo, A.; Campostrini, R.; Li, W.; Sorarù, G. D. Synthesis and Characterization of Polymer-Derived SiCN Aerogel. *J Eur Ceram Soc* 2015, *35* (12), 3295–3302.

(189) Zera, E.; Campostrini, R.; Aravind, P. R.; Blum, Y.; Soraru, G. D. Novel SiC/C Aerogels through Pyrolysis of Polycarbosilane Precursors. *Advanced Engineering Materials* 2014, *16* (6), 814–819.

(190) Aguirre-Medel, S.; Jana, P.; Kroll, P.; Sorarù, G. D. Towards Porous Silicon Oxycarbide Materials: Effects of Solvents on Microstructural Features of Poly(Methylhydrosiloxane)/Divynilbenzene Aerogels. *Materials* 2018, *11* (12). https://doi.org/10.3390/ma11122589.

(191) Assefa, D.; Zera, E.; Campostrini, R.; Soraru, G. D.; Vakifahmetoglu, C. Polymer-Derived SiOC Aerogel with Hierarchical Porosity through HF Etching. *Ceramics International* 2016, *42* (10), 11805–11809. https://doi.org/https://doi.org/10.1016/j.ceramint.2016.04.101.

(192) Vallachira Warriam Sasikumar, P.; Zera, E.; Graczyk-Zajac, M.; Riedel, R.; Soraru, G. D. Structural Design of Polymer-Derived SiOC Ceramic Aerogels for High-Rate Li Ion Storage Applications. *Journal of the American Ceramic Society* 2016, *99* (9), 2977–2983. https://doi.org/https://doi.org/10.1111/jace.14323.

(193) Du, B.; Hong, C.; Wang, A.; Zhou, S.; Qu, Q.; Zhou, S.; Zhang, X. Preparation and Structural Evolution of SiOC Preceramic Aerogel during High-Temperature Treatment. *Ceramics International* 2018, *44* (1), 563–570. https://doi.org/10.1016/j.ceramint.2017.09.212.

(194) Bruzzoniti, M. C.; Appendini, M.; Rivoira, L.; Onida, B.; del Bubba, M.; Jana, P.; Sorarù, G. D. Polymer-Derived Ceramic Aerogels as Sorbent Materials for the Removal of Organic Dyes from Aqueous Solutions. *Journal of the American Ceramic Society* 2018, *101* (2), 821–830. https://doi.org/https://doi.org/10.1111/jace.15241.

(195) Zera, E.; Brancaccio, E.; Tognana, L.; Rivoira, L.; Bruzzoniti, M. C.; Sorarù, G. D. Reactive Atmosphere Synthesis of Polymer-Derived Si–O–C–N Aerogels and Their Cr Adsorption from Aqueous Solutions. *Advanced Engineering Materials* 2018, *20* (7). https://doi.org/10.1002/adem.201701130.

(196) Zhao, W.; Shao, G.; Han, S.; Cai, C.; Liu, X.; Sun, M.; Wang, H.; Li, X.; Zhang, R.; An, L. Facile Preparation of Ultralight Polymer-Derived SiOCN Ceramic Aerogels with Hierarchical Pore Structure. *Journal of the American Ceramic Society* 2019, *102* (5), 2316–2324. https://doi.org/https://doi.org/10.1111/jace.16100.

(197) Zera, E.; Nickel, W.; Hao, G. P.; Vanzetti, L.; Kaskel, S.; Sorarù, G. D. Nitrogen Doped Carbide Derived Carbon Aerogels by Chlorine Etching of a SiCN Aerogel. *Journal of Materials Chemistry A* 2016, *4* (12), 4525–4533. https://doi.org/10.1039/c6ta00589f.

(198) An, G.; Liu, H.; Li, H.; Chen, Z.; Li, J.; Li, Y. SiBCN Ceramic Aerogel/Graphene Composites Prepared via Sol-Gel Infiltration Process and Polymer-Derived Ceramics (PDCs) Route. *Ceramics International* 2020, *46* (6), 7001–7008.

(199) Liu, H.; An, G.; Li, H.; Chen, Z.; Li, J.; Li, Y. SiBCN-ZrO2 Hybrid Ceramic Aerogels through the Polymer-Derived Ceramics (PDCs) Route. *Ceramics International* 2018, *44* (18), 22991–22996.

(200) Zera, E.; Nickel, W.; Kaskel, S.; Sorarù, G. D. Out-of-Furnace Oxidation of SiCN Polymer-Derived Ceramic Aerogel Pyrolized at Intermediate Temperature (600-800°C). *J Eur Ceram Soc* 2016, *36* (3), 423–428. https://doi.org/10.1016/j.jeurceramsoc.2015.10.038.

(201) Zhao, W.; Shao, G.; Jiang, M.; Zhao, B.; Wang, H.; Chen, D.; Xu, H.; Li, X.; Zhang, R.; An, L. Ultralight Polymer-Derived Ceramic Aerogels with Wide

Bandwidth and Effective Electromagnetic Absorption Properties. *J Eur Ceram Soc* 2017, *37* (13), 3973–3980. https://doi.org/10.1016/j.jeurceramsoc.2017.04.068.

(202) Shao, G.; Liang, J.; Zhao, W.; Zhao, B.; Liu, W.; Wang, H.; Fan, B.; Xu, H.; Lu, H.; Wang, Y. Co Decorated Polymer-Derived SiCN Ceramic Aerogel Composites with Ultrabroad Microwave Absorption Performance. *Journal of Alloys and Compounds* 2020, *813*, 152007.

(203) Zambotti, A.; Biesuz, M.; Campostrini, R.; Carturan, S. M.; Speranza, G.; Ceccato, R.; Parrino, F.; Sorarù, G. D. Synthesis and Thermal Evolution of Polysilazane-Derived SiCN (O) Aerogels with Variable C Content Stable at 1600° C. *Ceramics International* 2021, *47* (6), 8035–8043.

(204) Xu, X.; Zhang, Q.; Hao, M.; Hu, Y.; Lin, Z.; Peng, L.; Wang, T.; Ren, X.; Wang, C.; Zhao, Z.; Huang, Y.; Duan, X. Double-Negative-Index Ceramic Aerogels for Thermal Superinsulation. *Science (1979)* 2019, *363* (6428), 723–727. https://doi.org/10.1126/science.aav7304.

(205) Chu, P.; Liu, H.; Li, Y.; Zhang, H.; Li, J. Synthesis of SiC-TiO2 Hybrid Aerogel via Supercritical Drying Combined PDCs Route. *Ceramics International* 2016, *42* (15), 17053–17058. https://doi.org/https://doi.org/10.1016/j.ceramint.2016.07.213.

(206) Vakifahmetoglu, C.; Zeydanli, D.; Innocentini, M. D. D. M.; Ribeiro, F. D. S.; Lasso, P. R. O.; Soraru, G. D. Gradient-Hierarchic-Aligned Porosity SiOC Ceramics. *Scientific Reports* 2017, *7*. https://doi.org/10.1038/srep41049.

(207) Zeydanli, D.; Akman, S.; Vakifahmetoglu, C. Polymer-Derived Ceramic Adsorbent for Pollutant Removal from Water. *Journal of the American Ceramic Society* 2018, *101* (6), 2258–2265. https://doi.org/https://doi.org/10.1111/jace.15423.

(208) Vakifahmetoglu, C.; Zeydanli, D.; Ozalp, V. C.; Borsa, B. A.; Soraru, G. D. Hierarchically Porous Polymer Derived Ceramics: A Promising Platform for Multidrug Delivery Systems. *Materials and Design* 2018, *140*, 37–44. https://doi.org/10.1016/j.matdes.2017.11.047.

(209) Vakifahmetoglu, C.; Buldu, M.; Karakuscu, A.; Ponzoni, A.; Assefa, D.; Soraru, G. D. High Surface Area Carbonous Components from Emulsion Derived SiOC and Their Gas Sensing Behavior. *J Eur Ceram Soc* 2015, *35* (16), 4447–4452. https://doi.org/https://doi.org/10.1016/j.jeurceramsoc.2015.08.030.

(210) Janakiraman, N.; Aldinger, F. Fabrication and Characterization of Fully Dense Si–C–N Ceramics from a Poly (Ureamethylvinyl) Silazane Precursor. *J Eur Ceram Soc* 2009, *29* (1), 163–173.

(211) Modena, S.; Sorarù, G. D.; Blum, Y.; Raj, R. Passive Oxidation of an Effluent System: The Case of Polymer-derived SiCO. *Journal of the American Ceramic Society* 2005, *88* (2), 339–345.

(212) Riedel, R.; Ruswisch, L. M.; An, L.; Raj, R. Amorphous Silicoboron Carbonitride Ceramic with Very High Viscosity at Temperatures above 1500 C. *Journal of the American Ceramic Society* 1998, *81* (12), 3341–3344.

(213) Vakifahmetoglu, C.; Colombo, P.; Carturan, S. M.; Pippel, E.; Woltersdorf, J. Growth of One-Dimensional Nanostructures in Porous Polymer-Derived Ceramics by Catalyst-Assisted Pyrolysis. Part II: Cobalt Catalyst. *Journal of the American Ceramic Society* 2010, *93* (11), 3709–3719. https://doi.org/10.1111/j.1551-2916.2010.03974.x.

(214) Vakifahmetoglu, C.; Pippel, E.; Woltersdorf, J.; Colombo, P. Growth of One-Dimensional Nanostructures in Porous Polymer-Derived Ceramics by Catalyst-Assisted Pyrolysis. Part I: Iron Catalyst. *Journal of the American Ceramic Society* 2010, *93* (4), 959–968. https://doi.org/10.1111/j.1551-2916.2009.03448.x.

(215) Lale, A.; Schmidt, M.; Mallmann, M. D.; Bezerra, A. V. A.; Acosta, E. D.; Machado, R. A. F.; Demirci, U. B.; Bernard, S. Polymer-Derived Ceramics with Engineered Mesoporosity: From Design to Application in Catalysis. *Surface and Coatings Technology* 2018, *350*, 569–586. https://doi.org/10.1016/j.surfcoat.2018.07.061.

(216) Kong, J.; Wang, M.; Zou, J.; An, L. Soluble and Meltable Hyperbranched Polyborosilazanes toward High-Temperature Stable SiBCN Ceramics. *ACS*

Applied Materials and Interfaces 2015, *7* (12), 6733–6744. https://doi.org/10.1021/am509129a.

(217) Patil, N.; Zhao, X.; Mishra, N. K.; Saed, M. A.; Radovic, M.; Green, M. J. Rapid Heating of Silicon Carbide Fibers under Radio Frequency Fields and Application in Curing Preceramic Polymer Composites. *ACS Applied Materials and Interfaces* 2019, *11* (49), 46132–46139. https://doi.org/10.1021/acsami.9b14971.

(218) Duong, B.; Gangopadhyay, P.; Brent, J.; Seraphin, S.; Loutfy, R. O.; Peyghambarian, N.; Thomas, J. Printed Sub-100 Nm Polymer-Derived Ceramic Structures. *ACS Applied Materials and Interfaces* 2013, *5* (9), 3894–3899. https://doi.org/10.1021/am400587z.

(219) Geissinger, A.; Oberle, J.; Teschner, W.; Boeder, H.; Heussner, K.-H. Ceramic Electric Resistor. Google Patents October 5, 1999.

(220) Gurlo, A.; Ionescu, E.; Riedel, R.; Clarke, D. R. The Thermal Conductivity of Polymer-Derived Amorphous Si–O–C Compounds and Nano-Composites. *Journal of the American Ceramic Society* 2016, *99* (1), 281–285.

(221) Kowbel, W.; Bruce, C. A.; Tsou, K. L.; Patel, K.; Withers, J. C.; Youngblood, G. E. High Thermal Conductivity SiC/SiC Composites for Fusion Applications. *Journal of Nuclear Materials* 2000, *283*, 570–573.

(222) Lube, T.; Dusza, J. A Silicon Nitride Reference Material—A Testing Program of ESIS TC6. *J Eur Ceram Soc* 2007, *27* (2–3), 1203–1209.

(223) Stabler, C.; Reitz, A.; Stein, P.; Albert, B.; Riedel, R.; Ionescu, E. Thermal Properties of SiOC Glasses and Glass Ceramics at Elevated Temperatures. *Materials* 2018, *11* (2). https://doi.org/10.3390/ma11020279.

(224) Kim, Y.-W.; Jin, Y.-J.; Eom, J.-H.; Song, I.-H.; Kim, H.-D. Engineering Porosity in Silicon Carbide Ceramics. *Journal of Materials Science* 2010, *45* (10), 2808–2815. https://doi.org/10.1007/s10853-010-4270-5.

(225) Carvalho, A. C.; Raupp-Pereira, F.; Rodrigues Neto, J. B.; Novaes De Oliveira, A. P. A New Source for Production of Ceramic Filters. *Materials Letters* 2015, *145*, 250–252. https://doi.org/10.1016/j.matlet.2015.01.131.

(226) Zhang, F.-Z.; Kato, T.; Fuji, M.; Takahashi, M. Gelcasting Fabrication of Porous Ceramics Using a Continuous Process. *J Eur Ceram Soc* 2006, *26* (4–5), 667–671. https://doi.org/10.1016/j.jeurceramsoc.2005.07.021.

(227) Wei, Z.; Li, S.; Li, Y.; Li, X.; Xiang, R.; Xu, N. Porous Alumina Ceramics with Enhanced Mechanical and Thermal Insulation Properties Based on Sol-Treated Rice Husk. *Ceramics International* 2018, *44* (18), 22616–22621. https://doi.org/10.1016/j.ceramint.2018.09.036.

(228) Shimizu, T.; Matsuura, K.; Furue, H.; Matsuzak, K. Thermal Conductivity of High Porosity Alumina Refractory Bricks Made by a Slurry Gelation and Foaming Method. *J Eur Ceram Soc* 2013, *33* (15–16), 3429–3435. https://doi.org/10.1016/j.jeurceramsoc.2013.07.001.

(229) Medri, V.; Mazzocchi, M.; Bellosi, A. ZrB2-Based Sponges and Lightweight Devices. *International Journal of Applied Ceramic Technology* 2011, *8* (4), 815–823. https://doi.org/10.1111/j.1744-7402.2010.02512.x.

(230) Papetti, V.; Dimopoulos Eggenschwiler, P.; della Torre, A.; Lucci, F.; Ortona, A.; Montenegro, G. Additive Manufactured Open Cell Polyhedral Structures as Substrates for Automotive Catalysts. *International Journal of Heat and Mass Transfer* 2018, *126*, 1035–1047. https://doi.org/10.1016/j.ijheatmasstransfer.2018.06.061.

(231) Innocentini, M. D. M.; Rodrigues, V. P.; Romano, R. C. O.; Pileggi, R. G.; Silva, G. M. C.; Coury, J. R. Permeability Optimization and Performance Evaluation of Hot Aerosol Filters Made Using Foam Incorporated Alumina Suspension. *Journal of Hazardous Materials* 2009, *162* (1), 212–221. https://doi.org/10.1016/j.jhazmat.2008.05.025.

(232) Colombo, P.; Vakifahmetoglu, C.; Costacurta, S. Fabrication of Ceramic Components with Hierarchical Porosity. *Journal of Materials Science* 2010, *45* (20), 5425–5455. https://doi.org/10.1007/s10853-010-4708-9.

(233) Duong-Viet, C.; Ba, H.; El-Berrichi, Z.; Nhut, J.-M.; Ledoux, M. J.; Liu, Y.; Pham-Huu, C. Silicon Carbide Foam as a Porous Support Platform for Catalytic Applications. *New Journal of Chemistry* 2016, *40* (5), 4285–4299. https://doi.org/10.1039/c5nj02847g.

(234) Patcas, F. C.; Garrido, G. I.; Kraushaar-Czarnetzki, B. CO Oxidation over Structured Carriers: A Comparison of Ceramic Foams, Honeycombs and Beads. *Chemical Engineering Science* 2007, *62* (15), 3984–3990. https://doi.org/10.1016/j.ces.2007.04.039.

(235) Santoliquido, O.; Bianchi, G.; Dimopoulos Eggenschwiler, P.; Ortona, A. Additive Manufacturing of Periodic Ceramic Substrates for Automotive Catalyst Supports. *International Journal of Applied Ceramic Technology* 2017, *14* (6), 1164–1173. https://doi.org/10.1111/ijac.12745.

(236) Taylor, J. A. Metal-Related Castability Effects in Aluminium Foundry Alloys. *Cast Metals* 1996, *8* (4), 225–252.

(237) Mbuya, T. O.; Odera, B. O.; Ng'ang'a, S. P. Influence of Iron on Castability and Properties of Aluminium Silicon Alloys: Literature Review. *International Journal of Cast Metals Research* 2003, *16* (5), 451–465. https://doi.org/10.1080/13640461.2003.11819622.

(238) Mansurov, Y. N.; Letyagin, N.; Finogeyev, A.; Rakhmonov, J. U. Influence of Impurity Elements on the Casting Properties of Al-Mg Based Alloys. *Non-Ferrous Metals* 2018, *44* (1), 24–29.

(239) Jorstad, J. L. Influence of Aluminum Casting Alloy Metallurgical Factors on Machinability. *SAE Transactions* 1980, 1892–1906.

(240) Vedula, V. R.; Green, D. J.; Hellman, J. R. Thermal Shock Resistance of Ceramic Foams. *Journal of the American Ceramic Society* 1999, *82* (3), 649–656.

(241) Green, D. J.; Colombo, P. Cellular Ceramics: Intriguing Structures, Novel Properties, and Innovative Applications. *MRS Bull* 2003, *28* (4), 296–300.

(242) Campbell, J. *Complete Casting Handbook: Metal Casting Processes, Metallurgy, Techniques and Design*; Butterworth-Heinemann, 2015.

(243) Sommers, A.; Wang, Q.; Han, X.; T'Joen, C.; Park, Y.; Jacobi, A. Ceramics and Ceramic Matrix Composites for Heat Exchangers in Advanced Thermal Systems—A Review. *Applied Thermal Engineering* 2010, *30* (11), 1277–1291. https://doi.org/https://doi.org/10.1016/j.applthermaleng.2010.02.018.

(244) Strumpf, H. J.; Stillwagon, T. L.; Kotchick, D. M.; Coombs, M. G. Advanced Industrial Ceramic Heat Pipe Recuperators. *Heat Recovery Systems and CHP* 1988, *8* (3), 235–246. https://doi.org/https://doi.org/10.1016/0890-4332(88)90059-2.

(245) Smyth, R. The Use of High Temperature Heat Exchangers to Increase Power Plant Thermal Efficiency. In *IECEC-97 Proceedings of the Thirty-Second Intersociety Energy Conversion Engineering Conference (Cat. No. 97CH6203)*; IEEE, 1997; Vol. 3, pp 1690–1695.

(246) Pelanconi, M.; Barbato, M.; Zavattoni, S.; Vignoles, G. L.; Ortona, A. Thermal Design, Optimization and Additive Manufacturing of Ceramic Regular Structures to Maximize the Radiative Heat Transfer. *Materials & Design* 2019, *163*, 107539. https://doi.org/https://doi.org/10.1016/j.matdes.2018.107539.

(247) Alm, B.; Knitter, R.; Haußelt, J. Development of a Ceramic Micro Heat Exchanger – Design, Construction, and Testing. *Chemical Engineering & Technology* 2005, *28* (12), 1554–1560. https://doi.org/https://doi.org/10.1002/ceat.200500253.

(248) Alm, B.; Imke, U.; Knitter, R.; Schygulla, U.; Zimmermann, S. Testing and Simulation of Ceramic Micro Heat Exchangers. *Chemical Engineering Journal* 2008, *135*, S179–S184. https://doi.org/https://doi.org/10.1016/j.cej.2007.07.005.

(249) Cramer, C. L.; Ionescu, E.; Graczyk-Zajac, M.; Nelson, A. T.; Katoh, Y.; Haslam, J. J.; Wondraczek, L.; Aguirre, T. G.; LeBlanc, S.; Wang, H.; Masoudi, M.; Tegeler, E.; Riedel, R.; Colombo, P.; Minary-Jolandan, M. Additive Manufacturing of Ceramic Materials for Energy Applications: Road Map and Opportunities. *J Eur Ceram Soc* 2022, *42* (7), 3049–3088. https://doi.org/https://doi.org/10.1016/j.jeurceramsoc.2022.01.058.

(250) Angelopoulou, P.; Vrettos, K.; Georgakilas, V.; Avgouropoulos, G. Graphene Aerogel Modified Carbon Paper as Anode for Lithium-Ion Batteries. *ChemistrySelect* 2020, *5* (9), 2719–2724. https://doi.org/https://doi.org/10.1002/slct.201904375.

(251) Wang, L.; Wei, G.; Dong, X.; Zhao, Y.; Xing, Z.; Hong, H.; Ju, Z. Hollow α-Fe2O3 Nanotubes Embedded in Graphene Aerogel as High-Performance Anode

Material for Lithium-Ion Batteries. *ChemistrySelect* 2019, *4* (38), 11370–11377. https://doi.org/https://doi.org/10.1002/slct.201902096.

(252) Butt, R.; Siddique, A. H.; Bokhari, S. W.; Jiang, S.; Lei, D.; Zhou, X.; Liu, Z. Niobium Carbide/Reduced Graphene Oxide Hybrid Porous Aerogel as High Capacity and Long-Life Anode Material for Li-Ion Batteries. *International Journal of Energy Research* 2019, *43* (9), 4995–5003. https://doi.org/https://doi.org/10.1002/er.4598.

(253) Shu, Y.; Li, X.; Ye, J.; Gao, W.; Cheng, S.; Zhang, X.; Ma, L.; Ding, Y. Improved Performance and Immobilizing Mechanism of N-Doping Carbon Aerogel with Net Channel via Long-Chain Directing for Lithium–Sulfur Battery. *Energy Technology* 2020, *8* (3), 1901057. https://doi.org/https://doi.org/10.1002/ente.201901057.

(254) Shi, M.; Yan, Y.; Wei, Y.; Zou, Y.; Deng, Q.; Wang, J.; Yang, R.; Xu, Y.; Han, T. Fabrication of Ultrafine Gd2O3 Nanoparticles/Carbon Aerogel Composite as Immobilization Host for Cathode for Lithium-Sulfur Batteries. *International Journal of Energy Research* 2019, *43* (13), 7614–7626. https://doi.org/https://doi.org/10.1002/er.4752.

(255) Zhang, X.; Li, X.; Gao, W.; Ma, L.; Fang, H.; Shu, Y.; Ye, J.; Ding, Y. Calixarene-Functionalized Porous Carbon Aerogels for Polysulfide Capture: Cathodes for High Performance Lithium-Sulfur Batteries. *Chempluschem* 2019, *84* (11), 1709–1715. https://doi.org/https://doi.org/10.1002/cplu.201900554.

(256) Ma, Y.; Wang, Q.; Liu, L.; Yao, S.; Wu, W.; Wang, Z.; Lv, P.; Zheng, J.; Yu, K.; Wei, W.; Ostrikov, K. K. Plasma-Enabled Ternary SnO2@Sn/Nitrogen-Doped Graphene Aerogel Anode for Sodium-Ion Batteries. *ChemElectroChem* 2020, *7* (6), 1358–1364. https://doi.org/https://doi.org/10.1002/celc.201901999.

(257) Hao, S.; Li, H.; Zhao, Z.; Wang, X. Pseudocapacitance-Enhanced Anode of CoP@C Particles Embedded in Graphene Aerogel toward Ultralong Cycling Stability Sodium-Ion Batteries. *ChemElectroChem* 2019, *6* (22), 5712–5720. https://doi.org/https://doi.org/10.1002/celc.201901549.

(258) Dibandjo, P.; Graczyk-Zajac, M.; Riedel, R.; Pradeep, V. S.; Soraru, G. D. Lithium Insertion into Dense and Porous Carbon-Rich Polymer-Derived SiOC

Ceramics. *J Eur Ceram Soc* 2012, *32* (10), 2495–2503. https://doi.org/https://doi.org/10.1016/j.jeurceramsoc.2012.03.010.

(259) Xia, K.; Wu, Z.; Xuan, C.; Xiao, W.; Wang, J.; Wang, D. Effect of KOH Etching on the Structure and Electrochemical Performance of SiOC Anodes for Lithium-Ion Batteries. *Electrochimica Acta* 2017, *245*, 287–295. https://doi.org/https://doi.org/10.1016/j.electacta.2017.05.162.

(260) Li, B.; Yuan, X.; Gao, Y.; Wang, Y.; Liao, J.; Rao, Z.; Mao, B.; Huang, H. A Novel SiC Nanowire Aerogel Consisted of Ultra Long SiC Nanowires. *Materials Research Express* 2019, *6* (4), 45030. https://doi.org/10.1088/2053-1591/aafaef.

(261) ASTM, D. 3576, Standard Test Method for Cell Size of Rigid Cellular Plastics. *Annual book of ASTM standards* 1997, *8*.

(262) Brunauer, S.; Emmett, P. H.; Teller, E. Adsorption of Gases in Multimolecular Layers. *J Am Chem Soc* 1938, *60* (2), 309–319. https://doi.org/10.1021/ja01269a023.

(263) Barrett, E. P.; Joyner, L. G.; Halenda, P. P. The Determination of Pore Volume and Area Distributions in Porous Substances. I. Computations from Nitrogen Isotherms. *J Am Chem Soc* 1951, *73* (1), 373–380. https://doi.org/10.1021/ja01145a126.

(264) Blum, Y.; Sorarù, G. D.; Ramaswamy, A. P.; Hui, D.; Carturan, S. M. Controlled Mesoporosity in SiOC via Chemically Bonded Polymeric “Spacers.” *Journal of the American Ceramic Society* 2013, *96* (9), 2785–2792. https://doi.org/10.1111/jace.12485.

(265) Schiavon, M. A.; Domenico Sorarù, G.; Yoshida, I. V. P. Synthesis of a Polycyclic Silazane Network and Its Evolution to Silicon Carbonitride Glass. *Journal of Non-Crystalline Solids* 2002, *304* (1), 76–83. https://doi.org/https://doi.org/10.1016/S0022-3093(02)01007-4.

(266) Dey, A.; Kayal, N.; Chakrabarti, O.; Caldato, R. F.; Innocentini, M. D. de M.; Guerra, V. G. Investigations on Material and Mechanical Properties, Air-Permeation Behavior and Filtration Performance of Mullite-Bonded Porous S

i C Ceramics. *International Journal of Applied Ceramic Technology* 2014, *11* (5), 804–816.

(267) Innocentini, M. D. M.; Tanabe, E. H.; Aguiar, M. L.; Coury, J. R. Filtration of Gases at High Pressures: Permeation Behavior of Fiber-Based Media Used for Natural Gas Cleaning. *Chemical Engineering Science* 2012, *74*, 38–48. https://doi.org/10.1016/j.ces.2012.01.050.

(268) Innocentini, M. D. de M.; Sepulveda, P.; Ortega, F. Permeability. Cellular Ceramics: Structure, Manufacturing, Properties and Applications. *Wiley-VCH* 2005.

(269) Potoczek, M.; Chmielarz, A.; Innocentini, M. D. D. M.; da Silva, I. C. P.; Colombo, P.; Winiarska, B. Porosity Effect on Microstructure, Mechanical, and Fluid Dynamic Properties of Ti2AlC by Direct Foaming and Gel-Casting. *Journal of the American Ceramic Society* 2018, *101* (12), 5346–5357. https://doi.org/10.1111/jace.15802.

(270) Barg, S.; Innocentini, M. D. M.; Meloni, R. V.; Chacon, W. S.; Wang, H.; Koch, D.; Grathwohl, G. Physical and High-Temperature Permeation Features of Double-Layered Cellular Filtering Membranes Prepared via Freeze Casting of Emulsified Powder Suspensions. *Journal of Membrane Science* 2011, *383* (1–2), 35–43. https://doi.org/10.1016/j.memsci.2011.08.003.

(271) Semerci, T.; Dizdar, K. C.; Kulkarni, A.; Dispinar, D.; Soraru, G. D.; Vakifahmetoglu, C. Polymer-Derived Ceramic Molten Metal Filters. *Journal of Materials Science* 2022. https://doi.org/10.1007/s10853-022-07542-9.

(272) Choudhary, A.; Pratihar, S. K.; Behera, S. K. Single Step Processing of Polymer Derived Macroporous SiOC Ceramics with Dense Struts. *Ceramics International* 2019, *45* (6), 8063–8068. https://doi.org/https://doi.org/10.1016/j.ceramint.2019.01.102.

(273) Gabriel, L. P.; Rodrigues, A. A.; Macedo, M.; Jardini, A. L.; Maciel Filho, R. Electrospun Polyurethane Membranes for Tissue Engineering Applications. *Materials Science and Engineering: C* 2017, *72*, 113–117. https://doi.org/https://doi.org/10.1016/j.msec.2016.11.057.

(274) Adnan, S.; Tuan Ismail, T. N. M.; Mohd Noor, N.; Nek Mat Din, N. S. M.; Hanzah, N.; Shoot Kian, Y.; Abu Hassan, H. Development of Flexible Polyurethane Nanostructured Biocomposite Foams Derived from Palm Olein-Based Polyol. *Advances in Materials Science and Engineering* 2016, *2016*. https://doi.org/10.1155/2016/4316424.

(275) Gómez-Fernández, S.; Ugarte, L.; Peña-Rodriguez, C.; Zubitur, M.; Corcuera, M. Á.; Eceiza, A. Flexible Polyurethane Foam Nanocomposites with Modified Layered Double Hydroxides. *Applied Clay Science* 2016, *123*, 109–120. https://doi.org/https://doi.org/10.1016/j.clay.2016.01.015.

(276) Radice, S.; Turri, S.; Scicchitano, M. Fourier Transform Infrared Studies on Deblocking and Crosslinking Mechanisms of Some Fluorine Containing Monocomponent Polyurethanes. *Applied Spectroscopy* 2004, *58* (5), 535–542. https://doi.org/10.1366/000370204774103354.

(277) Taheri, P.; Bokka, A.; Asgari, P.; Jeon, J.; Lang, J. C.; Campostrini, R.; Sorarù, G. D.; Kroll, P. Novel Sulfur-Containing Cross-Linking Agent for Si-Based Preceramic Polymers. *Macromolecular Chemistry and Physics* 2020, *221* (2). https://doi.org/10.1002/macp.201900380.

(278) Marciniec, B. Functionalisation and Cross-Linking of Organosilicon Polymers. *Hydrosilylation* 2009, 159–189.

(279) Sorarù, G. D.; Dalcanale, F.; Campostrini, R.; Gaston, A.; Blum, Y.; Carturan, S.; Aravind, P. R. Novel Polysiloxane and Polycarbosilane Aerogels via Hydrosilylation of Preceramic Polymers. *Journal of Materials Chemistry* 2012, *22* (16), 7676–7680. https://doi.org/10.1039/c2jm00020b.

(280) Ishihara, S.; Nishimura, T.; Tanaka, H. Precipitation Processing to Synthesize Fine Polycarbosilane Particles for Precursors of Silicon Carbide Powders. *Journal of the Ceramic Society of Japan* 2006, *114* (1330), 507–510. https://doi.org/10.2109/jcersj.114.507.

(281) Vakifahmetoglu, C.; Balliana, M.; Colombo, P. Ceramic Foams and Micro-Beads from Emulsions of a Preceramic Polymer. *J Eur Ceram Soc* 2011, *31* (8), 1481–1490. https://doi.org/https://doi.org/10.1016/j.jeurceramsoc.2011.02.012.

(282) Gibson, L. J. Ashby MF: Cellular Solids: Structure and Properties. *Edition: Cambridge Solid State Science Series.* 1997.

(283) Richardson, J. T.; Peng, Y.; Remue, D. Properties of Ceramic Foam Catalyst Supports: Pressure Drop. *Applied Catalysis A: General* 2000, *204* (1), 19–32.

(284) Moreira, E. A.; Coury, J. R. The Influence of Structural Parameters on the Permeability of Ceramic Foams. *Brazilian Journal of Chemical Engineering* 2004, *21*, 23–33.

(285) Moreira, E. A.; Innocentini, M. D. M.; Coury, J. R. Permeability of Ceramic Foams to Compressible and Incompressible Flow. *J Eur Ceram Soc* 2004, *24* (10), 3209–3218. https://doi.org/https://doi.org/10.1016/j.jeurceramsoc.2003.11.014.

(286) Colombo, P.; Bernardo, E.; Biasetto, L. Novel Microcellular Ceramics from a Silicone Resin. *Journal of the American Ceramic Society* 2004, *87* (1), 152–154. https://doi.org/10.1111/j.1551-2916.2004.00152.x.

(287) Colombo, P.; Bernardo, E. Macro-and Micro-Cellular Porous Ceramics from Preceramic Polymers. *Composites Science and Technology* 2003, *63* (16), 2353–2359.

(288) Colombo, P.; Hellmann, J. R.; Shelleman, D. L. Mechanical Properties of Silicon Oxycarbide Ceramic Foams. *Journal of the American Ceramic Society* 2001, *84* (10), 2245–2251. https://doi.org/https://doi.org/10.1111/j.1151-2916.2001.tb00996.x.

(289) Colombo, P.; Modesti, M. Silicon Oxycarbide Ceramic Foams from a Preceramic Polymer. *Journal of the American Ceramic Society* 1999, *82* (3), 573–578. https://doi.org/10.1111/j.1151-2916.1999.tb01803.x.

(290) Prasanth, A. S.; Krishnaraj, V.; Nampoothiri, J.; Sindhumathi, R.; Akthar Sadik, M. R.; Escobedo, J. P.; Shankar, K. Uniaxial Compressive Behavior of AA5083/SiC Co-Continuous Ceramic Composite Fabricated by Gas Pressure Infiltration for Armour Applications. *Journal of Composites Science* 2022, *6* (2), 36.

(291) Biasetto, L.; Innocentini, M. D. M.; Chacon, W. S.; Corradetti, S.; Carturan, S.; Colombo, P.; Andrighetto, A. Gas Permeability of Lanthanum Oxycarbide Targets for the SPES Project. *Journal of Nuclear Materials* 2013, *440* (1–3), 70–80. https://doi.org/10.1016/j.jnucmat.2013.04.038.

(292) Dey, A.; Kayal, N.; Chakrabarti, O.; Innocentini, M. D. M.; Chacon, W. S.; Coury, J. R. Evaluation of Air Permeation Behavior of Porous SiC Ceramics Synthesized by Oxidation-Bonding Technique. *International Journal of Applied Ceramic Technology* 2013, *10* (6), 1023–1033. https://doi.org/10.1111/j.1744-7402.2012.02847.x.

(293) Nazari, E.; Razavi, S. H.; Boutorabi, S. M. A. Effect of Filtration on the Morphology and Mechanical Properties of Mg Molten Alloy Entering the Mould Cavity. *Journal of Materials Processing Technology* 2010, *210* (3), 461–465.

(294) Hashemi, H.; Raiszadeh, R.; Khodadad, M. Study and Modification of Naturally-Pressurized Running System: Effect of Cermic Filter. *J. appl. Sci* 2009, *9*, 2115–2122.

(295) Davami, P.; Kim, S. K.; Varahram, N.; Yoon, Y. O.; Yeom, G. Y. Effect of Oxide Films, Inclusions and Fe on Reproducibility of Tensile Properties in Cast Al–Si–Mg Alloys: Statistical and Image Analysis. *Materials Science and Engineering: A* 2012, *558*, 134–143.

(296) Davami, P.; Kim, S. K.; Tiryakioğlu, M. The Effect of Melt Quality and Filtering on the Weibull Distributions of Tensile Properties in Al–7% Si–Mg Alloy Castings. *Materials Science and Engineering: A* 2013, *579*, 64–70.

(297) Basuny, F. H.; Ghazy, M.; Kandeil, A.-R. Y.; El-Sayed, M. A. Effect of Casting Conditions on the Fracture Strength of Al-5 Mg Alloy Castings. *Advances in Materials Science and Engineering* 2016, *2016*.

(298) Ardekhani, A.; Raiszadeh, R. Removal of Double Oxide Film Defects by Ceramic Foam Filters. *J Mater Eng Perform* 2012, *21* (7), 1352–1362.

(299) Kaufman, J. G.; Rooy, E. L. *Aluminum Alloy Castings: Properties, Processes, and Applications*; Asm International, 2004.

(300) Davila-Maldonado, O.; Adams, A.; Oliveira, L.; Alquist, B.; Morales, R. D. Simulation of Fluid and Inclusions Dynamics during Filtration Operations of Ductile Iron Melts Using Foam Filters. *Metallurgical and Materials Transactions B* 2008, *39* (6), 818–839.

(301) Walton, R. I. Subcritical Solvothermal Synthesis of Condensed Inorganic Materials. *Chemical Society Reviews* 2002, *31* (4), 230–238. https://doi.org/10.1039/B105762F.

(302) Saliger, R.; Heinrich, T.; Gleissner, T.; Fricke, J. Sintering Behaviour of Alumina-Modified Silica Aerogels. *J Non Cryst Solids* 1995, *186*, 113–117.

(303) Aravind, P. R.; Mukundan, P.; Pillai, P. K.; Warrier, K. G. K. Mesoporous Silica–Alumina Aerogels with High Thermal Pore Stability through Hybrid Sol–Gel Route Followed by Subcritical Drying. *Microporous and mesoporous materials* 2006, *96* (1–3), 14–20.

(304) Ratke, L.; Milow, B. Aerogels for Foundry Applications. In *Aerogels Handbook*; Springer, 2011; pp 763–788.

(305) Meyer, E.; Milow, B.; Ratke, L. Development of Aerogel Additives for the Foundry Industry. *The Journal of Supercritical Fluids* 2015, *106*, 62–68.

(306) Ratke, L.; Brück, S. Mechanical Properties of Aerogel Composites for Casting Purposes. *J Mater Sci* 2006, *41* (4), 1019–1024.

VITA

Tuğçe SEMERCİ

Education

Ph.D.- Materials Science and Engineering, Izmir Institute of Technology, 2022
M.Sc.- Materials Science and Engineering, Izmir Institute of Technology, 2015
B.Sc.- Physics, Izmir Institute of Technology, 2012

Appointments

- *Research & Teaching Assistant* - Materials Science and Engineering, Izmir Institute of Technology, 2013-2022.
- *Researcher* - Air Force Office of Scientific Research (AFOSR, USA), Izmir Institute of Technology, 2021-2022
- *Researcher* - Ministry of Science Industry and Technology (SAN-TEZ), Izmir Institute of Technology, 2012-2013.

Publications

- **Semerci, T.**, Dizdar K. C., Kulkarni A., Dispinar D., Soraru G. D., Vakifahmetoglu C., (2022). Polymer-derived ceramic molten metal filters. *Journal of Materials Science*, *in press*.
  DOI: *https://doi.org/10.1007/s10853-022-07542-9*
- Vakifahmetoglu, C., **Semerci, T.**, Gurlo, A., Soraru, G. D. (2021). Polymer derived ceramic aerogels. *Current Opinion in Solid State and Materials Science*, *25*(4), 100936.
  DOI: *https://doi.org/10.1016/j.cossms.2021.100936*
- **Semerci, T.**, de Mello Innocentini, M. D., Marsola, G. A., Lasso, P. R. O., Soraru, G. D., Vakifahmetoglu, C. (2020). Hot air permeable preceramic polymer derived reticulated ceramic foams. *ACS Applied Polymer Materials*, *2*(9), 4118-4126.
  DOI: https://doi.org/10.1021/acsapm.0c00734
- Vakifahmetoglu, C., **Semerci, T.**, Soraru, G. D. (2020). Closed porosity ceramics and glasses. *Journal of the American Ceramic Society*, *103*(5), 2941-2969.
  DOI: *https://doi.org/10.1111/jace.16934*
- **Semerci, T.**, Demirhan, Y., Miyakawa, N., Wang, H. B., Ozyuzer, L. (2017). Fabrication of Bi2212 single crystal bolometer for detection of terahertz waves. In *THz for CBRN and Explosives Detection and Diagnosis* (pp. 75-83). Springer, Dordrecht.
  DOI: *https://doi.org/10.1007/978-94-024-1093-8_11*
- **Semerci, T.**, Demirhan, Y., Miyakawa, N., Wang, H. B., Ozyuzer, L. (2016). Thin film like terahertz bolometric detector on Bi2212 single crystal. *Optical and Quantum Electronics*, *48*(6), 1-11.
  DOI: *https://doi.org/10.1007/s11082-016-0612-0*